Doctoral Dissertation
Doctoral Program in Civil and Environmental Engineering (XXXIV cycle)

Ecomorphodynamic carbon pumping of the world's large tropical rivers

By

Luca Salerno

******

Supervisor(s):
Prof. Carlo Camporeale
Prof. Annunziato Siviglia

Doctoral Examination Committee:
Prof. Francesco Comiti, Università di Bolzano
Prof. Fabio Giulio Tonolo, Politecnico di Torino, Italy
Prof. Jost-diedrich Graf Von Hardenberg, Politecnico di Torino, Italy
Prof. Angela Gurnell, Queen Mary University of London, UK
Prof. Chris Paola, University of Minnesota, US

Politecnico di Torino
2022

Declaration

I hereby declare that, the contents and organisation of this dissertation constitute my own original work and does not compromise in any way the rights of third parties, including those relating to the security of personal data.

Luca Salerno
2022

* This dissertation is presented in partial fulfillment of the requirements for **Ph.D. degree** in the Graduate School of Politecnico di Torino (ScuDo).

Acknowledgements

I would like to acknowledge and give my warmest thanks to my supervisors, Prof. Camporeale and Prof. Siviglia, who helped me to overcome the not only scientific challenges I encountered during my PhD, and without whom I would not have been able to complete this research.

I would also like to thank committee members for their work and in particular the thesis reviewers for their brilliant comments and suggestions.

My gratitude extends to Compagnia Sanpaolo for the funding opportunity to undertake my PhD studies.

I would also like to give special thanks to the Image Processing Laboratory of the University of Valencia for hosting my PhD visiting period. In particular, I would like to express my sincere gratitude to Dr. Álvaro Moreno Martínez and Dr. Emma Izquierdo Verdiguier, for their invaluable advice and continuous support, which have been fundamental to my research.

I would like to extend my sincere thanks to my colleagues, who have supported me and had to put up with my stresses and whines for the past three years of study.

Finally, I am deeply grateful to my family for their encouragement and support throughout my studies.

Abstract

The role of inland waters in the carbon cycle has been re-evaluated in recent decades. In fact, the collective contribution of inland freshwater to the global carbon cycle was found to be comparable to that of terrestrial and marine ecosystems combined. Nevertheless, the quantification of lateral carbon fluxes from wetlands and riparian zones to freshwater is affected by high uncertainties and many processes are still poorly understood. This thesis aims to investigate some unexplored fluxes of inland waters carbon derived from the interactions between river dynamics and riparian vegetation and evaluate the influence of river regulation on floodplain forests.

Rivers are dynamic entities that wander by spanning the floodplain back and forth. During this wandering, the carbon biomass stored in standing vegetation is recruited by flow erosion and partially stocked downstream by sediment burial. Bare landforms become available for atmospheric carbon to be captured by growing vegetation. This 'mowing' and 'stocking' mechanism was explored, quantifying its relevance as an efficient carbon pump for the world's largest tropical rivers.

We suggest that the high mobility of natural rivers plays a significant role in the carbon budget of fluvial corridors. A multi-temporal analysis of satellite data for all world's largest tropical rivers in the period 2000-2019, with 30 m resolution was carried out. Based on this data, quantification of a yet unexplored highly efficient Eco-Morphodynamic Carbon Pump (eCP) mechanism in riverine systems is provided. River morphodynamics is shown to drive carbon export from the riparian zone and to promote CO_2-sequestration. This is realized by an integrated process through floodplain rejuvenation and plant colonization. For tropical rivers larger than 200 m this pumping mechanism alone accounts for 12 ± 0.96 million tons per year of carbon mobilization. In this thesis, signatures of fluvial eco-morphological activity that provide a proxy for the carbon mobilization capability associated with river activity were identified. The magnitude of the carbon pump suggests that care is needed in

breaking the river migration rate – carbon mobilization nexus in the management of tropical rivers promoting innovative and sustainable management criteria.

Moreover, the regular natural flood pulse of large tropical rivers is the main driver of ecological and biogeochemical processes in large Amazonian floodplains. Endemic vegetation species developed adaptation to survive in seasonal flood environments and tune their vital process with periodic flood events, water levels, and sedimentary processes. The construction of hydroelectric dams also causes alterations of the natural hydrological regime and sediment supply, threatening downstream floodplain forests.

An assessment of river regulation impact on floodplain vegetation is crucial to developing a modern watershed management approach in the Neotropics aimed at mitigating alterations of the floodplain environment. Floodplain forest monitoring requires high–resolution mapping, as vegetation dynamics are in the narrow area at the interface between terrestrial and aquatic systems. The existing satellite images that afford land observations have limitations due to coarse resolution or gaps in data caused by the extreme cloudiness of tropical regions.

A new framework for high-resolution mapping and monitoring of a large-scale tropical forest in the aquatic-terrestrial zone of an Amazon basin is provided in this thesis. The main aim is to assess the vegetation status and the environmental degradation in a highly altered fluvial setting. To achieve the goal, a remote sensing processing chain, which couples hydrologic and vegetation data, was developed. A map of high-resolution traditional vegetation indices and their non-linear generalization was derived from the high-resolution gap-free reflectance data obtained by combining Landsat and MODIS data, through the HISTARFM algorithm. Subsequently, hydrological modification within these areas was assessed by using a global water surface dataset.

In addition, the impact of river regulation on riverine forest carbon cycling was assessed through the analysis of interannual variability of the gross primary production of floodplain vegetation. The framework was applied to analyze the last two decades of changes in the floodplain forest of Uatumã river (central Amazon basin), downstream of the Balbina hydropower dam built in 1987. The analysis showed the presence of vegetation degradation in areas of increased hydrologic stress and upland forest encroachment in areas no longer inundated. The dam continues to have effects on vegetation even 30 years after its construction. The ongoing profound

reshuffling of the floodplain forest and the impact on the carbon storage capacity of the floodplain forest suggest that the situation is far from a new environmental equilibrium.

The proposed high–resolution approach allows for a detailed mapping of riparian vegetation alterations, helping to develop a more careful management of the watershed through a better understanding of the human footprint on floodplain forests.

Contents

List of Figures

List of Tables

Nomenclature

Table 1 List of Abbreviations

AGWB	Aboveground Biomass
API	Application Programming Interface
ATTZ	Aquatic-Terrestrial Transition Zone
AVHRR	Advanced Very High Resolution Radiometer
BS	Bell-Shaped
Bu	Burial
eCE	eco-morphodynamic Carbon Export
eCP	eco-morphodynamic Carbon Pump
ENPP	Enhanced Net Primary Production
EVI	Enhanced Vegetation Index
FAPAR	Fraction of Absorbed Photosintetically Active Radiation
GEE	Google Earth Engine
GFHR	Gap-Filled High spatial Resolution data
GHG	Greenhouse gases
GPP	Gross Primary Production
GBP	Intern. Geosphere-Biosphere Progr.
HISTARFM	HIghly Scalable Temporal Adaptive Reflectance Fusion Model
ICW	Inorganic Carbon input from Weathering
IPCC	Intergovern. Panel on Climate Change
kNDVI	kernel Normalized Difference Vegetation Index
LCW	Large Coarse Wood
LSWI	Land Surface Water Index
MM	Multi-Modal pattern
MODIS	Moderate Resol. Imaging Spectroradiomete
MNDWI	Modified Normalized Difference Water Index
M_r	Migration rate
NDVI	Normaized Difference Vegetation Index

continue →

continue →

NPP	Net Primary Production
NHV	Natural with High vegetation density
NLV	Natural with Low vegetation density
NPP	Net Primary Production
NS	Negatively Skewed pattern
PAR	Photosysntetically Active Radiation
PD	Population density
PF	Photosynthetic fixation
POM	Particulate Organic Matter
PS	Positively Skewed pattern
R	Respiration
ROI	Region Of Interest
RZ	Riparian Zone
SCW	atmospheric CO_2 uptake from Silicate and Carbonate Weathering
TSS	Total Suspended Sediment
USDR	Uatama Sustainable Development Reserve
WHRC	Woods Hole Research Center

Part I

Chapter 1

Introduction

1.1 Carbon cycle in the Inland Waters

Although inland freshwaters cover only 1% of the Earth's surface, their collective contribution to global carbon fluxes is comparable to all other terrestrial and marine ecosystems combined (Cole et al., 2007).

The idea of river networks just as passive and static conduits that deliver water and carbon from the headwaters to the oceans was deeply reconsidered in the last decades. Rivers are complex and dynamic systems within which carbon is actively produced, conveyed, and stored in several forms (Aufdenkampe et al., 2011; Battin et al., 2009; Cole et al., 2007; Regnier et al., 2013), involving the global carbon cycle at different spatial and temporal scales.

Fluvial systems transfer carbon laterally from the terrestrial ecosystem toward the oceans, while exchange vertically with the atmosphere (Cole et al., 2007; Regnier et al., 2013). The terrestrial carbon enters in the inland waters either as organic matter derived from biological processes or as inorganic carbon from the geological compartment (further details about processes involved in inland water carbon cycle are described in Chapter 2).

During their transport, carbon-containing molecules entered into the river network can be transformed through chemical or physical processes. The C output from the inland waters toward the oceans is only the final result of the complex series of transformations and losses that it undergoes during its journey (Cole et al., 2007;

Regnier et al., 2013). Continuous exchanges with the atmosphere and the terrestrial sedimentary compartment represent the pathways for which inland waters are not passive conduits. In general, there are essentially three fates for carbon entered in the river network: i) re-emitted into the atmosphere essentially as CO_2 or CH_4; ii) buried and then stored within the fluvial sedimentary compartment or lakes; iii) arriving in the ocean. In the next section, a review of carbon fluxes in the inland water will be provided highlighting the recent literature assessments and their uncertainties.

1.1.1 Inland water carbon budget

The amount of C input to inland waters is far larger than the one exported to estuaries and coastal oceans. In order to frame the carbon cycle involving inland waters, it is possible to identify the main incoming and outgoing fluxes through a mass balance equation:

$$C_w^{in} + C_t^{in} + C_{ph}^{in} = C_{gas}^{out} + C_o^{out} + C_{bu}^{out}, \tag{1.1}$$

where C_w^{in} is the inorganic C input from weathering of silicate and carbonate rocks, C_t^{in} is the carbon permeated from fast carbon cycle of terrestrial ecosystems as Large Coarse Wood (LCW), Particulate Organic Matter (POM) or Dissolved Organic Carbon (DOC) or as dissolved carbon dioxide from soil respiration, C_{ph}^{in} is the carbon fixed by in-stream biomass from atmosphere and not respired by the inland waters, C_{gas}^{out} is the carbon evaded in gaseous form (e.g. CO_2 or CH_4) from water, C_o^{out} is the total C exported to the oceans, C_{bu}^{out} is the total C burial in inland water sediment.

The total bulk C input to inland waters (the left hand side of eq. 1.1) was quantified as 2.7-2.9 Pg C/yr [1] based on up-scaling of local C budgets (Battin et al., 2008; Cole et al., 2007; Regnier et al., 2013; Tranvik et al., 2009). In a simplified way, this terrestrial carbon input can be calculated as the quantity necessary to close the mass balance given the output flows (oceanic export, burial, and outgassing). A more recent review of the literature data has highlighted how the assessment of this input is subject to continuous evolution due to the updates of estimates of the individual flows (Drake et al., 2018). In particular, Drake et al. (2018) suggests an input from the ground of approximately 5.1 PgC /yr, highlighting how the substantial uncertainties in all the main budget terms affect this estimate. Although the evaluation of the quantity of carbon transported by rivers reaches the ocean has not changed radically

[1] a Petagram of carbon (Pg C), is equal to 10^{15} grams or one billion tonnes

in the last 40 years, new technologies and methods of analysis have led to an increase in the estimate of carbon released into the atmosphere by rivers and lakes by about 5 times in the last 2 decades. Moreover, the estimation of the inland water carbon cycle is made more difficult by anthropogenically induced disturbances that impact the carbon fluxes (Drake et al., 2018; Regnier et al., 2013). The main fluxes of inland water carbon cycle are shown in Figure 1.1 (the references of fluxes showed in figure are reported in Table 1.1). Further details about the inland water carbon cycle are provided in Chapter 2.

Table 1.1 Carbon fluxes reported in Fig. 1.1, with references. Colored rows refer to fluxes involved in the inland waters C-budget commented in the present thesis (see Chapter 2).*According to Drake et al. (2018). ** Budget of CO_2 emissions and uptake from estuaries and air-sea CO_2 flux in the Oceans. *** Total C burial in estuarine and oceans sediment. References: Raymond et al. (2014); Drake et al. (2018); Cole et al. (2007); Regnier et al. (2013); Lal (2003); Battin et al. (2009); Tranvik et al. (2009); Aufdenkampe et al. (2011), Hartmann et al. (2009)

Carbon flux	Reference	Role in Inland waters budget	Estimates (PgC/yr)	Level of Uncertainty*	Consequence on C cycle*
Outgassing	Raymond et al. (2013) Drake et al. (2018)	Out-coming	2.1 3.9	high	high
Oceanic export	Cole et al. (2007) Regnier et al. (2013)	Out-coming	0.9 0.95	low	low
Burial	Lal et. al (2003) Battin et al.(2009) Tranvik et al. (2009) Aufdenkampe et al. (2011) Regnier et.al (2013)	Out-coming	2.8-4.2 0.6 0.6 1.5 0.6	high	high
Autochthonous photosynthetic fixation	Regnier et al. (2013)	In-coming	0.3	high	moderate
Bed-rock weathering	Hartmann et al. (2009)	In-coming	0.5	-	-
C export from terrestrial ecosystem to inland water (resulting from a difference of the above fluxes)	Drake et al. (2018)	In-coming	2.9 - 8.3	high	high
Geological fluxes	Regnier et.al (2013)		0.15	-	
Fluxes from Atmosphere to Oceans and Estuaries (net) F_1	Regnier et.al (2013)**		2.1	-	-
Fluxes from Oceans and Estuaries to Sediments (net) F_2	Regnier et.al (2013)***		0.65	-	-
Silicate and Carbonate weathering F_3	Hartmann et al (2009) Regnier et.al (2013)		0.3-0.44 0.35	- -	 -
Antropogenic fossil-fuel emissions F_4	Regnier et.al (2013)		7.9	-	-

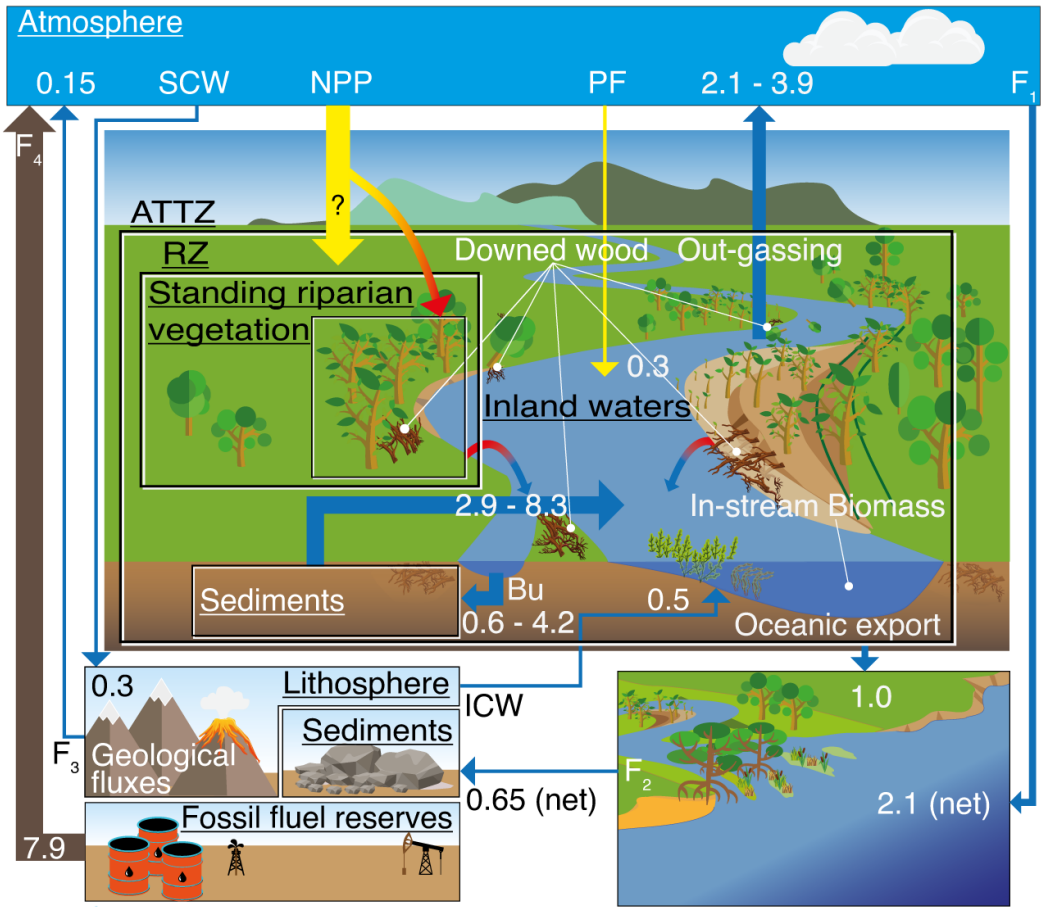

Fig. 1.1 Global carbon budget of the aquatic-terrestrial transitional zone in rivers, with fluxes reported in PgC/yr. Red-to-blue arrows represent large coarse woody (LCW) flux through river morphodynamic activities (eCE), estimated in the present work to 12 TgC/yr for large tropical rivers (width > 200 m). Yellow-to-red arrows refer to ENPP (C-fixation promoted by vegetation encroachment on bare riparian areas generated by the morphodynamic activity). SCW: atmospheric CO_2 uptake from Silicate and Carbonate Weathering; ICW Inorganic Carbon input from Weathering; Bu: Burial; PF: Photosynthetic fixation; ATTZ: Aquatic-Terrestrial Transitional Zone RZ: Riparian Zone. Meaning, definitions, source literature of fluxes F_1-F_4 and for all other arrows are reported in Table 1.1

1.2 New analysis of the carbon cycle in tropical rivers

This thesis aims to investigate some unexplored fluxes of inland waters carbon cycle. These fluxes are driven by interactions between river dynamics and riparian vegetation and could represent an additional term to left side of equation (1.1). We focused our attention on large tropical rivers mainly for two reasons. Firstly, the processes investigated are present in water courses where fluvial connectivity allows

exchanges of water, sediment, and organic material between floodplains and the river. Furthermore, given the limited temporal availability of satellite data (less than half a century), it is necessary to analyze areas where the responses of vegetation to river perturbations are very fast. The tropics thus represent an ideal study region, where there are still large rivers showing their pristine condition unaltered by human activities and where dense, highly productive vegetation populates the floodplains. Secondly, the case of the Tropics deserves special attention, given that in these regions river connectivity is threatened by the construction of a massive number of new dams (351 large new dams are planned in the Amazon, La Plata, and Andean-foreland basins). We show that tropical countries urgently need major watershed management interventions, in order to limit the impact of freshwater exploitation on the global carbon cycle.

1.2.1 A compound machinery for carbon pumping

Recognition by Cole et al. (2007) of the river system as a dynamic component of the Earth's carbon cycle has brought increasing attention to the analysis of the carbon cycle in Inland waters (Battin et al., 2009; Drake et al., 2018; Regnier et al., 2013). Nevertheless, the estimates of carbon fluxes through the terrestrial aquatic continuum are affected by high uncertainties as to make the inland water carbon cycle far from being fully explained. More specifically, the lateral fluxes of wetland and riparian ecosystems are poorly known yet. The wetlands and riparian zones represent complex transition ecosystems between the *terra firma* and the aquatic zone and are characterized by marked spatiotemporal variability. River migration and flow fluctuations, with the alternation of erosion and deposit phenomena of floodplains, play an active role in the flux of dissolved, particulate, and coarse carbon in the water compartment (Evans, 2022). Rivers periodically rework the floodplains, removing vegetation through uprooting or bank erosion. This vegetation recruitment by fluvial dynamics represents a pathway through organic carbon stored in the terrestrial ecosystem enters the inland waters. The flow of organic carbon that reaches rivers and travels through the fluvial network, can result from soil leaching (DOC or Particulate Organic Carbon (POC)), or from this morphodynamic-driver recruitment. While the role in the carbon cycle of the first component is well recognized (although not constrainedly assessed), the second component is often implicitly assumed to be rapidly degraded and mineralized. We argue that it is a misconception to assume

that all woody input is decomposed and reduced to micrometric size during the transit time in the fluvial system, and hence solely contributes to the fine component. The degradation time of the wood material (Holt and Jones, 1983; Junk, 1997a; Mackensen et al., 2003; Torres, 1994) is very often greater than the time it takes to reach the oceans. This is true both if the wood material leaves rivers and floodplains in a few months and when it is buried (and kept in anoxic conditions that protect it from degradation) and re-mobilized many times before reaching the ocean. Unlike the fine or dissolved fraction, the carbon contained in this coarse material can reside for a long time in the floodplains or oceanic sediments before being mineralized and returning to the atmosphere. Moreover, river dynamics are fundamental in the growth and development of floodplain forests. The morphodynamic-driven vegetation recruiting generates bare fertile riparian areas wherein new vegetation can rapidly grow. This continuous vegetation rejuvenation process influences the net primary production of the floodplain forests maintaining the system at an intermediate highly productive stage. This compound mechanism of ecomorphological Carbon Export eCE (recruitment of mature vegetation) and enhancement of net primary production (ENPP) has been defined by us as an ecomorphological Carbon Pump (eCP) and will be described in detail in Part II of this thesis.

1.2.2 Anthropological impact of tropical river regulation

The present-day inland water carbon cycle is affected by human activities that impact many relevant fluxes. Regnier et al. (2013) estimated that anthropogenic perturbations (land-use change, agriculture, soil erosion, liming, sewage-water production, damming of water courses, water withdrawal, and human-induced climatic change) have increased the exchange of carbon to inland water by ~ 1.0 Pg C/yr since pre-industrial times. Soil erosion (~ 0.8 Pg C/yr) was identified as the main cause of this human-driven C flux increase (Regnier et al., 2013). Moreover, human sewage represent an additional flux (~ 0.1 PgC/ yr) of highly biodegradable organic carbon (Regnier et al., 2013). These additional bio-available sources of organic carbon could trigger and promote respiration of stable sinks of carbon through a process called priming (Bianchi, 2011; Evans, 2022; Regnier et al., 2013). The increase in CO_2 concentration in the atmosphere causes an increase in weathering that (David, 2010), with a consequent CO_2 capturing and an increase in inorganic carbon fluxes in water courses (Regnier et al., 2013). The above-mentioned interaction represents

only some of the anthropogenic influences on the inland water carbon cycle. Given the complexity of the phenomena analyzed and the high uncertainty in the estimates of each stream, the estimates of anthropogenic impact so far are considered poorly constrained (Drake et al., 2018). Although Regnier has shown it is possible to close a balance of all the components (anthropogenic and non-anthropogenic) of the land-to-ocean aquatic continuum, the datasets available to date do not allow robust estimates of these components (Regnier et al., 2013). Anthropogenic impacts need to be further investigated to understand their impact on the various compartments of the carbon cycle.

For example, the use of hydropower dams is controversial and many aspects related to their impact are not fully understood. Despite the importance that these structures have in the energy production, many studies have unraveled the impacts of hydroelectric dams (Almeida et al., 2019; Kahn et al., 2014), highlighting the social, economic and environmental negative repercussions (Agostinho et al., 2018; Assahira et al., 2017; Castello and Macedo, 2016; Cochrane et al., 2017; Fearnside, 2002, 2014; Fearnside and Pueyo, 2012; Nilsson and Berggren, 2000; Poff and Hart, 2002; Timpe and Kaplan, 2017). Furthermore, the consequences of large damming are not only limited to the area near the infrastructure but also affect floodplains downstream and the estuarine environment at large scales (Andersson et al., 2000; Castello and Macedo, 2016; Latrubesse et al., 1957; Merritt and Wohl, 2006; Tealdi et al., 2011). The Amazon basin has among the largest total number of existing dams (151), as well as planned and under-construction (358) dams (Zarfl et al., 2015), and this makes the Amazonian floodplains one of the most threatened ecosystems in the world (de Resende et al., 2020; Kahn et al., 2014; Lees et al., 2016). An assessment of the impact of river regulation on floodplain vegetation is crucial to developing a modern approach to the management of the regulated river in the Neotropics and to mitigate the impact of damming on the floodplain environment. Nevertheless, in these remote areas, field measurement activities are extremely challenging and expensive while the excessive cloudiness makes the use of the classic satellite approach prohibitive. In Part III of this thesis, an operative framework will be proposed and used for assessing the degradation status of the floodplain forest of altered basins.

1.2.3 The thesis in a nutshell

This thesis focuses on two aspects concerning on the interaction between river and floodplain vegetation:

(i) During their movement, the rivers recruit carbon biomass stored in riparian vegetation and partially stock it in sedimentary compartments (fluvial or oceanic). Moreover, new areas are made available for colonization of new vegetation that, by growing, can capture carbon from the atmosphere. We explore and quantified this highly efficient pumping mechanism in riverine systems. Through a satellite-based analysis, we assessed the carbon exported by large tropical river as LCW. Furthermore, the relevance of carbon pumping mechanism in the carbon cycle were discussed in detail, highlighting the role of the pump in supporting innovative and sustainable river management criteria.

(ii) The amazonian floodplain represents one of the world's most threatened ecosystems due to the number of existing and under-construction dams that alter the delicate equilibrium between natural flood pulse and floodplain forest. Defining what management policies are the best to be able to manage hydropower dams requires mapping and monitoring ecosystems so that river regulation can be modulated to minimize environmental impacts. In this thesis, we propose an operative framework for high-resolution mapping and monitoring of a large-scale tropical forest in the aquatic-terrestrial zone of Amazon basins. The aim of this framework is to assess the vegetation status and the environmental degradation in an altered fluvial setting, through coupling hydrological and vegetation data.

The ecomorphodynamic carbon pump (eCP) mechanism will be analyzed in the Part II. In Chapter 3, we introduce a new integrated nexus between sediment transport, migration rate and carbon sequestration. That nexus gives rise to a virtuous circle in the carbon budget of inland waters, driven by the river morphodynamic activity, and promotes CO_2 sequestration from the atmosphere into the riparian zones and eventually into fluvial sediments and oceans. We define such a compound machinery as carbon pump comprised by the organic carbon export by river dynamics (eCE) and enhanced production of new vegetation in riparian zone (ENPP). We assessed the eCP from high-resolution analysis of satellite data of the world's largest tropical

rivers (Chapter 5). More in detail we show and discuss the result about eCE at global and continental scale (Section 5.2 and 5.1). In the Section 5.3 we analyze the nexus between sediment transport, migration rate and carbon sequestration reanalysing 14 tropical rivers. The ENPP is described in Section 5.4, providing an example of assessment in a point bar or Beni river. In addition, the section 5.5 describes how river dynamics influence the distribution and conformation of floodplain forests, leaving clear "signatures" in carbon maps. The thesis also shows the negative effects of anthropic alterations on the fluvial Eco-Morphodynamic Carbon Pumping in Neotropics, so promoting a carbon budget approach in the management of regulated rivers (see Section 5.6). Finally, the Chapter 4 provides the methodological approach used for eCP assessment describing the definition of region of interest, the probabilistic approach to assess the vegetation loss due to river dynamics, the 4 different methodologies used to calculate the eCE, downscaling to smaller rivers and the uncertainties analysis.

The Part III of this thesis describes the alteration of floodplain vegetation due to river regulation detected through a satellite analysis. The role of natural annual cycle of water level on floodplain forest dynamics will be introduced in Chapter 6 , focusing on the threat that river regulation represent for these environments. A new operative framework to assess the impact of dam alteration on floodplain environment will be presented in chapter 7. To achieve this goal, we combined forest change detection (Section 7.2-7.4.4) with an analysis of hydrological transition and the assessment of annual gross primary production (Section 7.5.1). The framework will be applied to a case study (Uatama river) and the results will be presented in the Chapter 8. In the chapter 9 we discuss the potentiality of the framework highlighting it strength and weaknesses (Sections 9.1,9.2). Finally, our results obtained from the analysis of Uatama river will be compared with literature date to analyse multi-decadal effect of dam management in Sections 9.3 and 9.4.

Chapter 2

The inland water carbon cycle up close

The processes investigated in the following Parts II and III involve the interactions between carbon contained in the biomass of riparian vegetation and the inland waters. This chapter aims to provide a conceptual background of the main processes involved in the inland water carbon cycle in order to frame the fluxes analysed in this thesis in the broader plethora of processes that involves the carbon cycle in the Aquatic-Terrestrial Transitional Zone (ATTZ).

2.1 Carbon input pathways in the inland waters

The terrestrial ecosystems fix carbon vertically from the atmosphere through photosynthetic activity. Photosynthesis is the process used by autotrophic organisms to synthesize the organic matter from inorganic precursors (e.g. CO_2) through the use of solar energy and reducing power. In the plants, specialized plastids (the chloroplasts) are the reactive centers within which the endergonic oxidation-reduction process occurs fixing carbon into carbohydrates (biomass) and releasing oxygen. Therefore, during the plant life cycle carbon is stored in stems, branches, and leaves (above-ground) or roots (below-ground) while is continuously exchanged with the pedosphere through plant detritus, roots exudate, or after plant death. This terrestrial organic carbon can enter laterally in inland waters either through river migration or

overflow and flooding that recruit plants, large coarse wood, or sediment (from soil erosion) or through leaching of the soil in dissolved or particulate form.

Another fundamental pathway to carbon input in inland waters is the export from the inorganic compartment. Carbon can enter the inland waters as dissolved CO_2 or CH_4 derived by soil respiration (Drake et al., 2018; Regnier et al., 2013); Furthermore, rivers contribute to link weathering of the continental surface with oceanic sedimentation (Evans, 2022). The terrestrial weathering of silicate or carbonate rocks recruits carbon from atmospheric CO_2 and produces dissolved ions as the result of the weakening and subsequent disintegration of minerals. The drainage network receives such ions (dissolved carbonate and bicarbonate) and transports them to the oceans wherein can be sedimented releasing partially (ions from silicate weathering) or totally (ions from carbonate weathering) the CO_2 consumed during weathering reaction. Finally, rivers receive particulate calcium carbonate or calcite minerals from erosion and physical weathering of carbonate rocks. Although the fluxes mentioned above represent the main carbon inputs in the freshwaters, a plethora of other contributes exist. Algae and in-stream autotrophic organisms fix carbon to their make their sustenance. This process can be considered an input for inland waters only if CO_2 used in photosynthetic activities is from the atmosphere. Another input carbon flux is due to dissolved fraction in sewage water originating from biomass consumption by humans and farming (Regnier et al., 2013).

2.2 Inland water carbon fates

The carbon entered in river network can be essentially re-emitted into the atmosphere, buried and then stored within the fluvial sedimentary compartment or lakes or exported in oceans. In the follow, we briefly reviewed the last estimates of these fluxes

Carbon burial in inland water sediment

A fraction of the terrestrial carbon that the inland water receives, transports, and processes ends up being stored in freshwater sediments. The estimates of the rate of C burial in sedimentary comportment are still poorly constrained today and affected by great uncertainties Drake et al. (2018). Cole et al. (2007) highlights the role

that carbon stored in lake sediments plays in the global carbon cycle. The carbon accumulated in lakes during the Holocene is estimated to be between 400 and 800 Pg. Accumulation of C in lakes is large, despite not having a very high C rate (~ 0.05 Pg C/yr, Cole et al. (2007)), partly because lake sediments are preserved much longer (10,000 years or more) relative to forest biomass or soil (decades or centuries) (Cole et al., 2007). More in general, Cole et al. (2007) estimated that freshwater sediments (excluding sediment storage in rivers and streams) store every year 0.23 Pg C. Recent studies have reassessed the global area occupied by lakes and reservoirs and the burial of carbon in small lakes. Nevertheless, the lack of large-scale empirical data on sedimentation rate and carbon content in sediments makes carbon storage in inland waters still very uncertain (Drake et al., 2018). The range of estimates on carbon storage goes from 0.2 to 1.6 Pg. Given the large uncertainty value, some studies assume with low confidence an arbitrary value of 0.6 Pg (Battin et al., 2009; Drake et al., 2018; Regnier et al., 2013; Tranvik et al., 2009). However, these estimates could add up to 4.2 PgC due to the reburial (Lal, 2003). For these reasons, Drake et al. (2018) ranks storage estimates in the carbon cycle as highly uncertain and with strong consequences on the cycle itself.

Outgassing: C that returns to the Atmosphere

Inland waters are not a passive transport tube, and carbon undergoes physical and biological transformations during its journey through the network before reaching the ocean. A fraction of carbon delivered by rivers is re-emitted in the atmosphere in gaseous form (mainly as CO_2, but also as CH_4) (Raymond et al., 2014; Regnier et al., 2013). Rivers and lakes are generally supersaturated systems with an p_{CO_2} that range from ~ 1,300-4,300 μatm (Raymond et al., 2014). Carbon evading from freshwaters can originate from soil or root respiration, from decomposition and oxidation of terrestrial organic matter or sewage (Regnier et al., 2013). Rivers and streams typically emit C in gaseous form as CO_2. In lakes and reservoirs, in addition to carbon dioxide, methane (CH_4) is produced and released by surface diffusion, ebullion, or diffusion through plant stems

The role of outgassing is relevant to the global carbon cycle since the magnitude of emissions of greenhouse gases from inland waters is similar to CO_2 uptake from the oceans (Tranvik et al., 2009). Nevertheless, the assessment of carbon released into the atmosphere is challenging and affected by high uncertainties (Drake et al.,

2018). Over the past two decades, estimates of C-evasion have been continually updated, thanks to an improved geospatial assessment of the global surface-water area, and an increased number and coverage of measurements. This has led to an increase in early conservative estimates and a refinement of assessments of C fluxes. We provide a summary of the last most significant results about C outgassing. Cole et al. (2007) was among the first to recognize the active role of inland waters in the global carbon cycle, identifying net gaseous emissions as one manifestation of this activity. Cole et al. (2007) estimated the CO_2 emitted from globally large rivers, reservoirs, and groundwater withdrawals to be 0.75 PgC/yr. Headwater systems were not included in the estimates because of lacking of data about gas transfer velocity and the global extension of stream cover (Cole et al., 2007). However, since those systems are known to be net emitters of CO_2, Cole speculates that this makes his estimates extremely conservative. Raymond et al. (2014) obtained a global CO_2 evasion rate of 1.8 PgC/yr from rivers and streams and 0.32 from lakes and reservoirs, combing global hydrographic data sets with river scaling laws, discharge estimates for global drainage basins, and assessment of gas transfer velocity across river network. Raymond predicts river and stream evasion hotspots in regions characterized by high gas transfer rates and high surface area (high precipitation areas such as the Tropics). However, the paucity of data in such regions makes the estimates particularly uncertain and further studies are needed. Borges et al. (2014) provided a further refinement of assessment in African tropical areas, through a reanalysis of sub-Saharan rivers and wetlands. Their results increase 0.6 PgC/yr from the estimated in the same region provided by Raymond et al. (2014), confirming the relevance of tropical regions. Through direct measurement of CO_2 fluxes, Sawakuchi et al. (2017) revised the outgassing estimates of the lower Amazon, assessing an emission rate of about 0.48 PgC/yr. Including the value of lower tributaries with updated estimates of CO_2 outgassing from small streams, Sawakuchi et al. (2017) estimates outgassing from Amazon running waters to 0.95 PgC/yr. Holgerson and Raymond (2016) estimated the contribution of non-running inland waters to be 0.58 PgC/yr. Carbon dioxide and methane concentration measurements from 427 small lakes and ponds were used to estimate their diffusive carbon emissions and to upscale the overall carbon efflux of very small water bodies. Contributions from the aforementioned studies were used by Drake et al. (2018) to update the estimates of Raymond et al. (2014). By considering the more detailed data about the African region (Borges et al., 2014), the estimates of Amazon basin contribution Sawakuchi et al. (2017) and role

of non-running inland waters Drake et al. (2018) obtains a global CO_2 evasion rate of 3.9 PgC/yr. Despite these recent improvements in outgassing estimates many aspects remain poorly understood and further investigation is needed. As stated by Drake et al. (2018); Raymond et al. (2014) small rivers and stream contributions could be underestimated. In these streams, especially in tropical areas, the availability of measured data is limited. Raymond et al. (2014) argued the lacking of measurements of gas-transfer velocity in rivers with a high slope and during the variation in flow conditions represents a large research gap. In fact, the paucity of data is the main source of uncertainty in all estimates. Moreover, although inland waters in tropical regions are recognized as among the largest emitters, are also those where greater uncertainty and scarcity of data are present. The role of wetlands and floodplains in these regions is not yet well defined. The contribution of C evasion of wetlands and floodplains of large rivers is controversial, as they are intermediate between terrestrial and aquatic systems. Although they are characterized by highly supersaturated water, their CO_2 efflux can be compensated by uptake of emergent vegetation, which is often omitted from the carbon balance of inland waters (Cole et al., 2007; Drake et al., 2018). Although their emissions are not considered among those of watercourses, current estimates of CO_2 evasion contain an unknown fraction from these ecosystems. As argued by Drake et al. (2018), this is particularly relevant in wetland-dominated systems such as the Amazon River. They estimated the contribution of flooded Amazon environment equal to 15 %, by comparing recent estimates of Amazon wetland emissions (Abril et al., 2014) with stream outgassing assessment provided by Sawakuchi et al. (2017). The gaps still present in the literature and the continuing increases in the assessment of outgassing led Drake to rank the uncertainty of the amount of carbon outgassed high with an important impact on the estimate of C input from the lands.

Table 2.1 Estimates of global oceanic export in Pg per year. DOC Dissolved Organic Carbon, POC particulate Organic Carbon, DIC Dissolved Inorganic Carbon, PIC Particulate Inorganic Carbon

DOC	POC	DIC	PIC	Data Source	Description
-	-	0.45	-	Kempe (1979)	Revision of previous study flux of HCO_3^- fluxes from rivers
0.25	0.15	-	-	Hedges et al. (1997)	
0.37				(Schlesinger and Melack, 1981)	Extrapolated from 12 rivers
0.22	0.18	0.17	0.38	Meybeck (1982)	
0.20	0.1	0.24	-	Meybeck (1993)	
0.36	-	-	-	Aitkenhead and McDowell (2000)	Predicted based on relation with soil C:N ratio
0.17	-	-	-	Dai et al. (2012)	
0.24	0.24	0.41	0.17	Li et al. (2017)	
0.21	0.17	0.32	-	Ludwig et al. (1996)	Result of empirical model from 29 rivers
0.9				Cole et al. (2007)	

Oceanic Export

The fate for a fraction of carbon transported by rivers is to arrive in the ocean. Four components of this flux are commonly measured: dissolved organic carbon (DOC), particulate organic carbon (POC), dissolved inorganic carbon (DIC), and particulate inorganic carbon (PIC). Over the past four decades, several studies have been conducted to estimate the components of oceanic export (Table 2.1 shows some of the most important). By revising previous estimates of HCO_3^- fluvial fluxes (Livingstone, 1963), Kempe (1979) estimated that rivers transport to the ocean 0.45 Pg C/yr as DIC. Schlesinger and Melack (1981) first estimated that the total flux of organic carbon (OC) was 0.37 Pg C/yr by extrapolating the data from 12 intermediate-to-large rivers. An analysis of all four components of flux to the oceans was given by Meybeck (1982) who, through a review of literature data on river carbon concentration, estimated a global carbon flux of about 0.9 PgC /yr (0.22 Pg

C/yr DOC, 0.18 Pg C/yr POC, 0.17 Pg C/yr DIC, 0.38 Pg C/yr PIC). A result similar to previous OC estimates was obtained by Ludwig et al. (1996) through an empirical model (OC flux ~ 0.38 Pg C/yr). A recent review by Cole et al. (2007), confirms the results obtained in the last decades, i.e. that rivers carry ~ 0.9 billion tons of carbon into the ocean every year. The above estimates are based on analyses conducted on large rivers or basins. Although the carbon contribution of large basins to ocean exports is relatively well established, some factors of uncertainty about the role of small rivers could lead to considering the flow underestimated (Drake et al., 2018). While the role of headwaters in the production of carbon flux is well known (in particular POC; in fact about 40% of global POC flux is derived from land surfaces with slopes of over 10%, and represent OM source to downstream waters), the role of small rivers or basins that drain directly into the ocean from continental margins has only recently been analyzed. In particular, recent results by Anderson and Amon (2015); Holmes et al. (2013) about small to medium rivers in the Arctic show how extrapolation of C flows from larger rivers can underestimate the total input into the Arctic Ocean (Drake et al., 2018).

Furthermore, although the flow components studied so far are thought to comprise the main forms in which carbon reaches the sea through the river network, the contribution of carbon contained in coarse particulate matter or large coarse woods has never been studied on a global scale. This stems from the fact that this type of coarse material ends up being routed during floods, and its direct estimation is therefore prohibitive. Moreover, from a classical point of view is assumed that all woody input is decomposed and reduced to micrometric size (traditionally considered $< 20\ \mu$m) during the transit time in the fluvial system, and hence solely contributes to the DOC or POC component.

Part II

Carbon Pumping by tropical rivers

The contents of the present Part has been partially derived from Camporeale et al. (2022).

Chapter 3

Introduction

Rivers are not simply passive and static conveyance systems that deliver water and sediments from the headwaters to the oceans, but instead they actively affect the global carbon budget (Cole et al., 2007; Wohl et al., 2017). Although the carbon lateral export from terrestrial ecosystems is recognized to be a key pathway in the biogeochemical carbon cycle (Aufdenkampe et al., 2011), the role of river dynamics in carbon mobilization has generally been overlooked (Battin et al., 2009; Ciais et al., 2013; Drake et al., 2018; Le Quéré et al., 2018). By exploring the sediment load – river dynamics – carbon flux nexus of tropical regions, we show that river morphodynamics is central to carbon fluxes between terrestrial systems, river corridors and the atmosphere.

Through a global–scale assessment of the dynamics and vegetation density within the aquatic-terrestrial transion zone (ATTZ), we evaluate that the world's largest tropical rivers annually recruit 12 million tons of carbon as Large Coarse Wood (LCW). Through the exploration of an Eco-Morphodynamic-Carbon-Pumping (eCP) mechanism we identify that this recruitment may promote a virtuous cycle for carbon sink, mostly deposited in floodplains but probably even farthest, in oceans.

Under the classical view of the River Continuum Concept (Vannote et al., 1980), LCW exported from floodplains is fragmented and decomposed as it moves downstream, with the consequent transformation of organic matter into a fine particulate, Dissolved Organic Matter (DOM), and then outgassing. However, the ultimate fate of LCW recruited by stream waters is far from being fully explained. For example, rivers with high sediment loads have been demonstrated to easily bury wood at least

at the same rate as the wood exported to estuaries (Kramer and Wohl, 2016). Several studies have provided evidence that, once recruited by the channel, LCW can persist buried in the alluvium for extraordinarily long times (Ruiz-Villanueva et al., 2016a). This suggests that some processes are overlooked in river carbon budgeting (Drake et al., 2018). Indeed, riverine sediment storage is a key aspect of biogeochemical cycling, since part of biospheric organic carbon is stored in terrestrial reservoirs over millennial timescales before reaching ultimate depocenters in marine basins (Torres et al., 2017).

Like the biological carbon pump (David, 2010), whereby phytoplankton net production and its ultimate marine fall drive carbon from the atmosphere to ocean interior and seafloor sediments, we conjecture that photosynthetic fixation by riparian vegetation, the recruitment of LCW, its transport, and burial, fit together in an integrated nexus in which rivers drive a carbon pump from the atmosphere to long-term stocks (i.e. floodplains and ocean). In particular, carbon mobilization is triggered by a two-steps pumping mechanism that we name Eco-Morphodynamic Carbon Export (eCE) and Enhanced Net Primary Production (ENPP). eCE refers to the carbon export from floodplains, whereas ENPP consists of C-fixation promoted by vegetation encroachment on bare riparian areas generated by the morphodynamic activity. We therefore define the eCP as the combination of these two processes, that work in cascade, and that are mainly energized by channel migration in meandering rivers and by overflow and flooding in multi-thread rivers (Fig. 3.1).

Moreover, we show how river regulation can affect floodplain forests (see Part III) and the carbon cycle in general. The debate on the impact of large basins is currently affected by the poor understanding of the carbon budget in inland waters. At least 3700 major dams are either planned or under construction worldwide, thus reducing the number of the remaining free-flowing large rivers by about 21% (Zarfl et al., 2015). The Neotropics represent among the most threatened regions due to the large number of dams planned for the next years. Dams interrupt the sediment transport continuum in the river system, causing an estimated reduction of 1.4 billion tons per year worldwide in sediment load trapped by reservoirs (Syvitski et al., 2005), and reducing river mobility and floodplain regeneration. Moreover alteration of natural water level oscillations, perturbs the complex interaction between water and vegetation life cycle (further details in Part III).

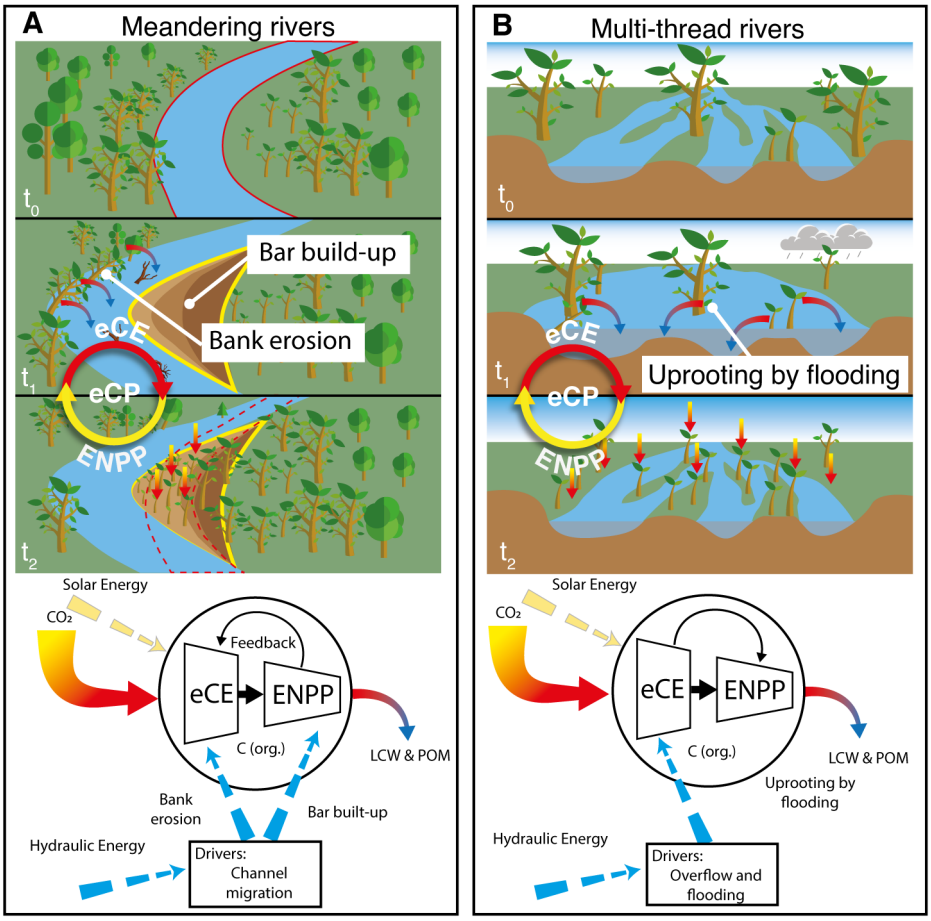

Fig. 3.1 The functioning of the ecomorphodynamic Carbon Pumping (eCP) mechanism. a) In meandering rivers, channel- migration-driven capture of woody biomass are exported from the outer bank into the stream (eCE). Young biomass then colonizes the inner newly deposited point bar, so driving further CO_2-fixation from the atmosphere (ENPP) and promoting further river migration (feedback effect). Hydraulic energy (dashed blue arrows) drives morphodynamics and channel migration, while solar energy (dashed yellow arrows) drives the consequent CO_2 fixation from atmosphere. b) In multi-thread rivers, extreme hydrologic events cause a reorganization of floodplain, exporting biomass from bars, banks and islands into the stream (eCE). Young vegetation colonize the newly available spots so driving further CO2-fixation from the atmosphere (ENPP). Hydraulic energy (dashed blue arrows) drives the overflow events, while solar energy (dashed yellow arrows) drives the consequent CO_2 fixation from atmosphere. In both cases, the output of the pump is the mobilization of LCW and POM, which is eventually stored in river channel sediments or in oceans.

3.1 LCW dynamics and the carbon pumping mechanism

River systems store carbon in four interconnected compartments (Sutfin et al., 2016): a) Standing riparian biomass; b) Large downed wood (>10 cm in diameter and 1 m in length); c) Sediments, litter humus, and soil organic carbon (SOC); d) In-stream biomass which decomposition process produces Particulate Organic Matter (POM) and Dissolved Organic Carbon (DOC). In this paper, we refer to previously disregarded carbon fluxes of LCW as the wood directly recruited from compartment a) and delivered to other compartments through bank erosion, flooding, uprooting and burial (Fig. 3.2). Hence, we do not focus at SOC, whose dynamics has already been well explored elsewhere (Lal, 2003; Ludwig et al., 1996).

Notably, a process gap can be highlighted in the latest calculations of the carbon cycle budget, whereby the LCW component of the aquatic–floodplain-estuarine flux remained unexplored (Battin et al., 2009; Ciais et al., 2013; Drake et al., 2018; Le Quéré et al., 2018). In fact, the global estimate (Fig. 1.1) of about 2.9-8.3 PgC/yr of carbon exported from terrestrial ecosystems (fluvial sediments and riparian vegetation) to inland waters is obtained by subtracting the *out-fluxes* – i.e., outgassing (2.1-3.9 PgC/yr, ref. Drake et al., 2018; Raymond et al., 2014; Sawakuchi et al., 2017), burial (0.6-4.2 PgC/yr, ref. Drake et al., 2018; Lal, 2003), and the oceanic export (~1 PgC/yr, ref. Regnier et al., 2013) – from the *in-fluxes* i.e., bedrock weathering (0.5 PgC/yr, ref. Hartmann et al., 2009) and in-stream autochthonous photosynthetic fixation (~20% of the out-fluxes, ref. Regnier et al., 2013). However, this budgeting overlooks LCW recruitment, since it is reasonable not assuming that the whole woody input is decomposed and reduced to micrometric size (traditionally considered <20 μm) during the transit time in the fluvial system, and hence not stating that transported wood is transformed into the fine fraction of POM or it is mineralized.

Furthermore, recent assessments of global CO_2-evasion rates (Horgby et al., 2019; Raymond et al., 2014) and inland water surfaces (Allen and Pavelsky, 2018) do not consider in the budget the vegetation recruitment to flow downstream, transport, deposition, and burial in the floodplain (Le Quéré et al., 2018; Ruiz-Villanueva et al., 2016a). Since the main source of LCW arises from plant uprooting due to overflow and bank erosion, logs tend to be routed during floods, and floating logs can

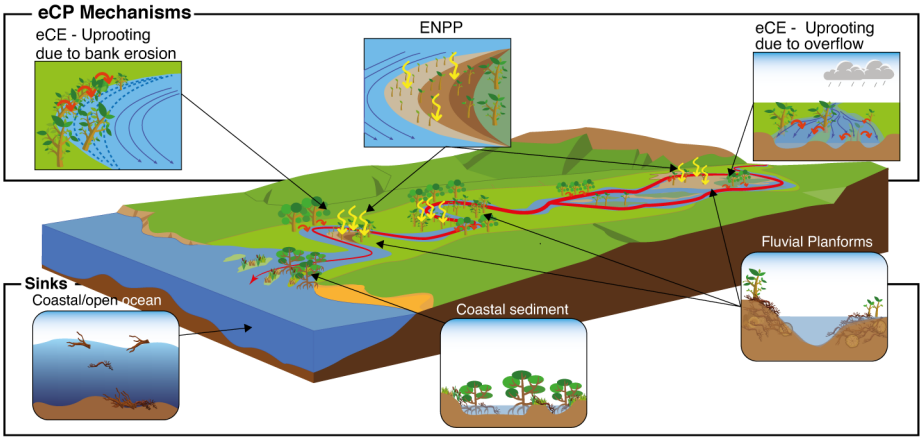

Fig. 3.2 Conceptual sketch of pathways of the ecomorphodynamic Carbon Pump (eCP) in the inland waters.

survive for years before decomposing (Mackensen et al., 2003). The organic carbon (OC) in the form of POM or LCW can be deposited under anoxic conditions and stabilized at long term (Boye et al., 2017; Davies and Gibling, 2011). In addition, the high migration rates in lowland meandering rivers may reduce the residence time of floodplain-stored material (Torres et al., 2017), and therefore limit the time available for the oxidation (Bradley and Tucker, 2013). Although a fraction of the carbon recruited by the river returns to the atmosphere through processes of decomposition (Junk, 1997a) and out-gassing (Abril et al., 2014), there is a part that is permanently stocked within river corridors as sedimentary organic carbon (Torres et al., 2017), or delivered to coastal zones and deep oceans (Regnier et al., 2013). Indeed, this stock is responsible for the deposits in floodplains over geological timescales, which currently account for more than 20% of the world's remaining hydrocarbon reserves (Keogh et al., 2007). On the other hand, LCW does not necessarily remain on a consistent downstream journey in the river and may spend significant time in logjams or deposited onto the floodplain (Beckman and Wohl, 2014).

A quantification of the role of LCW in the carbon budget of the aquatic-terrestrial transitional zone seems to be needed (Wohl, 2016) and a knowledge gap and the uncertainties in the fluxes reported in Fig. 1.1 were already remarked (Drake et al., 2018). In summary, three aspects deserve further investigation: i) The recruitment of LCW flux seems to be generally underestimated at the global scale, although it is strongly associated with river morphodynamic processes nevertheless; ii) Periodic rejuvenation of the riparian vegetation triggers a still unexplored *enhacement* of

the net primary production (NPP) of the fluvial corridor, with a direct effect on the carbon budgeting; iii) The fate of LCW fluxes after the recruitment from the riparian zone still lacks a quantitative global estimation (Le Quéré et al., 2018), in particular concerning the effect of burial in tropical floodplains (Ruiz-Villanueva et al., 2016a; Sutfin et al., 2016), in lakes and estuaries (Tranvik et al., 2009). By conjecturing and quantifying the Eco-morphodynamic Carbon Pump (eCP), the present work focuses on points i) and ii) above.

The first step of the pumping mechanism (i.e., eCE) comprises the stream-induced biomass recruitment of LCW from standing riparian vegetation by erosion and flood-induced uprooting. This biomass is uprooted and/or transported into the water stream (or it remains downed in situ) and either stocked somewhere through burial in the fluvial floodplains or delivered to the oceans. The second step (ENPP) is C-fixation promoted by vegetation encroachment and primary production on new bare riparian areas. These two steps involve two carbon fluxes crossing the riparian zone, respectively outgoing and incoming.

Chapter 4

Methods

4.1 ROIs definition

Each analysed river was divided into Regions of interest (ROIs) characterized by homogeneous morphological behavior. The ROI represents the elementary unit for the calculation of eCE and are characterized by longitudinal and lateral boundaries. The changes in Horton-Strahler order (Strahler, 1957), sinuosity, transition from single-thread to multi-thread or vice versa, or sudden changes in channel width (Allen and Pavelsky, 2018) were considered as geomorphological criteria longitudinal divides between two consecutive ROIs (*sensu* ref. (Gurnell et al., 2016)). The main channel of the analysed rivers has the width grater than 200m, when referring to the mean annual discharge, according to the analysis by (Allen and Pavelsky, 2018). The lateral extent of ROIs comprises the land adjacent to the stream where vegetation is influenced by rivers dynamics and/or flooding. Such an active lateral area was identified in two steps.

First, it was considered the spatial gradient in biomass density. The areas frequently involved by flooding or river dynamics are featured by vegetation adapted to survive and are characterized by successional pattern with specific biomass distributions (Schöngart and Wittmann, 2010). An analysis of high-resolution biomass map allowed us to identified edges between floodplain forest and land forest (e.g., defined as *terra firma* in Amazonian basins, Fig. 4.1).

Second, where the lateral boundaries were not evident by biomass map, we also considered the water surface occurrence by using the GWS dataset (Pekel et al.,

2016). Accordingly, the identification of sites ever detected as water over the last 35 years in the GWS dataset enabled us to identify the aquatic-terrestrial transitional zone.

Nevertheless, short-lived events are not always correctly detected by GSW because such events must be concurrent with cloud-free satellite observations. Because of the extreme cloud contamination that characterizes the tropical area (particularly the eastern Amazon Basin and western Congo Basin), many short but intense events cannot be included in the event map developed by Pekel et al. (2016), making our estimates of the lateral boundaries of the ROIs further conservative.

4.2 River selection and data filtering

As mentioned above, the boundaries of each ROI were defined by considering the biomass distribution gradients and the areas within which the active riverbed occurred at least once during the period 1984–2019 in the Global Surface Water database (Pekel et al., 2016). In order to ensure a eCE quantification that was strictly based on river-driven forest loss (RDFL), a three-step selection procedure was used to identify and exclude non-RDFL cases, e.g., rivers impacted by anthoripic activities. Step 1: All evident sources of anthropic alteration were identified by visual inspection from Landsat images, such as physical infrastructures in the river channel or along the surrounding floodplain, presence of river channelization, check dams, weirs, fords, embankments, bank protection, revetments and mining activities. For these reasons, all large Indian rivers were excluded. Step 2: Rivers classified as *not free flowing* through the CSI index by Grill et al. (2019) – i.e., rivers in which fragmentation and regulation or alteration in water quality and temperature compromise fluvial connectivity (CSI index $< 95\%$, SI Appendix, Table S2) – were also excluded. These first two steps excluded 91% of 1,297,000 km overall length of all tropical reaches with Horton-Strahler index ≥ 4. Step 3: A probabilistic classification model was used to define the likelihood P that river-driven forest loss (RDFL) occurred for each pixel within the ROIs. Extreme likelihood values are P=0 (no forest loss or forest loss unquestionably due to causes other than river dynamics), and P=1 (forest loss unquestionably due to river geomorphic activity). To assess intermediate probabilities, the *Global Forest Change* dataset (Hansen et al., 2013) was combined with three potential causes of non-river-driven forest loss: i) population density; ii)

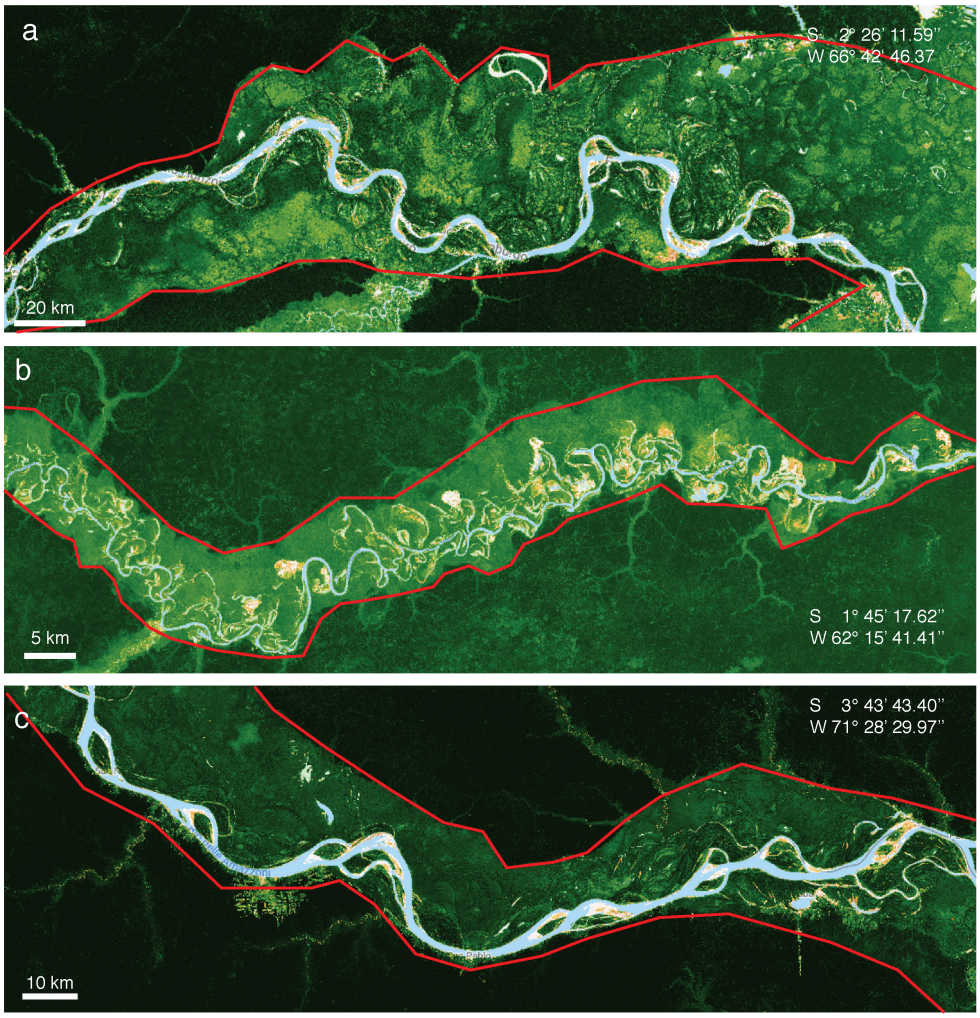

Fig. 4.1 **Three examples of carbon density map, from dataset (Zarin et al., 2016), and the lateral extension of ROIs (red solid line).** The recurrent fluvial disturbances that affect floodplain vegetation and promote a continuous rejuvenation of riparian corridors (removal of mature vegetation and colonization by seedlings and young trees of bare riverbanks) thus inducing an immature stage and a lower C-stock than non-flooded mature forests (Chambers et al., 2001; Schöngart and Wittmann, 2010). An edge between carbon distributions of the disturbed floodplains and *terra firma* is well visible in the carbon map developed by Zarin et al. (2016) and it was used to define the lateral extension of ROI (red line). (a) Amazon river, near the Jutai river confluence; (b) Rio Cuiuni (c) The upper Amazon river near Iquitos (Perù).

forest fires; iii) land-cover changes (source datasets are listed in SI Appendix, Table S2). For any pixel k of ROI j in which forest loss occurred, the model assessed the likelihood that the forest cover change was not due to urbanization ($P_{j,k}^{(\mathrm{u})}$), wildfire ($P_{j,k}^{(\mathrm{wf})}$) or man-made land-cover changes ($P_{j,k}^{(\mathrm{lc})}$), thus yielding three probability maps (SI Appendix, Sect. 2B). The overall likelihood map was obtained by multiplying the three probability maps, since they refer to independent events, namely $P_{j,k}$= $P_{j,k}^{(\mathrm{u})} \cdot P_{j,k}^{(\mathrm{wf})} \cdot P_{j,k}^{(\mathrm{lc})}$. In this way, an area of 260 ± 17 km^2 annually in the tropical wetlands of large rivers was classified as non-RDFL and therefore excluded from the whole analysis. This corresponds to 28% of the annual cover loss detected in the ROIs. The result of the filtering procedure for three example cases are shown in SI Appendix, Fig. S7. The data used in this study refer to the HydroRIVERS data layers (Linke et al., 2019) providing vectorized line network of all global rivers with a catchment area greater than 10 km^2 or an average river flow larger than 0.1 m^3/s, and were derived from HydroSHEDS data (Lehner and Grill, 2013) based on a grid resolution of 15 arc-seconds. River order was expressed using the Horton-Strahler ordering system. Following this system, the first order represents headwater streams and when two streams with the same order meet, they form a river of one order greater.

Table 4.1 List of the global databases analysed in the present work.*Dataset updated annually, version 1.7 was used in this study which analyzes the period 2000-2019. **Dataset updated annually, version 1.3 was used in this study which analyzes the period 2000-2019. References: Baccini et al. (2012); Zarin et al. (2016); Hansen et al. (2013); Pekel et al. (2016); Giglio et al. (2015); Linard et al. (2012); Gaughan et al. (2013); Sorichetta et al. (2015); Friedl and Sulla-Menashe (2015); Grill et al. (2019); Linke et al. (2019).

Dataset	Description	Data source	Use in this paper (Section)
WHRC Carbon Stock	A national-level map of above-ground live woody biomass density for tropical countries at 500m resolution. This dataset was assembled from a combination of co-located field measurements, LiDAR observations, and imagery recorded from the Moderate Resolution Imaging Spectroradiometer (MODIS).	Baccini (2012)	Estimation of carbon density within regions of interest (eCE Computation - Method M4), Calibration of model for plant growth (SI-Logistic growth model – Method M2), (Classification of the biomass distribution signature).
WHRC Aboveground Live Woody Biomass Density	Global-scale, map of aboveground biomass (AGB) at approximately 30-meter resolution. This data product expands on the methodology presented in Baccini et al. (2012) to generate a global map of aboveground live woody biomass density (megagrams biomass ha-1) for the year 2000.	Zarin (2016)	Estimation of carbon density within regions of interest (eCE Computation – Methods M1, M2, M3), Calibration of model for plant growth (SI-Logistic growth model- Method M2).
Global Forest Change	Results from time-series analysis of Landsat images to characterize global forest extent and change.	Hansen (2013)* dataset version 1.7 (2000-2019)	Identification of river-driven forest loss RDFL (River selection and data filtering).
Global Surface Water	Maps of the location and temporal distribution of surface water from 1984 to 2019 and statistics on the extent and changes of those water surfaces.	Pekel (2016)** dataset version 1.2 (2000-2019)	Assessment of wet area within regions of interest (ROIs definition).
MODIS Burned Area Monthly Global 500m	The Terra and Aqua combined MCD64A1 Version 6 Burned Area data product is a monthly, global gridded 500m resolution product containing per-pixel burned-area and quality information.	USGS (2000-2019)	Definition of probability map of river-driven forest loss loss $P_{j,k}^{(wf)}$ (River selection and data Filtering).
WorldPop Global Project Population Data	Global high-resolution, contemporary data on human population distributions.	Linard (2012) Gaughan (2013) Sorichetta (2015)	Definition of probability map of river-driven forest loss loss $P_{j,k}^{(u)}$ (River selection and data Filtering).
MODIS Land Cover Type Yearly Global 500m	The MCD12Q1 V6 product provides global land cover types at yearly intervals (2001–2019) derived from six different classification schemes.	Biosphere Programme classification (IGBP)	Definition of probability map of river-driven forest loss $P_{j,k}^{(lc)}$ (River selection and data filtering).
Free Flowing Rivers	Mapping the world's free-flowing rivers.	Grill (2019)	Identification of natural river reaches not impacted by human activities CSI (River selection and data filtering).
HydroATLAS RiverATLAS	Comprehensive database presenting a wide range of hydro-environmental attributes from existing global datasets in a consistent and organized manner.	Linke (2019)	Assessment of Strahler index of river reaches (River selection and data filtering) and downscaling (Downscaling).

4.3 Definitions of maps $P_{j,k}^{(u)}$, $P_{j,k}^{(wf)}$ and $P_{j,k}^{(lc)}$

A probabilistic classification model was used to define the likelihood P that a River-Driven Forest Loss (RDFL) had occurred for each pixel within the ROIs. To this aim, the *Global Forest Change* dataset (Hansen et al., 2013) was filtered by considering three potential causes of no river-driven forest losses: i) population density; ii) forest fires; iii) land-cover changes (source datasets for these events are listed in Table 4.1). Accordingly, for any j-th pixel of the k-th ROI wherein forest loss occurred, the

model assessed the likelihood that the forest cover change is not due to urbanization ($P^{(u)}_{j,k}$), wildfire ($P^{(wf)}_{j,k}$) or man-made land-cover changes ($P^{(lc)}_{j,k}$), thus producing three probability maps.

The values reported in the map $P^{(u)}_{j,k}$ decrease with the population density (PD). According to a relationship between the human pressure score and the population density for sparsely populated areas suggested by Venter et al. (2016), we set:

$$P^{(u)}_{j,k} = \begin{cases} 1 - 0.333 \cdot \log(\mathrm{PD}+1), & \text{for PD} < 1{,}000 \quad \text{people/km}^2 \\ 0 & \text{for PD} \geq 1{,}000 \quad \text{people/km}^2 \end{cases}$$

Human population density was retrieved from the dataset *WorldPop Project Population* (Gaughan et al., 2013; Linard et al., 2012; Lloyd et al., 2019; Sorichetta et al., 2015) at 100 m resolution.

To define the maps $P^{(wf)}_{jk}$ and $P^{(lc)}_{jk}$, the probability that the forest loss in a given year has not been caused by a non-River-Driven Event (henceforth referred non-RDE) was expressed as a function f(Δt), where Δt is the time gap (causal relation principle) between the forest loss and non-RDE occurred in the same region (wildfires or land cover changes). The function f(Δt) (the probability that the loss has been caused by a non-RDE) follows a piecewise dependence on time, as reported in the Fig S5.

Basically, if the forest loss and the non-RDE belong to the same year (i.e., Δt =0), the causal connection is guaranteed, so the function f takes the maximum (f =1). Cases with Δt<0 means that the non-RDE anticipated a forest loss. In this case, a positive causal connection may be possible for several reasons. For example: i) the non-RDE might have not caused a detectable forest loss in the same year, e.g., a wildfire that irreversibly damaged the vegetation which however died in the following months/years; ii) extreme cloudiness of tropical region caused a delay in the forest loss detection. In the cases with Δt >0, forest loss anticipated the non-RDE. Albeit counter-intuitive, even in this case a positive causal connection can be possible. For example, a slow land conversion (e.g., from forest to cropland) that takes some years to cover a portion of territory observable through MODIS-based dataset (coarse resolution 500 m) while was suddenly detected as forest change in the Landsat-based products (resolution of 30 m). In each plot performing a forest loss during the observation window, fire events were detected by using the MODIS-based

dataset (Giglio et al., 2015). We set

$$P_{j,k}^{(\mathrm{wf})} = \prod_{i=1}^{N} 1 - f_i(\Delta t), \tag{4.1}$$

where N is the number of fires observed during the 2000-2019 in the pixel. Where no fires were observed, $\mathrm{P}_{jk}^{(wf)}$ =1. We remark that this filter excludes the capture of recalcitrant LCW generated by the incomplete combustion of biomass during fires, so-called black carbon as analyzed in Jones et al. (2020) . This aspect may be an additional source of underestimation of the present eCE assessment. where N is the number of fires observed during the 2000-2019 in the pixel. Where no fires were observed, $P_{j,k}^{(wf)}$=1. We remark that this filter excludes the capture of recalcitrant LCW generated by the incomplete combustion of biomass during fires, so-called black carbon as analyzed by Jones et al. (2020). This aspect may be an additional source of underestimation of the eCE assessment.

The map $P_{j,k}^{(lc)}$, namely the likelihood that forest loss is not due to land cover change caused by human activity, is generated by using the data product MODIS Land Cover Type MCD12Q1 (Friedl and Sulla-Menashe, 2015). Following the classification of the Annual International Geosphere-Biosphere Programme (IGBP, Table 4.2, ref. Friedl and Sulla-Menashe, 2015) , four land cover macro-classes were identified: Natural with High vegetation density (NHV), Natural with Low vegetation density (NLV), Anthropic (AN) and Water/Unvegetated (UV). A per-pixel analysis at MODIS scale was performed in ROIs and each yearly variation in land cover macro class was detected and classified. In each pixel, the variations from NHV to NLV, from NHV to AN and from NLV to AN were considered as due to human activities while all the other changes were attributed to river morphodynamic processes (i.e., RDFL).

Table 4.2 IGBP Classification

Classes	IGBP (Land Cover – Type1)
Natural with High vegetation density (NHV)	Evergreen Needleleaf forest
	Deciduous Needleleaf forest
	Evergreen Broadleaf forest
	Deciduous Broadleaf forest
	Mixed Forest
	Closed/Open Shrublands
	Grasslands and Permanent Wetlands
Natural with Low vegetation density (NLV)	Savannas
	Woody Savanna
Anthropic (AN)	Croplands
	Croplands/Natural vegetation mosaics
	Urban and Built-up lands
Unvegetated (UV)	Water bodies
	Permanent snow and ice
	Barren

The probability that the forest loss at pixel k of ROI j was not due to human induced land cover change is therefore defined as

$$P_{j,k}^{(lc)} = \prod_{i=1}^{N} 1 - f_i(\Delta t), \tag{4.2}$$

where N is the number of land cover transitions observed during the 2000-2019 in the same pixel, while (Δt) is the time difference between the forest loss and the land cover change. When no human-induced land cover variations were detected, $P_{j,k}^{(lc)}$=1.

For the above reasons, a conservative choice in terms of eCE estimation was to assume that when forest loss and non-RDE occurred within the temporal window of five years they were causally connected, so f=1. The result of the filtering procedure for three example cases are shown in Fig. 4.2.

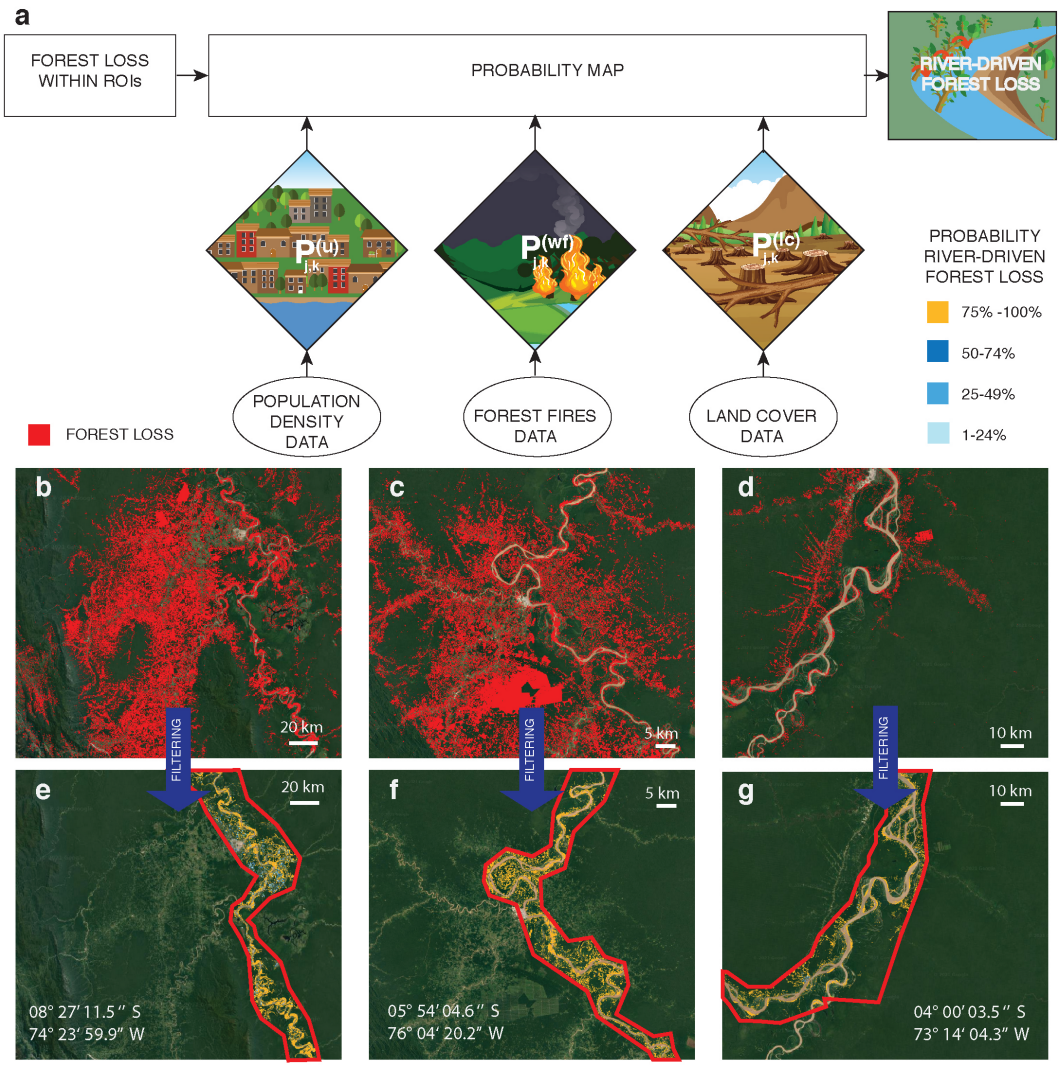

Fig. 4.2 **Filtering procedure.** (a) Conceptual algorithm. (b-d) Satellite images before filtering, with forest loss reported in red. (e-g) Same images after filtering, with the probability of River-Driven Forest Loss clustered in four classes (see legend).

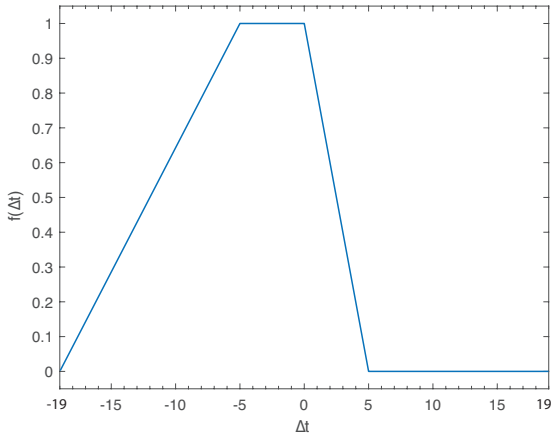

Fig. 4.3 The function $f(\Delta t)$.

eCE computation

The eCE of j-th ROI was computed as

$$\mathrm{eCE}_j = \sum_k \mathrm{eCE}_{j,k} = \sum_k L_{j,k} \cdot \rho_{j,k}, \quad [\mathrm{TgC/yr}], \tag{4.3}$$

where $\rho_{j,k}$ is the biomass density [TgC/km^2] and $L_{j,k}$ is the annual mean RDFL [km^2/yr] for the period 2000–2019, and for pixel k of ROI j. In order to statistically exclude non-fluvial causes, $L_{j,k}$ was computed as the product between the surface $A_{j,k}$ of the cell and the likelihood $P_{j,k}$ of loss being RDFL (see the previous section). For the assessment of biomass density we adopted four different methods (M1–M4). Method M1: $\rho_{j,k}$ was taken from the WHRC *Carbon Stock* dataset developed by Zarin et al. (2016) for the above-ground living woody biomass density at 30 m resolution for the year 2000. In this case, carbon density of a single cell was assumed constant during the entire period of analysis, neglecting the possibility that plots where loss occurred after the year 2000 might have experienced an increase in the carbon content due to growth in the time between 2000 and the year of loss. Method M2: The value of carbon density of each pixel was adjusted considering the amount of vegetation had grown between the year 2000 and the year of loss, by using a calibrated logistic growth model (Section 4.4). Methods M3 and M4: The value of carbon density of each pixel was approximated using the spatial average over the whole ROI (i.e., $\rho_{j,k}$=$\sum_k \rho_{j,k}/N_j$, being N_j the number of pixels in ROI j) by using the WHRC *Carbon Stock* datasets by Zarin et al. (2016) for M3 and Baccini

et al. (2012) for M4. These datasets describe biomass in tropical regions for only a limited period (the year 2000 for Zarin et al. (2016) and the period 2007-2008 for Baccini et al. (2012)). Tropical rivers are highly dynamic systems that during a inter-decade evolution likely visit most of their geomorphological configurations (e.g., the Ucayali river, a tributary of the Amazon river, shows migration rates of up to 100 m/year). For methods M3 and M4, we therefore adopted an ergodic-like hypothesis (Paine, 1985), which allowed the temporal mean of carbon density in a single plot to be inferred from its spatial average over the whole ROI. It is worth noting that spatial averaging in methods M3 and M4 induces a slight underestimation of the eCE (Table 5.1), since the erosion mechanism and the consequent capture of biomass usually involve the mature bank, where vegetation is at a higher level of growth. Since the considered datasets only report the above-ground biomass (AGB) density, the belowground biomass (BGB) was assessed as $\mathrm{BGB}=0.489 \cdot \mathrm{AGB}^{0.89}$ (Saatchi et al., 2011), and the total carbon was estimated as 50% of the total biomass (AGB+BGB). From the estimates of eCE, we also estimated the carbon sequestrated per unit ROI area and per river length ($\mathrm{eCE_A}$ = eCE/S_r [kg C/m^2 yr], where S_r is the the ROI surface, and eCE_L=eCE/L_r, where L_r is length of river reaches within ROI). We remark that the relative differences of the eCE estimation among methods M1-M4 does not exceed 3.3% (Table 5.1). Quantitatively, the four different methods therefore perform in a very similar way, despite they are based on different datasets. For simplicity, the results reported in the main text refer to the Method 2. A graphical summary of the whole methodology is reported in Fig. 4.4.

4.4 Calibration of the logistic growth model update in Method M2

In the method M2, the increasing in the carbon content, due to vegetation growth between the acquisition time (year 2000, ref. Zarin et al., 2016) and the time of forest loss, was considered by calibrating a simplified logistic biomass growth model (Camporeale et al., 2013; Muneepeerakul et al., 2007),

$$\frac{d\rho_i}{dt} = \alpha_i \rho_i \left(V_i - \rho_i\right), \tag{4.4}$$

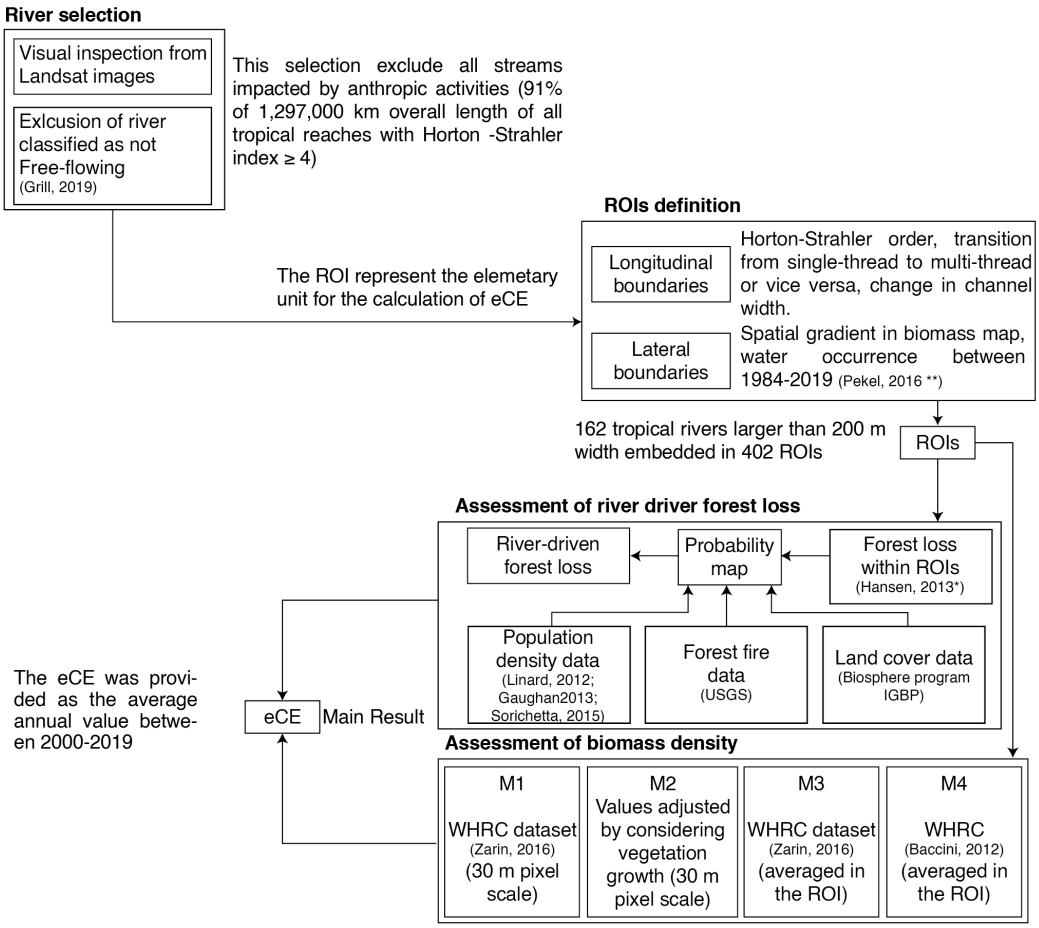

Fig. 4.4 Recapitulation of the procedure for the eCE assessment. For further details on the datasets used refer to Tab. 4.1. *Dataset updated annually, version 1.7 was used in this study which analyzes the period 2000-2019. **Dataset updated annually, version 1.3 was used in this study which analyzes the period 2000-2019.

where ρ is the biomass carbon density, t is time, V is the carrying capacity, i.e. the maximum sustainable biomass carbon density, and α is the growth rate, while subscript i refers to the generic i-th cell. By setting the initial condition $\rho_{0,i}=\rho(t_0)$, that corresponds to the biomass reported by the dataset (Zarin et al., 2016) at year t_0=2000, the formal solution of equation (4.4) at time $t=t_0+\Delta t$ reads

$$\rho_i(t) = \frac{A_i \rho_{0,i} V_i}{(A_i - 1)\,\rho_{0,i} + V_i}, \tag{4.5}$$

where we have defined $A_i=\exp(V_i \alpha_i \Delta t)$. We calibrated the function $A_i(t)$ and the parameter V_i in order to use the equation (4.5) to update the value of carbon biomass density from $t=t_0$=2000 to the time of the cover loss ($t=t_0+\Delta t$), for any cell. The calibration procedure relies on the comparison of carbon biomass as reported by two different datasets with acquisition times eight years apart (Zarin et al. (2016) and Baccini et al. (2012), referring to 2000 and 2008, respectively). The comparison of these two datasets is possible since they were generated by the same methodology, albeit with different resolution (30 mpx for ref. Zarin et al. (2016) and 500 mpx for ref. Baccini et al. (2012)). In the following recursive procedure, the two datasets will be tagged with subscripts $_{30}$ and $_{500}$, respectively. Firstly, all cells in the 30 m resolution dataset were resampled to the 500 m resolution within blocks corresponding to the pixel boundaries of the second dataset. Secondly, for each j-th block, we imposed the matching between the mean of the values $\rho_{30,i}$ within the block (updated at t=2008) and the value $\rho_{500,j}$, namely,

$$\frac{1}{N_j} \sum_{i=1}^{N_j} [\rho_{30,i}]_{t=2008} = \rho_{500,j}. \tag{4.6}$$

which, after using equation (4.5), becomes

$$\frac{1}{N_j} \sum_{i=1}^{N_j} \left. \frac{A_i \rho_{0,i} V_i}{(A_i - 1)\,\rho_{0,i} + V_i} \right|_{\Delta t = 8 \text{ yr}} = \rho_{500,j}, \tag{4.7}$$

where N_j is the number of 30 m resolution cells in the j-th 500 m resolution block. Third, it was assumed that all cells within each block share the same value of A_i and V, so $A_i=A$ is a constant which can be taken out from the summation in (4.7). Furthermore, since $1/\rho_{0,i}(A-1) \sim 1/\rho_{0,i} \gg 1/V$, as a first order approximation we

get

$$A|_{\Delta t^*} \sim \frac{\rho_{500,j}}{\rho_M}, \tag{4.8}$$

where $\rho_M{=}N_j^{-1}\sum_{i=1}^{N_j}\rho_{0,i}$. By iterating and substituting (4.8) in (4.7) one gets a second order approximation

$$A|_{\Delta t^*} \sim \frac{N_j \rho_{500,j}}{\sum_{i=0}^{N_j} \frac{1}{\frac{\frac{\rho_{500,j}}{\rho_M}-1}{V}+\frac{1}{\rho_i}}}. \tag{4.9}$$

By recursion, it is evident that further approximations lead to a cumbersome formula containing a continued fraction in the denominator of (4.9), and for numerical convenience it suffices to stop at the second step. The carrying capacity was cautiously assumed constant throughout the ROI and equal to the maximum value of ρ_M (namely, V=ρ_M^{max}). By replacing in (4.5), and after recalling that $A|_{\Delta t}{=}(A|_{\Delta t^*})^{t/\Delta t^*}$, where $\Delta t^*{=}$ 8 yr is the time lag between the two datasets, one finally gets the relationship for the carbon density updated at time t, for each cell:

$$\rho_i(t) = \frac{(A|_{\Delta t^*})^{t/\Delta t^*}\rho_{0,i}\rho_M^{max}}{\left[(A|_{\Delta t^*})^{t/\Delta t^*}-1\right]\rho_{0,i}+\rho_M^{max}}. \tag{4.10}$$

An example of use of equations (4.9)-(4.10) is reported in the Fig. 4.5.

4.5 ENPP computation

C-sequestration in AGWB of a single tree has been calculated as the difference of the C-stock between consecutive years along the whole lifespan (Schöngart et al., 2011). Accordingly, the ENPP is proportional to the time derivative of the carbon stored in the AGWB: $C_{seq}{=}f{\cdot}\mathrm{d}C_{stock}/\mathrm{d}t$, where f is the fraction of carbon in AGWB, f=0.5 for slow-growing tree species (mature stage) and f=0.45 for fast-growing tree species (young stage) Schöngart and Wittmann (2010). The individual C-stock of the principal species of trees, along their lifespan in várzea forest, was estimated with two allometric models (Cannell, 1984; Chave et al., 2005; Schöngart and Wittmann, 2010):

$$C_{stock}^{(1)} = \pi F \rho h (d/2)^2, \quad C_{stock}^{(1)} = 0.112\left(\rho h d^2\right)^{0.916} \tag{4.11}$$

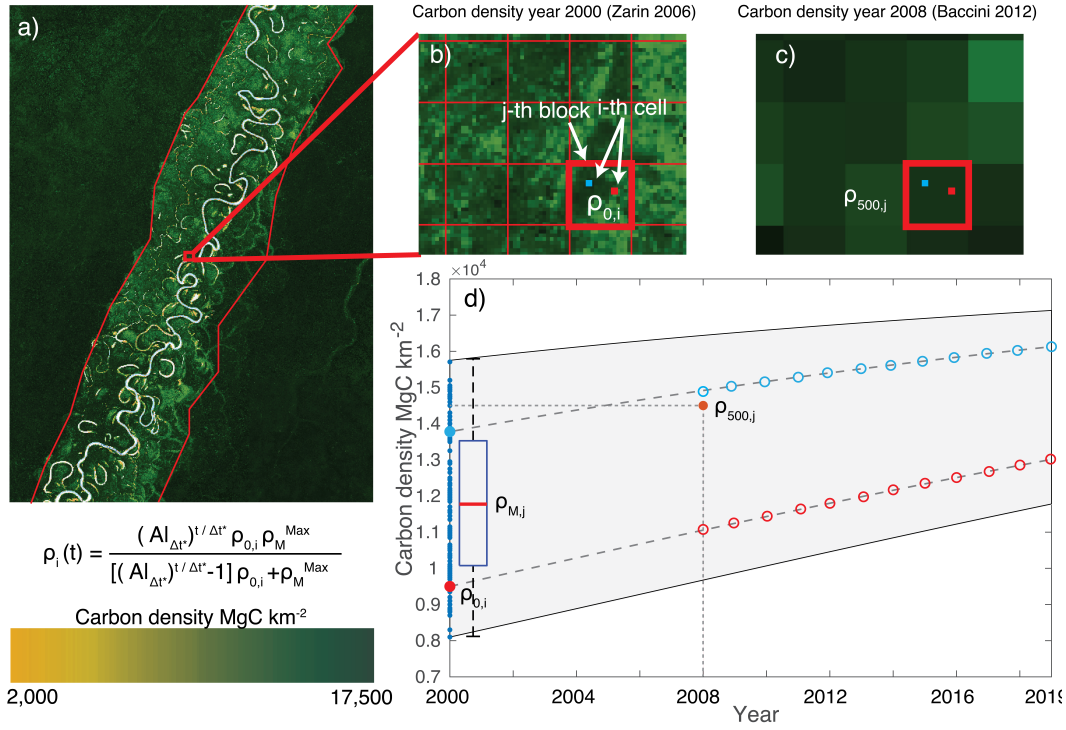

Fig. 4.5 **Application of the logistic growth update developed in Methods M2, through the use of equations** (4.9) **and** (4.10)**.** For each ROI (a) the value of carbon density of the generic pixel *i* was corrected in order to account the vegetation growth between the acquisition time (b) and the time of the forest loss (if occurred after 2008), through the equation (4.10). The model was calibrated by comparing the carbon biomasses reported by two different datasets with different acquisition times: i) dataset from ref. Zarin et al. (2016) acquired in 2000 (panel b); ii) dataset from ref. Baccini et al. (2012) acquired 2008 (panel c). In the case the forest loss occurred before 2008, the value of carbon density was not updated. An example of result for the extrapolated annual values of carbon density for two generic pixels are reported in panel d (blue and red open points), whereas the blue close points and the box-plot refer to the values of all cell within the j-th block at t=2000.

where d is the tree diameter (cm), h the total tree height (m), ρ the wood tree density (g/cm^3) and F=0.06 is a constant form factor assuming the taper does not change as the trees become larger. Equation 4.11a was used for Peruvian várzea forest and successional stages in Central Amazonia (Nebel et al., 2001; Worbes, 1997) while equation 4.11b was developed from dataset of tropical regions in America, Africa and Asia. Both models were tested for várzea floodplain, with fair agreement with field measurements (Schöngart and Wittmann, 2010). According to previous measurements of ring-widths and heights (Schöngart and Wittmann, 2010), we adopted the following growth models

$$h = \frac{da_2}{d+b_2}, \quad d(age) = \frac{a_1}{1+\left(\frac{b_1}{age}\right)^{c_1}}, \tag{4.12}$$

where the coefficients (a_1, a_2, b_1, b_2, c_1) for twenty-three dominant tree species of várzea (classified as: i) *short-living pioneers*, ii) *long-living pioneers*, iii) *emergent climax*, iv) *understorey climax*) are reported in the SI Appendix, SI Dataset S3. The results obtained for each of the twenty-three considered species were averaged, namely $C_{seq,j}$=$\frac{1}{n_j}\sum_{i=1}^{n_j} C_{seq,i}$, where j is the vegetation class, and n_j is the number of species belonging to the j-th class.

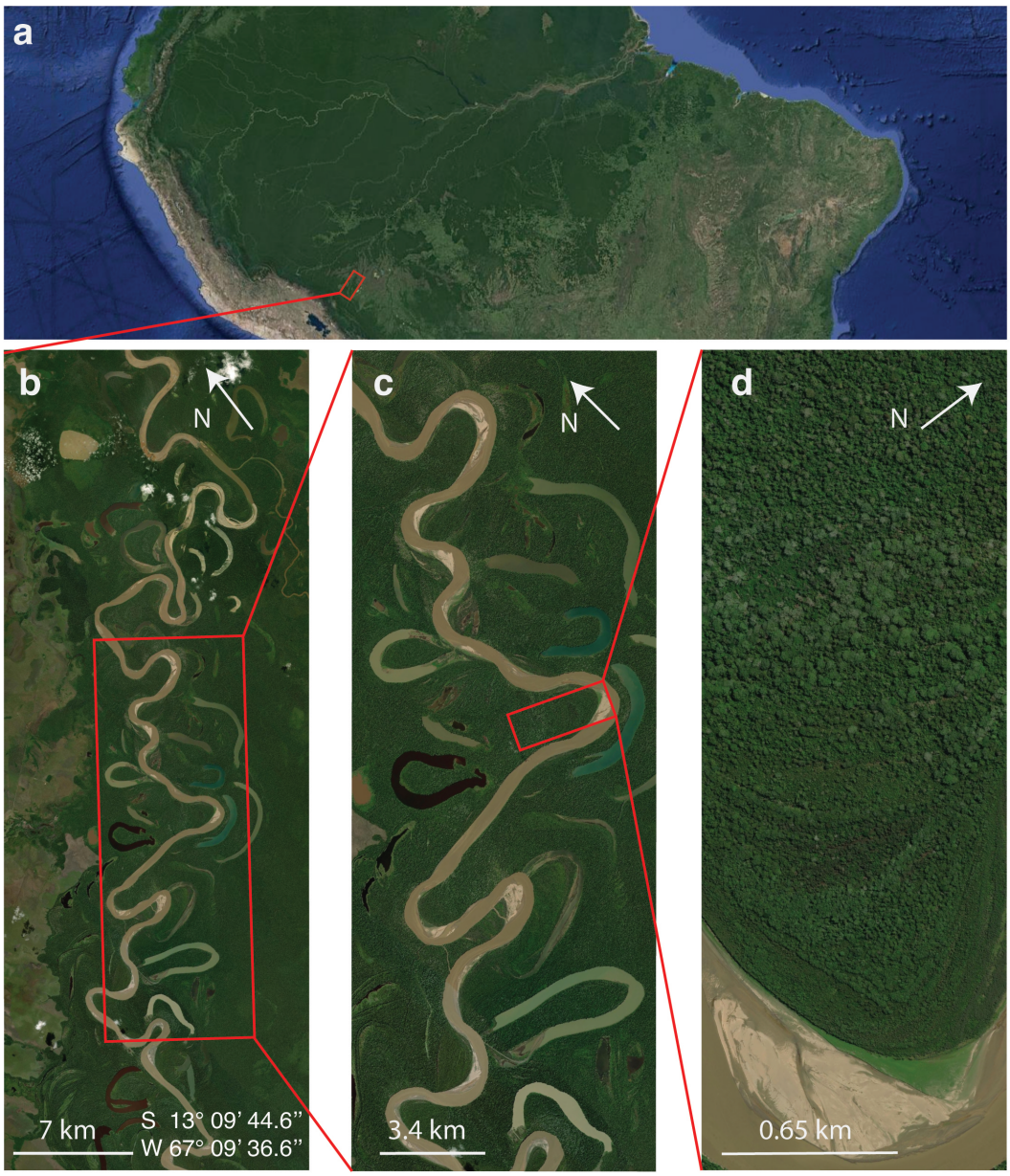

Fig. 4.6 Setting of the meander of Beni River reported in Fig. 5.3. Panel (d) corresponds to Fig. 5.3 of the main text.

4.6 Classification of the biomass distribution signatures

The analysis was performed using a set of Java APIs (Application Programming Interface), that are optimized for the analysis of big data. Due to the lack of an efficient and simple procedure for multi-modality detection Pfister et al. (2013), we also developed an ad-hoc classification algorithm that is able to distinguish four patterns in the biomass density distributions (negatively skewed, positively skewed, multi-modal, bell-shaped). The procedure combines the statistical parameters of the carbon density distribution across the ROI: mode (M), median (Med) and skewness (S_k). These parameters were calculated using a set of GEE-native geo-statistical functions, applied to the *WHRC Carbon Stock* Dataset Baccini et al. (2012). The minimum bin of histograms was fixed to 200 MgC/km^2 (the accuracy reported by Baccini et al. (2012) is 100 Mg C/ km^2). The algorithm was tested on a subset of 10% of the ROIs, randomly selected as a possible validation dataset, which showed a total accuracy of 95% (correctly classified distributions).

Firstly, the algorithm separates uni-modal from multi-modal distributions. To this aim, two sub-samples are extracted from the data-set of each ROI, by considering a cutoff at the median value of the carbon density distribution, referred to as the left- (L) and right- (R) sub-samples. ROIs' distribution are classified as multi-modal (MM) if two conditions are both satisfied: i) the frequency of the mode of the left (F_{ML}) or right (F_{MR}) sub-samples exceeds more than ± 10% the frequency of median value of whole sample (F_{Med}); ii) left (M_L) or right (M_R) modes are distant enough to the main median (Med), namely $|M_{L,R} - \text{Med}| > 400$ MgC/km^2. If conditions i) and ii) are both false, the skewness S_k of the main distribution is considered: positive skewness (S_k >0.4) provides PS, negatively skewed (S_k >-0.4) provides NS, whereas moderate skewness (-0.4< S_k <0.4) provides BS distributions. If only one of either i) or ii) is satisfied (i.e., just one sub-sample mode is detected to be distant from the median) the difference $D = F_{MR} - F_{ML}$ is computed to distinguish between NS ($D<0$) and PS ($D>0$) distributions. If the condition related to D is not satisfied (Fig. 4.7), the algorithm uses again S_k to classify biomass density distributions in NS, PS or BS classes.

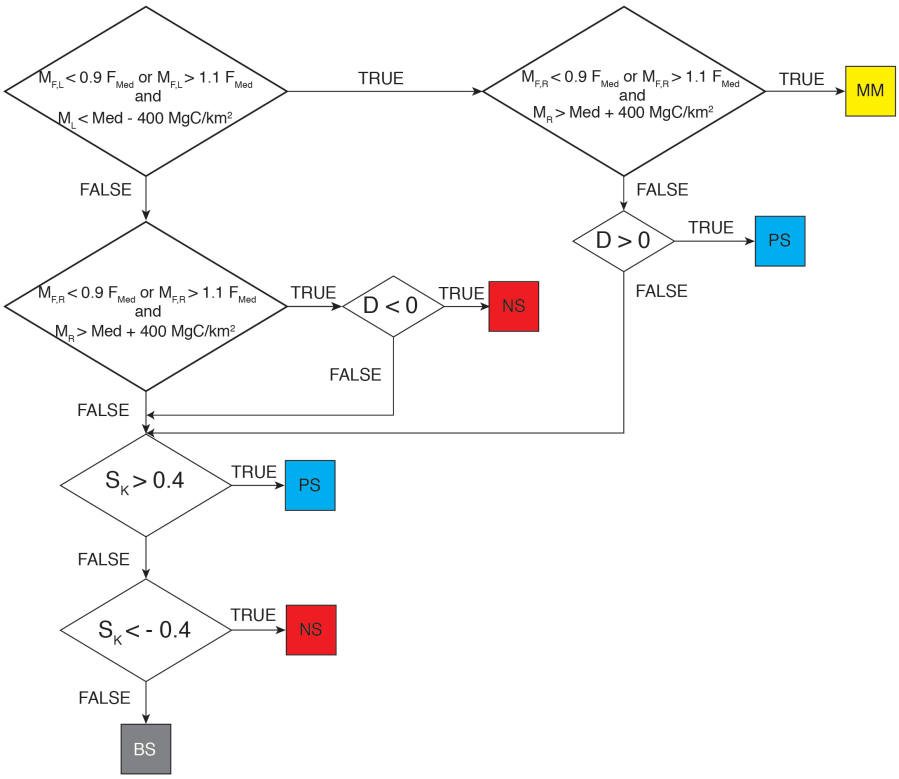

Fig. 4.7 Classification Algorithm

4.7 Uncertainty analysis

The aggregated continental eCE assessment for the largest tropical rivers was obtained as the sum of the values calculated in each ROI of the continent. The uncertainty (namely the standard deviation, henceforth referred to with symbol σ) at the pixel level may be computed from probability theory. The eCE is in fact the product of two quantities both affected by error (i.e., river-driven forest loss area and biomass carbon density) so they can be considered as random processes. According to the filtering procedure described above, for each pixel, forest loss can be associated with a discrete random variable $\chi_{j,k}$ that takes only two values: 1 with probability $P_{j,k}$ (RDFL) or 0 with probability 1-$P_{j,k}$ (non-RDFL). This corresponds to a Bernoulli process (Ross, 2009) –repeated coin flipping–, which has mean equal to $P_{j,k}$ and variance equal to

$$\sigma^2_{\chi_{j,k}} = P_{j,k}(1 - P_{j,k}). \tag{4.13}$$

The carbon density is instead a continuous random variable, with mean $\rho_{j,k}$ (from methods M1–M4) and standard deviation $\sigma_{\rho_{j,k}}$. By using Goodman's expression (Goodman, 1960) for the variance of a product of two uncorrelated random variables, the error variance of the eCE of pixel (j,k) reads

$$\sigma^2_{\mathrm{eCE}_{j,k}} = A^2_{j,k} P_{j,k} \left[\sigma^2_{\rho_{j,k}} + (1 - P_{j,k}) \rho^2_{j,k} \right], \tag{4.14}$$

where $A_{j,k}$ is the pixel area. Per-pixel values for $\sigma_{\rho_{j,k}}$ are not reported in the raw datasets herein considered, so we adopted different conservative assumptions, based on the observation that residuals are proportional to the mean, as also suggested in Baccini et al. (2012). Accordingly, in M1 and M2, we set

$$\sigma_{\rho_{j,k}} = C_{\mathrm{v}} \cdot \rho_{j,k}, \tag{4.15}$$

with the coefficients of variation C_{v} ranging between 0.5 and 1.25.

In M3 and M4, $\sigma_{\rho_{j,k}}$ was set to a constant value throughout the ROI, equal to the standard deviation of all the carbon densities measured inside the ROI, as reported in the *WHRC Carbon Stock* datasets Zarin et al. (2016) for M3, and the dataset by ref. Baccini et al. (2012) for M4.

As a further step, the propagation of the uncertainty from the pixel to the continental scale requires the assessment of the spatial correlation of the errors, otherwise per-pixel errors cancel out and the overall uncertainty may be largely underestimated. In the present case, standard use of spatial variograms (sensu Baccini et al. (2012)) are precluded by the spatial patchiness of ROIs, the heterogeneity of biomass due to river dynamics and in addition, because it is computationally prohibitive (even when encoded in GEE). Following Baccini et al. (2012), we therefore adopted two empirical autocorrelation length-scales (ALS) – ALS_1 equal to 500 m and ALS_2 equal to the ROI area – and we conservatively assumed that the pixels are perfectly correlated at a distance smaller than the ALS and uncorrelated at larger distances. The dataset was divided into independent blocks by using squares (for ALS_1) or ROI polygons (for ALS_2) and an upper conservative estimate of the uncertainties was calculated for each block by exploiting all the values of $\sigma_{\mathrm{eCE}_{j,k}}$ provided by aforementioned Goodman's formula within the block. For each method M1–M4, the uncertainty in the eCE at the continental scale $\sigma^2_{cont,ALS}$ was calculated for both ALS, by summation of the variance associated with each block within the continent: $\sigma^2_{cont,ALS}=\sum_i^N \sigma^2_{i,ALS}$, where N is the number of blocks in a continent and $\sigma^2_{i,ALS}$ is the variance error associated with each block.

For methods M3 and M4, the errors were assessed only with ALS_2, since in both scenarios the carbon density was derived from a spatial average at the ROI scale. In each block, the variance was calculated by taking its supremum over the block ($\sup_{(j,k)\in\text{block}} \{\mathrm{eCE}_{j,k}\}$). By combining methods M1–M4 with the two auto-correlation length-scales and considering the four values of C_v for methods M1 and M2, eighteen different configurations were considered for the uncertainty assessment (Table 5.1). The most conservative configuration (maximum uncertainty) gives standard deviation (in TgC/yr) and percentage error of 0.84 (9.78%), 0.36 (16.53%) and 0.29 (24.57%) for South America, tropical Africa and Asia/Oceania, respectively.

4.8 Downscaling

In the Horton-Strahler ordering system of the HydroATLAS dataset (Linke et al., 2019), the cutoff at the size of 200 m roughly corresponds to the order n=5. Since the finest resolution for cover loss was 30 m, we adopted a cautious approach and limited the downscaling of our results to rivers with widths in the interval 30–200 m

(i.e, n ~3–5). We first estimated the active wet surface AWS_r of a generic r-th reach with Horton-Strahler order $n \geq 3$ as the product of the reach lengths by the widths ($\mathrm{AWS}_r = l_{r,n} \cdot w_n$). The widths were computed as the trapezoidal mean of median stream widths recovered from published literature and satellite images (see Table 4.3),

Table 4.3 Trapezoidal mean of median stream widths, derived by Downing et al. (2012) from the published literature and measurements made using satellite images.

Horton-Strahler order (n)	3	4	5	6	7	8	9	10
width in meters (w_n)	29.3	73.3	131.5	264.5	608.5	803	988.5	3079

The mean biomass density of all the cell having a cover loss in a generic j-th ROI can be computed as $\bar{\rho}_j = \mathrm{eCE}_j / \sum_k L_{j,k}$. For any jth-ROI, Fig. 4.8 shows eCE_j plotted against the quantity $\bar{\rho}_j \sum_r \mathrm{AWS}_{j,r}$, where $\sum_r \mathrm{AWS}_{j,r}$ is the cumulative active wet surface of all the reaches with n≥3 in the ROI. The plot exhibits a nearly linear fit, with a mean y-to-x ratio

$$\beta = N^{-1} \sum_j \frac{\mathrm{eCE}_j}{\bar{\rho}_j \sum_r \mathrm{AWS}_{j,r}} = N^{-1} \sum_j \frac{\sum_k L_{j,k}}{\sum_r \mathrm{AWS}_{j,r}} = 0.0192, \tag{4.16}$$

where N=402 is the total number or ROIs. By using the HydroATLAS dataset (Linke et al., 2019), we estimated that the cumulative active wet surface of all tropical free flowing rivers with $n \geq 3$ is 207,000 km^2. After multiplying this value by the mean ratio β and the tropical mean carbon density $\bar{\rho}_{tr} = N^{-1} \sum_j \bar{\rho}_j$, we obtain an overall estimate of eCE for all tropical free-flowing rivers with $n \geq 3$, namely

$$\mathrm{eCE}_{\mathrm{all}} = \bar{\rho}_{tr} \beta \sum_{r,n} w_n l_{r,n}. \tag{4.17}$$

The uncertainty of this result was computed by combining the propagation of uncertainty, with the aforementioned probabilistic approach. In particular, the computation of the standard deviation of β accounts for the propagation of uncertainty in $L_j = \sum_k L_{j,k}$ and $\sum_{r \in \mathrm{ROI\text{-}j}} l_{r,n}$. The standard deviation of $\bar{\rho}_{tr}$ accounts for the propagation of uncertainty in eCE_j and L_j (see Sect. 4.7). Finally, after considering the resolution of the dataset HydroATLAS, we set $\sigma_{l_{r,n}}$=0.45 km.

After retrieving lengths and widths of all streams with $n \geq 3$, we estimated their eCE based on the quasi-linear link between the measured eCE and the total wet

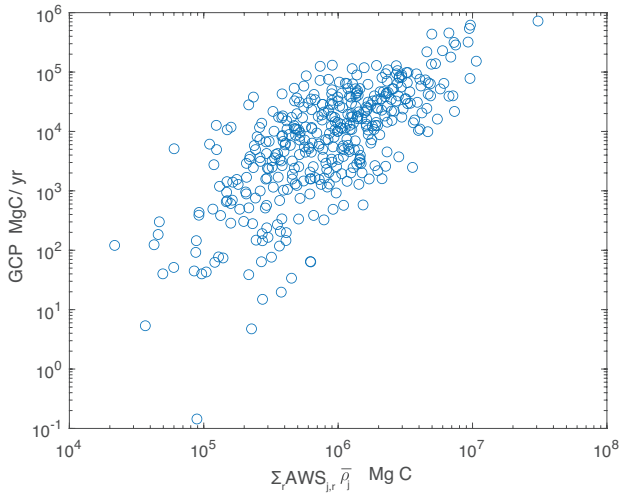

Fig. 4.8 eCE against the product of the wet surface area and the mean biomass density. Each point represents one ROI.

surface area in the ROIs (Fig. 4.8). We thus estimated that the eCE for the totality of free-flowing tropical rivers amounts to 49±8 TgC/yr, with small rivers contributing 75% of the total.

Chapter 5

Results

We analyzed the dynamics of all tropical rivers wider than 200 m in the period 2000-2019 and previously classified as *free-flowing* (Grill et al., 2019), i.e., weakly disturbed by anthropic activities. This resulted in a dataset of 162 large rivers embedded in 402 regions of interest (ROI), with a total fluvial length of 108,000 km and a total analyzed area of 403,000 km^2 (of which ~62,000 km^2 is active wet surface, see Methods). Through remote sensing analysis of satellite datasets developed on the free-access cloud computing platform Google Earth Engine (GEE, ref. Gorelick et al., 2017, Table 4.1), we focused at the area in the river corridor that had a vegetation loss due to river dynamics. With a probabilistic classification mapping (Chapter 4), this area was estimated to be 17,693 km^2 during 2000-2019, which corresponds to an annual forest loss of 931 km^2/year. Under stationary natural conditions, neither vegetation biomass removal nor production prevails and the eCE and ENPP processes equalize each other.

5.1 Eco-morphodynamic carbon export at the global scale

Forest losses were combined with biomass densities to assess the strength of the Eco-morphodynamic Carbon Export (eCE) and its value per unit ROI area: eCE_A (Methods). We estimated that large tropical rivers in South America, Africa, and Asia/Oceania respectively export 8.90 ± 0.84, 2.23 ± 0.36, and 1.32 ± 0.29 TgC/yr

of woody biomass carbon from riparian corridors (total eCE = 12.38 ± 0.96 TgC/yr; eCE_A = 30.8 ± 0.42 MgC/km^{2}yr, Fig. 5.1, Table 5.2). Overall, half of the total carbon export is due to just nine rivers (6%) – *Big exporters* – each contributing eCE > 305 GgC/yr. The areas dynamically affected by these rivers occupy 35% of the total area considered. They include: i) *Extensive Exporter* (eCE_A <50 MgC/ km^{2}yr), which are major contributors due to their large fluvial corridors, such as the Rio Negro; ii) *Intensive Exporters* (eCE_A >90 MgC/ km^{2}yr) with less extensive fluvial corridors but high migration rates ($M_r > 4 \cdot 10^{-2}$ channel widths per year, ref. Constantine et al., 2014), such as Ucayali.

Rivers smaller than 200 m wide were excluded from the above analysis. However, because of their abundance, small lowland rivers are likely to be important contributors to the overall eCE. It is also possible to provide an indirect–albeit less accurate, but probably conservative–assessment of eCE for smaller river reaches (i.e., width=30-200 m). Accordingly, after a down-scaling procedure the overall estimate of tropical eCE is almost quadrupled (49±8 TgC/yr, Section 4.8). Yet, this latter estimate requires a further scrutiny.

Table 5.1 Results about the aggregated continental eCE (by using the methods M1-M4) and the corresponding uncertainties, for the largest tropical free flowing rivers (width >200 m.)

Methods	Continental eCE (TgC/yr)			Autocorrelation scale	Carbon uncertainties	Continental eCE uncertainties (TgC/yr)		
	America	**Africa**	**Asia**			**America**	**Africa**	**Asia**
M1	8.60	2.20	1.17	500 m	50% $\rho_{j,k}$	0.06	0.03	0.02
					75% $\rho_{j,k}$	0.09	0.04	0.03
					100% $\rho_{j,k}$	0.12	0.06	0.05
					125% $\rho_{j,k}$	0.15	0.07	0.06
				ROI scale	50% $\rho_{j,k}$	0.39	0.17	0.13
					75% $\rho_{j,k}$	0.51	0.22	0.18
					100% $\rho_{j,k}$	0.67	0.29	0.23
					125% $\rho_{j,k}$	0.84	0.36	0.29
M2	8.89	2.23	1.25	500 m	50% $\rho_{j,k}$	0.06	0.03	0.02
					75% $\rho_{j,k}$	0.09	0.04	0.03
					100% $\rho_{j,k}$	0.12	0.06	0.05
					125% $\rho_{j,k}$	0.15	0.07	0.06
				ROI scale	50% $\rho_{j,k}$	0.39	0.17	0.13
					75% $\rho_{j,k}$	0.51	0.22	0.18
					100% $\rho_{j,k}$	0.67	0.29	0.23
					125% $\rho_{j,k}$	0.84	0.36	0.29
M3	7.91	2.01	1.02	ROI scale	Spatial St.Dev. ρ	0.22	0.09	0.06
M4	8.62	2.11	1.01	ROI scale	Spatial St.Dev. ρ	0.23	0.09	0.06

5.2 Description of eco-morphodynamic carbon export at continental scale

The Amazon basin and corresponding tributaries can be divided into three geomorphologically homogeneous sub-regions (Fig. 5.2). The upstream region, corresponding to the Peruvian-Bolivian Amazon basin, is the most dynamic one (eCE=4,283 GgC/yr) with high levels of sinuosity, bank erosion rate and channel migration. The Lowland Rainforests in such a region are heavily influenced by lateral erosion of meandering rivers and new sequential succession forest develops on scroll bars very rapidly, while most of the (mature) mosaic vegetation loss is on the outer bank or in the short-lived islands (Salo et al., 1986).

The middle region (eCE=3,132 GgC/yr) is characterized by a lower erosion rate and more stable channel banks. Meandering rivers (e.g., such as Purus, Jurua, Jutai) have migration rates lower than 0.2 channel-widths/yr (Constantine et al., 2014) (because of the low levels of sediment transport, see Fig. 2j) and a GPC_A between 1.4 and 100 MgC/km^2/ yr. The Amazon river corridor of this region is characterized by an increase in the recurrence of low-waters, and green grass and shrubs species colonize a rising portion of wetlands with the consequent reduction of woody plant communities (Hess et al., 2003). For instance, the Negro river corridor (a tributary of the Amazon River in Central Amazonia) is characterized by relatively lower biomass density where swamp forest (igápo) and white sand vegetation populate stable islands (Lima et al., 2012). The downstream subregion (e.g. Jurunea, Rio Mapuera) provides the lowest levels of eCE in the Amazon basin (eCE=1,079 GgC/yr, eCE_A=19.4 MgC/km^2 yr). The Amazon river corridor is here populated by dish-shape lakes in the floodplain and herbaceous vegetation is widespread. Carbon pumping is dominated by recurrent floods, so vegetation remains at immature stage and biomass density is usually low (<53 MgC/ha). However, the amount of carbon sequestrated remains high due to a high river-land connectivity (800 GgC/yr) while eCE_A is lower than the upstream zone. Others rivers outside the Amazon Basin (Orinoco basin) and rivers of Central America sequestrate 407 GgC/yr with eCE_A that ranges between 1 and 102 MgC/km^2 yr (mean value: 17 MgC/km^2).

African eCE is mainly due to the Congo basin, which can be divided in two subregions. The upper region (the Upper Congo river and Lowa river) is characterized by dense forest with high values of the above-ground biomass (120 MgC/ha). The

Table 5.2 Estimates of Eco-morphodynamic Carbon Export (eCE) and River-Driven Forest Loss Area (A_{RDFL}) for the largest tropical rivers. Values in parentheses indicate percentage relative to total eCE=12.45 Tg C/yr. Uncertainty analysis is described in Methods.

Basins	eCE_A [MgC/km^{2}yr]	eCE [TgC/yr]	A_{RDFL} [km^2/yr]
America			
Upstream Amazon	63.6	4.28(34.4%)	295
Central Amazon	24.7	3.13 (25.2%)	212
Downstream Amazon	19.4	1.08 (8.7%)	94
Others	17.2	0.41 (3.3%)	36
Africa			
Upstream Congo	53.7	1.65 (13.3%)	118
Downstream Congo	31.8	0.34 (2.8%)	30
Others	10.6	0.18 (1.4%)	21
Madagascar	14.4	0.06 (0.5%)	9
Asia			
New Guinea Island	12.9	0.18 (1.4%)	14
Borneo Island	71.3	0.7 (5.6%)	61
Sumatra Island	100.3	0.22 (1.8%)	21
Malay Peninsula	149.8	0.13 (1.0%)	11
Others	20.3	0.09 (0.7%)	8
Major Exporters			
River	eCE [Tg C/yr]	Rivers	eCE [Tg C/yr]
Amazon	2.6 (21.2%)	Congo	0.37 (2.9%)
Ucayali	1.4 (11.5%)	Ubangi	0.32 (2.5%)
Rio Negro	0.42 (3.4%)	Lualaba	0.31 (2.5%)
Purus	0.38 (3.1%)	Maranon	0.31 (2.5%)
Kapuas	0.37 (3.0%)		

vegetation is here mainly removed by overflow and uprooting, the planforms are stable and long-lived and vegetation populates both the floodplain and the riparian corridor. In contrast, the central-downstream region of Congo basin represents one of the world's most extensive swamp forest, that is supposed to host a huge peat deposit (30.6 PgC, ref. (Dargie et al., 2017)). Nevertheless, the density of above-ground biomass is modest (66 MgC/ha) and the mean sequestration capacity is 31 MgC/km^2 yr. The remaining African basins sequestrate only 177 GgC/yr^{-1}. This is due to a

low tree cover and aboveground carbon density (39 MgC/ha) that characterize arid and semiarid zone.

The Indonesian and New Guinea forest has a relevant carbon store (18.6 PgC, ref. Baccini et al., 2012), but it experimented an important conversion from tropical forest to oil palm plantation (Morel et al., 2011). Also the historically unaltered wetland forest has lost ~ 52,000 km^2 of cover between 2000 and 2012 (Margono et al., 2014), probably due to agro-industrial land development (Margono et al., 2014). These aspects are not related to fluvial dynamics, and make the assessment of river-induced forest loss more uncertain (see Table 5.1). Our assessment of carbon sequestrated by Indonesian basins is 1,840 GgC/yr and eCE_A ranges between 2.9 and 149.8 MgC/km^2yr (mean value: 54.4 MgC/km^2yr).

5.3 The nexus between sediment transport, migration rate and carbon export

As pointed out by Constantine et al. (2014), the whitewater rivers in the Andean-foreland basin – Ucayali, Huallaga, Beni and Maranon - are highly dynamic due to the high suspended sediment load they carry (0.23 ±0.16 Mt/year). In fact, the suspended load in these catchments was found to be positively correlated with river migration rates (Ahmed et al., 2019) because sediment transport increases the buildup of fluvial bars, which enhances the topographic steering of longitudinal flow (Dietrich and Smith, 1983) and thus promotes shear stress and bank erosion (Camporeale et al., 2007). Such a key phenomenon, combined with the nutrient-rich sediment and high biomass density (80–161 MgC/ha) of fluvial corridors in the Andean-foreland basin, makes it the most active basin in the world for carbon transport (34.4% of the total eCE of large tropical rivers). Our reanalysis of 14 selected rivers of the Amazon basin, whose migration rate per unit width M_r was already known, suggests that eCE is positively correlated with M_r and/or the total suspended sediment TSS (Fig. 5.1l), and strongly supports our hypothesis of morphodynamically driven carbon export.

Similar to the C-sink triggered by erosion of topsoil layers (Van Oost et al., 2012), we therefore claim that river morphodynamics induces the recruitment of wood from riparian vegetation through erosion and uprooting and promotes colonization and

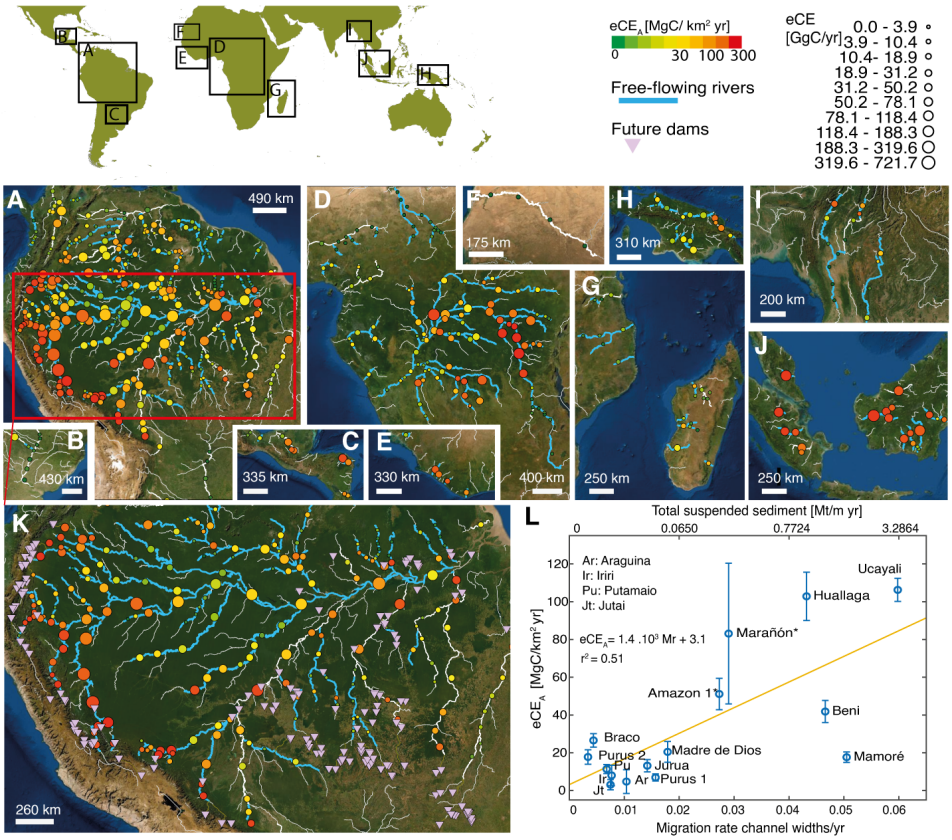

Fig. 5.1 Eco-morphodynamic Carbon Export (eCE) of the world's largest tropical rivers (overall 402 ROIs). (a) South America, (b) Northern Argentina, (c) Mexico, (d) central Africa, (e) Central West Africa, (f) West Africa, (g) southeast Africa, (h) Papua and New Guinea, (i) Southeast Asia, (j) Borneo and Sumatra. Point size is proportional to eCE, colors show eCE_A. Blue reaches indicate free-flowing streams (CSI index > 95%, after ref. Grill et al., 2019). (k) Magnified view of Andean-foreland forest basin and distribution of planned new large hydroelectric dams (>1 MW, see Zarfl et al. (2015)) shown by pink triangles. (l) Correlation between sediment transport, migration rate, and carbon export (data on migration rate and sediment transport from ref. Constantine et al. (2014), in the river marked * we derived migration rate from M_r=0.043·$TSS^{0.28}$, as suggested by Constantine et al. (2014)).)

rejuvenation of the riparian zone (Wohl et al., 2019). The more the carbon export induced by river dynamics, the larger area is freed, the higher the colonization of new vegetation, thus fostering further NPP. If for any reason, lateral erosion, uprooting, and overflow were interrupted, then C-export would be reduced and rejuvenation of the floodplain inhibited.

Fig. 5.2 Zonation of river basins

5.4 Enhanced Net Primary Production

An example of computation of the ENPP for a meandering river (Beni river, Brazil) is provided in Fig. 5.3. The riparian zone of Beni river is part of Várzea forest, whose trees grow in zones periodically inundated by rich-nutrient sediment whitewater rivers, drained from the Andes. This is a highly dynamic ecosystem wherein young trees in newly deposited point bars are highly efficient in C-fixation, whereby the above-ground NPP of young successional stage of várzea forest is among the largest of tropical forest (Schöngart and Wittmann, 2010).

We estimated the ENPP in a point bar, i.e. the carbon sequestrated by the Above Ground Woody Biomass (AGWB) (Section 4.5). Fig. 5.3d shows that C-sequestration of individual trees increases rapidly during the first 50-80 years of successional growth, and then remains stationary (solid curve). Short living pioneer species (such as genus *Salix*, Fig. 4.6) dominate the young stages, and are then followed by a secondary stage dominated by long living pioneers (e.g., *Cecropia* sp., ref. Worbes, 1997). Pioneer tree species at the young successional stage are more exposed to sunlight and have much higher photosynthetic rates than species at the late-successional stage.

The shift in the species composition during the successional sequence is associated to a structural change. The dashed curve in Fig. 5.3d shows the temporal trend of population density of várzea, i.e., the number of individuals per unit area (Worbes, 1997). The population density rapidly decreases after the maximum (~35 $\times 10^4$ indv./km^2) at the stand age of about 10 years. In old stands, the species of climax forest dominates, absorbing light and colonizing bars, and the population density becomes seven-fold lower than in young stands (~5×10^4 indv./km^2). It follows that, although the C-stocked in non-flooded mature forest is 136-151% higher than várzea forest (Chambers et al., 2001; Schöngart and Wittmann, 2010), the stand C-sequestrated is instead 47%-59% lower (Fig. 5.3e). Furthermore, mature vegetation (stand age >100 years), which has a lower sequestration capability, is likely uprooted during flood events and thus is delivered into the aquatic system and replaced by highly productive young trees.

It is noteworthy that at the early stage, the product between the high C-sequestration capability of pioneer species and their high population density peaks the stand C-sequestration. In fact, Fig. 5.3e shows that the overall net C-sequestration across the

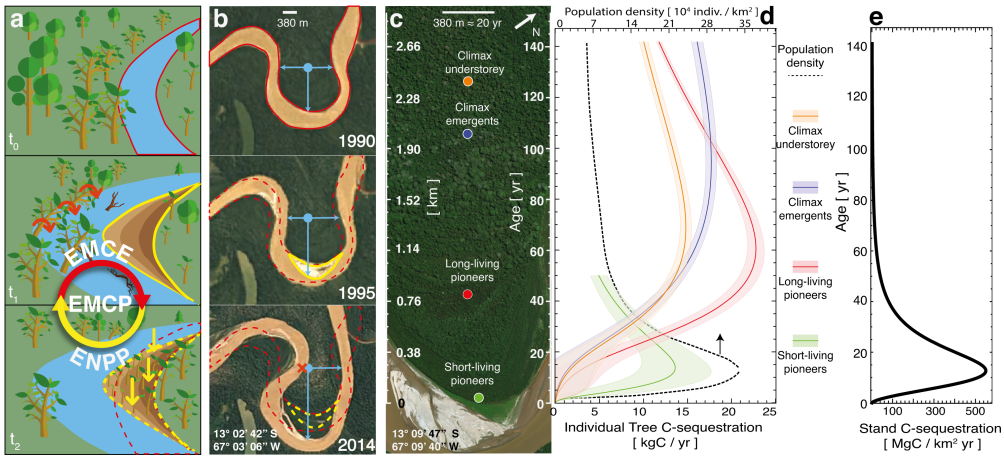

Fig. 5.3 (a) Conceptual scheme of eCP as a result of eCE (red arrow) and ENPP (yellow arrow), in the case of a migration-driven capture of woody biomass from the outer bank and exported into the stream (see also SI Appendix, Fig. S1). (b) The 25-year time-lapse of migration and folding in the Beni river (zoom-out in SI Appendix, Fig. S3) showing the change in relative distances between a generic point and the river (blue arrows). (c) Cross-section of Beni River's point bar, with double axes linking stand age to the distance from the river, assuming mean migration rate ~20 m/yr Ahmed et al. (2019). (d) Individual tree-sequestration of different plant typologies in Várzea forest (mean values and standard errors reported through colored bands) and population density (dashed curve from Junk, 1997a) from a reanalysis of data by Schöngart and Wittmann (2010). (e) Stand C-sequestration, namely the individual C_{seq} times the population density (modified after Schöngart and Wittmann, 2010), which identifies a highly productive inner riparian corridor populated by pioneer species (<40 yr).

successional gradient (i.e., considering the whole community) peaks at the stands with age of 20 years. Afterwards, when the stand is more than 100 years old, net C-sequestration reduces nearly to zero. The main reason is that recruitment of mature stands depends on floodplain erosion and reworking associated to the folding of meanders. Indeed, this non-local process (Guo et al., 2019) causes the relative distance between points on scroll bars and the meander banks to increase along one direction, whilst decreasing along the other (blue arrows in Fig. 5.3b). Sooner or later, the vegetation growing on such locations will again be removed by river meandering dynamics. It follows the filtering of riparian communities as a result of the matching between the age of the most mature-less productive plants and the meandering timescale T_m (e.g., Junk, 1997a). This is the mean recurrence time of the river centerline for the plots in the floodplain and it is also equal to the reciprocal of the annual regeneration rate of the floodplain.

From the analysis of the Landsat images of Beni River (Fig. 5.3c), the mean annual regeneration rate was 1-2.5% in the period 1987-2001 (Gautier et al., 2007), and similar rates were reported for the Manu River (Salo et al., 1986). These values correspond to T_m=40-100 years, in agreement with the observation that stands older than 50 years perform the lowest population density and a stand C-sequestration nearly null after 100 years (Fig. 5.3e). Given the mean channel migration rate (20 m/yr, for Beni river), this timescale is linked to a spatial scale (~2 km), that defines the most productive region, and allows for the pairing between eCE and ENPP.

5.5 Carbon signatures

Large unconfined fluvial systems that are characterized by river dynamics can be divided into two groups: (i) multi-thread; and (ii) single-thread systems (Wohl and Ogden, 2013). The former refers to braided and wandering rivers that are *elevation*-dominated, whereby flooding removes or buries vegetation leading to large elevation change rates related to deposition/erosion, while maintaining the fluvial system in an immature, but highly productive stage – in accordance with the Intermediate Disturbance Hypothesis (Ward and Stanford, 1995) and the Flood Pulse Concept (Junk, 1997a). Instead, the latter, single-thread systems, refer to sinuous/meandering streams that are *planimetry*-dominated, whereby lateral erosion and deposition act antithetically, thus producing vegetation reallocation in the fluvial corridor. From the

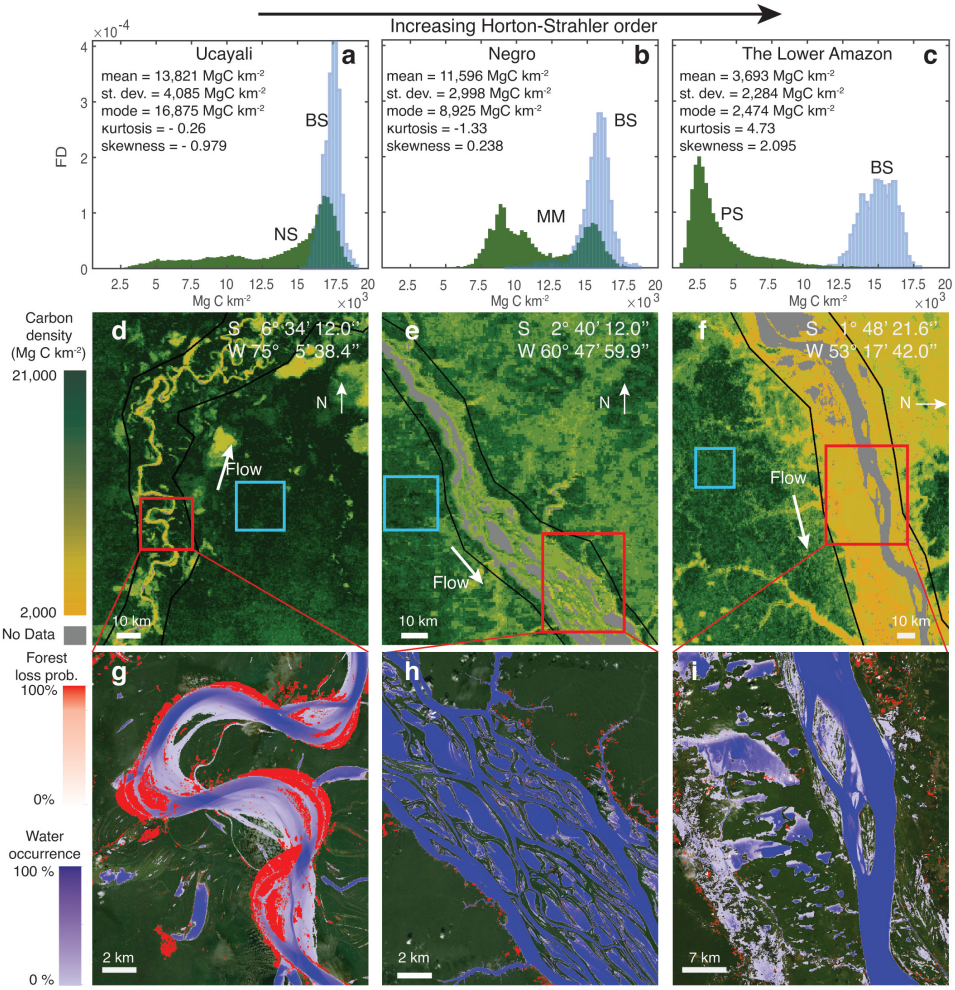

Fig. 5.4 Signature of planforms on carbon density distributions for a meandering river (Ucayali), and two multi-thread rivers (Negro and the Lower Amazon). (a-c) Frequency distribution of biomass carbon density. Green histograms refer to the entire ROIs reported in panels d-f (black polygons), blue histograms refer only to the region in the blue box (i.e., where river dynamics do not affect vegetation). NS : negatively-skewed; MM: multi-modal; PS: positively-skewed; BS: bell-shaped. d-f) Maps of carbon density distribution for corresponding regions based on dataset by Baccini et al. (2012); g-i) River-driven forest loss probability P (red) over 2000-2019 (see Methods) and water surface occurrence (blue) from the dataset by Pekel et al. (2016).

analysis of the *WHRC Carbon Stock* dataset (Baccini et al., 2012), some distinctive signatures in the carbon distribution are recognizable, which provide a proxy of the sequestration capability of the rivers.

We observed that eco-morphodynamic carbon export leaves a morphology-dependent footprint in biomass distribution, because the downstream gradiens in waterlogging duration (also called hydroperiod) and fluvial planforms Through the analysis of the *WHRC Carbon Stock* dataset (Baccini et al., 2012), and a new clustering algorithm, we identified four signatures of fluvial biomorphological activity evident in biomass distributions within ROIs (Fig. 5.4, Fig. 5.5, Table 5.3): negatively-skewed (NS, 39.0% of observations), positively-skewed (PS, 26.8%), multimodal (MM, 25.5%), bell–shaped (BS, 8.7%). We observed that fluvial corridors follow the NS-MM-PS longitudinal sequence fairly closely with increasing the Horton-Strahler number (Rodriguez-Iturbe and Rinaldo, 2001), a scenario evident in the Amazon River (Fig. 5.5I). Such signatures are a proxy for the export capacity of rivers and demonstrate the link between sediment transport, flood pulses, river morphodynamics, and carbon pumping.

In single-thread sinuous/meandering rivers with high migration rates, lateral erosion removes the mature forest, while deposition provides new fertile ground for juvenile vegetation colonization. The hydroperiod (i.e., the mean duration of seasonal floods) is short enough to allow forest to reach mature condition and store a high amount of carbon. Instead, the point bars and bare banks are rapidly vegetated by seedling and young trees with high sequestration capability but with low carbon density. Thus, the carbon distribution is negative-skewed with a peak representing the mature forest and a left tail dues to seedling.

In multi-thread (braided/wandering) rivers, intermediate-to-high fluvial disturbances affect the vegetation that populates islands and banks. At weakly disturbed conditions (short hydro-period), a mature forest populates islands, or central bars, in the inner cores while young trees develop along the banks. Such a mixture of mature and young vegetation is recognizable as a multi-modal distribution in the carbon density. With the increasing of the hydro-period, the development of mature vegetation in the islands cores is progressively inhibited and the system remains at an immature stage, so inducing a positively-skewed carbon density distribution.

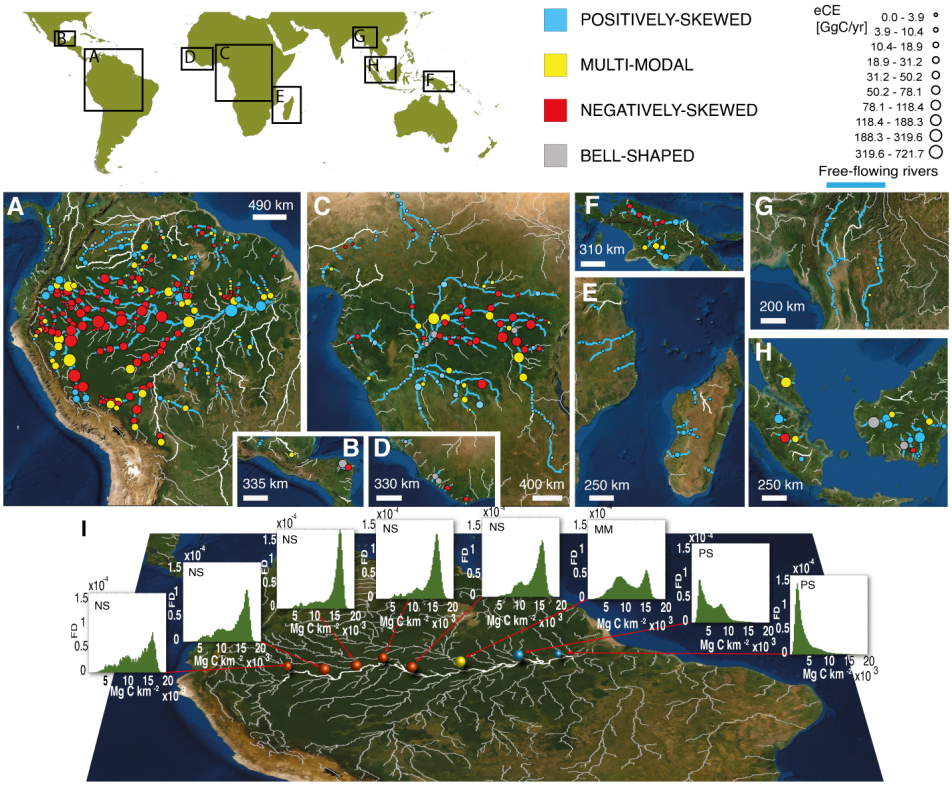

Fig. 5.5 Maps of the carbon signature of the world's largest free-flowing tropical rivers in America (A, B), Africa (C-E) and Asia (F-H). All the outcomes are reported in Table S3. (I) Longitudinal sequence of signatures in the frequency distribution (FD) for Amazon River corridor biomass density (NS: negatively skewed; MM: multimodal; PS: positively skewed.)

5.6 Opportunities for water management

The eCP process is closely linked to the ability of river systems to recruit vegetation and sustain the rejuvenation of the riparian corridor. However, the river activity – carbon export nexus is broken when fluvial connectivity is undermined by anthropogenic activities. For example, dams and reservoirs impact the frequency and duration of flood pulses in the river network (Timpe and Kaplan, 2017) and can reduce the input of bedload and suspended sediment to the downstream reaches (Finer and Jenkins, 2012), resulting in channel narrowing and incision (Wohl et al., 2015). Lower flood pulses and sediment supply can also greatly alter riparian vegetation dynamics (Bertagni et al., 2018) by reducing seedling establishment, increasing vegetation encroachment, and leading to even-aged riparian forests (Camporeale et al., 2013).

Table 5.3 Results of the classification algorithm and partition of the carbon signature at continental scale. NS: negatively skewed; MM: multi-modal; PS: positively skewed; BS: bell-shaped.

	NS	MM	PS	BS
Catchment scale				
America				
Upstream Amazon Basin	66.7 %	22.2 %	11.1 %	0 %
Central Amazon Basin	60.0 %	30.7 %	5.3 %	4.0 %
Downstream Amazon Basin	27.4 %	45.4 %	15.1 %	12.1 %
Others	18.5 %	29.6 %	38.9 %	13.0 %
Africa				
Upstream Congo Basin	54.3 %	28.3 %	8.7 %	8.7 %
Downstream Congo Basin	4.2 %	20.8 %	70.8 %	4.2 %
Others	15.9 %	6.8 %	47.7 %	29.6 %
Madagascar	0.0 %	0.0 %	100.0 %	0.0 %
Asia				
New Guinea Island	50.0 %	25.0 %	25.0 %	0.0 %
Borneo Island	7.7 %	15.4 %	61.5 %	15.4 %
Sumatra Island	25.0 %	25.0 %	50.0 %	0.0 %
Malay Peninsula	0%	100.0 %	0.0 %	0.0 %
Others	0%	50.0%	50.0 %	0.0 %
Continental scale				
America	47.9 %	29.9 %	16.2 %	6.0 %
Africa	26.7 %	16.9 %	41.9 %	14.5 %
Asia	23.5 %	26.5 %	44.1 %	5.9 %
Global scale				
Tropics	39.0 %	25.5 %	26.8 %	8.7 %

The connectivity of river systems worldwide was recently assessed using an integrated index (CSI, *sensu* ref. Grill et al., 2019) that considers river fragmentation, flow regulation, sediment trapping, water consumption and infrastructure development. For an additional group of 114 river segments (33,700 km) classified as *moderately altered* (i.e., CSI<95%, see white reaches in Fig. 5.1a-k), we found that their eCE_A was 40% lower than free-flowing rivers. This suggests that a loss of river connectivity reduces eCE.

These results reinforce concerns about the environmental vulnerability of rivers to dams in the Neotropics (Latrubesse et al., 1957), where 101 large hydropower dams are planned in Peru and Bolivia with a total installed capacity of 46 GW (Almeida et al., 2019). These dams are mostly located upstream from the major

carbon exporters in South America (pink triangles in Fig. 5.1k). If the new power plants were to break the sediment load linkage between the Amazon and the Andes, the migration rate of the *big exporter* of the Upstream Amazon basin would be greatly reduced, as also previously suggested by the Fluvial Dynamic Index (Latrubesse et al., 1957). Our analysis suggests a loss in carbon pumping equivalent to 4,283 MgC/year (Table 5.2) if river morphodynamics will cease. When these impacts are taken into account, the carbon intensity of the new Peruvian and Bolivian dams (i.e., CO_2-equivalent emissions per unit of electricity generated) increases from 238 $gCO_{2eq}kWh^{-1}$ (Almeida et al., 2019) to 277 $gCO_{2eq}kWh^{-1}$, a value nearly three times higher than the United Nations Agenda 2030 recommendation for sustainable global electricity generation.

In conclusion, a carbon budget approach to managing regulated rivers in the Neotropics is therefore essential to determine whether hydropower can be considered a clean energy source in the future.

5.7 Strength and weaknesses

The proposed eCE evaluation procedure is exportable to other locations. It is based on the processing of satellite products freely available on GEE (see Table 4.1) and does not require special calibration. The datasets used for the assessment of forest loss caused by river dynamics are updated annually, allowing continuous updating of the eCE assessment. In addition, the procedure is fully implemented on GEE, thus significantly reducing computational costs and storage space.

The study analyses free-flowing river. Although river regulation or anthropogenic impacts in general considerably reduce eCP (see Section 5.6), they do not totally cancel it out. As many as 77% of rivers longer than 1000 km are anthropically impacted (Grill et al., 2019), so their contribution in the phenomenon should be analyzed. However, the high level of disturbance that very often characterizes these waterways makes the presented methodology poorly constrained for their analysis, and further analysis and field measurements are needed.

The eCE assessment procedure is suitable for analyzing watercourses with channel widths greater than 200 m. This restriction is mainly due to the resolution of the datasets used. With appropriate adjustments, we also downscaled the result for rivers

between 200 and 30 m but the reliability of this result is lower. And finally, we can say nothing for rivers with widths less than 30 m. Globally these rivers represent about 89% (length) of the waterways (Downing et al., 2012). In addition, headwaters are recognized as conveyors of coarse woody material and producers of POM (Evans, 2022). Not considering them in a global estimate leads to an underestimation of the value of eCE.

Part III

Effect of river alteration on floodplain forest

The contents of the present Part has been partially derived from Salerno et al. (2022).

Chapter 6

River alteration in floodplain vegetation of the Amazon Basin

Floodplain forests represent about 14% of the Amazon Basin area (Flores et al., 2017) and are highly productive riverside areas, heavily influenced by both terrestrial and fluvial dynamics (Junk et al., 1989). As seen in Part III, river dynamics play a key role in defining the distribution of biomass in floodplain. The seasonal pattern of precipitation over the Amazon catchments drives a predictable mono-modal annual flood pulse in the unaltered large rivers (Junk et al., 1989, 2014; Schöngart and Junk, 2007).

The natural annual cycle of rising, high, and low water levels, has a strong impact on floodplain forest dynamics acting as a filter that selects a wide variety of flood-adapted species tolerating up to 6-8 months with flooding and up to 10 m of water depth (Junk, 1997b; Junk et al., 1989; Lewis et al., 2000; Wittmann et al., 2004, 2010). Moreover, the tree endemic species that populate the different topographic levels of floodplains, synchronize their phenology with periodic flood events, water levels, and sedimentation cycles (da Rocha et al., 2019; Ferreira et al., 2010; Junk, 1997b; Parolin and Wittmann, 2010; Worbes, 1997).

These complex interactions between water and vegetation life-cycle make the floodplain forests extremely sensitive to hydrological changes due to anthropogenic and natural disturbances. Any kind of alterations in the original hydro-geological drivers can represent a strong stress for riparian species. Long-term negative environmental consequences range from forest degradation, changes in the floristic

composition, and reduction of biodiversity, up to the ecological regime shifts in the worst cases (Tockner et al., 2010). Among the anthropic alterations of the riverine environment, the modifications of flood pulse due to hydropower dams may be particularly severe. Many studies have unraveled the impacts of hydroelectric dams (Almeida et al., 2019; Kahn et al., 2014; Kuriqi et al., 2021), highlighting the social, economic and environmental negative repercussions (Agostinho et al., 2018; Assahira et al., 2017; Castello and Macedo, 2016; Cochrane et al., 2017; Fearnside, 2002, 2014; Fearnside and Pueyo, 2012; Nilsson and Berggren, 2000; Poff and Hart, 2002; Timpe and Kaplan, 2017). Furthermore, the consequences of large damming are not only limited to the area near the infrastructure, but also affect floodplains downstream and the estuarine environment at large scales (Andersson et al., 2000; Castello and Macedo, 2016; Latrubesse et al., 1957; Merritt and Wohl, 2006; Tealdi et al., 2011). The Amazon basin has a very large number of existing dams (151) with 358 dams planned and under-construction (Zarfl et al., 2015); this makes the amazonian floodplains one of the most threatened ecosystems in the world (de Resende et al., 2020; Kahn et al., 2014; Lees et al., 2016).

The hydroelectric damming may alter the natural flood pulse and disrupt river connectivity (Grill et al., 2019), with serious repercussions on floodplain vegetation (Assahira et al., 2017; da Rocha et al., 2019; de Resende et al., 2019). da Rocha et al. (2019) found that in areas with a drastic reduction of flooding, upland forest species started competing with endemic species by encroaching the floodplains, while in the areas with extreme prolonged flooding the establishment of any species was impeded. Recent studies (Assahira et al., 2017; de Resende et al., 2019) on a regulated river of the Amazonas state (*Uatumã*) have documented, in the lower lands of the floodplain, a vast mortality of endemic tree species which did not tolerate river flooding lasting several years, associated with the discharge regulation operated by the hydropower dam (*Balbina*).

Moreover, dams reduce sediment supply causing the rearrangement of the river planform (e.g. reduction of lateral migration (Constantine et al., 2014), channel degradation), inhibiting the rejuvenation process of the riparian vegetation (Camporeale et al., 2013; Vesipa et al., 2017) and promoting vegetation encroachment.

The modification of vegetation species composition, not only jeopardizes several environmental services (de Sousa Lobo et al., 2019), but also may impact the floodplain carbon cycle. In the upper areas of the floodplain, the accumulation

of dead biomass is likely to increase the greenhouse gas emissions of these areas. Root mats and litter matter, no longer recruited by floods and bank erosion, remain and increase the vulnerability of areas to fire during droughts (De Almeida et al., 2016; de Resende et al., 2019; Flores et al., 2017).

Moreover, the encroachment of species from the upland forest and the decay of the poorly flood-tolerant species in topographically depressed regions of the floodplain (de Resende et al., 2019; Schöngart et al., 2021) cause a change in gross primary production (GPP) of such areas. These additional impacts on the global carbon cycle, caused by dams, require further investigations and should be added to the budget of known greenhouse gases emissions produced by anaerobic biomass degradation in reservoirs (Calamita et al., 2021; Deemer et al., 2016; Kemenes et al., 2011; Prairie et al., 2018), in order to better assess the carbon footprint of river regulation in the Neotropics.

Although the threats that the large dams represent for the tropical floodplain forest are well known in the literature (Latrubesse et al., 1957), the long-term consequences and the extent of environmental alteration remain only partially understood (Fearnside, 2016). The poor accessibility of tropical floodplains makes field monitoring and measurement campaigns very expensive, challenging and limited to a few spots. In contrast, to better understand and predict the evolution shift of the ecological regime of floodplain forests, an extensive assessment of vegetation is needed. It is crucial to understand if the whole ecosystem resilience is enough for assuring an adaptation to the hydrological changes (Shilpakar et al., 2021) or whether environmental degradation and catastrophic and irreversible shift of the ecosystems are unavoidable (Shilpakar et al., 2021; Tockner et al., 2010). In particular, as the main vegetation dynamics occur in a narrow area, at the interface between terrestrial and aquatic systems, a high spatial and temporal resolution of the data is needed for their analysis.

Remote sensing offers practical and efficient techniques to estimate biochemical and biophysical parameters and to analyze their evolution over time, even for very remote, wide and poorly accessible areas such as tropical floodplains. Although the vegetation index analysis is widely used in floodplain forest monitoring of temperate regions (Lafage et al., 2014; Nallaperuma and Asaeda, 2020; Sims and Colloff, 2012), it is poorly explored in tropical areas where the extreme cloudiness and presence of aerosols do not allow one to obtain historical series with adequate spatial

and temporal resolution. According to Kobayashi and Dye (2005), the normalized difference vegetation index (NDVI) data from the Advanced Very High–Resolution Radiometer (AVHRR) over the amazonian region show a seasonality mostly caused by variations in atmospheric conditions associated with biomass-burning aerosols and cloudiness. Furthermore, the coarse resolution of NDVI by AVHRR, makes it useless for the analysis of riparian forests. The present study aims to evaluate the impact of dam regulation on floodplain vegetation through a high-resolution satellite-based operative framework. More specifically, we couple temporal evolution analysis of vegetation indices and gross primary production with hydrological transitions data, in order to disentangle the role of river regulation on the floodplain forest alteration. The developed framework was applied to the floodplain of the Uatumã River (Amazonas, Brazil) downstream of the Balbina hydroelectric dam (built in 1987), in order to extensively map the long-term evolution of vegetation in a highly impacted environment due to dam management. Furthermore, the global availability of the adopted datasets makes this analysis potentially applicable to other sites.

Chapter 7

Material and methods

Through a remote sensing analysis of satellite data developed on the free-access cloud computing platform Google Earth Engine (GEE) (Gorelick et al., 2017), we have combined forest changes detection with an analysis of the hydrological transitions and the assessment of the annual GPP, in order to assess the impact of dam alteration on floodplain environment in the last two decades (2001-2019).

7.1 Study area

The developed framework was applied to the floodplain of the Uatumã River (Amazonas, Brazil) downstream of the Balbina hydroelectric dam (built in 1987), in order to extensively map the long-term evolution of vegetation in a highly impacted environment due to dam management. The analysis of vegetation focuses on changes that occurred during the last two decades (2001-2019), while the study of hydrologic alterations involves a period from before the dam has gone into operation until the present (1984-2020).
Uatumã river is a left tributary of the Amazon river (the confluence is approximately 270 km NE to Manaus city) and flows through the state of Amazonas (*Brazil*). The river drains a catchment area of 69,500 km^2 of Precambrian geological formation of the Guiana shield (Melack and Hess, 2010) mostly covered by not inundated forest (*terra firma*) and podzolic white-sand soil. The sediment load is almost absent (Lopes et al., 2019), inducing a river bed stability and slow geomorphic dynamics (Constantine et al., 2014; Junk et al., 2015). The Uatumã is a black-water poorly

nutrient river, but it is very rich in humic material derived from the leaching of various compounds from plant biomass and necromass (Myster, 2018), which confer to the water its acidity (pH 4.05 ± 0.2, Targhetta et al. (2015)) and a typical dark coloring. The soil texture of the floodplain is dominated by silt and clay with sand fraction increasing upward (de Sousa Lobo et al., 2019; Schöngart et al., 2021)).

River discharges and water stages have been highly affected by the Balbina hydro-power dam, wich was built between 1983 and 1987. The formation of a vast reservoir, upstream the dam, induced the rapid decay of almost 3,000 km^2 submerged forest and the formation of more than 3,500 isolated islands (Benchimol and Peres, 2015; Schöngart et al., 2021). Downstream of the dam, the discharge regulation enforced by the hydropower plant management caused alterations in the hydrological cycle, with several consequences on vegetation, that are not completely understood yet (de Resende et al., 2020, 2019; Fearnside, 1989).

An increase in the floodplain tree mortality for certain species was documented as early as the first flow regulation during dam construction (1983-1987), with a peak in the first decade of dam operations (1994-1997) (Schöngart et al., 2021). The study region (~ 3,000 km^2) comprises the Uatumã floodplain downstream of the dam (see Fig.7.1), including the Uatumã Sustainable Development Reserve (USDR), a protected area that aims to preserve nature, while maintaining and improving the lifes of the population (2100 people) through sustainable development projects.

According to the analysis by Assahira et al. (2017), the time series of the unique gauge station that is present downstream of the dam (Cachoeira da Morena, Figure 7.2), shows that the uninomodal flood pulse pattern – very common in the Amazon basin and characteristic of the Uatumã pre-dam regime – almost completely disappeared after the regulation. The post-dam hydrological regime exhibits a reduction of high-water marks up to 95 cm less (Assahira et al., 2017). Conversely, low water regime during post-dam period experienced an increase in water stages compared to the unregulated conditions (Assahira et al., 2017). We also remark that, since the position of the gauge station is on a terrace, near rapids, the results from its data analysis is expected to underestimate the actual hydrological change induced by the dam (de Resende et al., 2019).

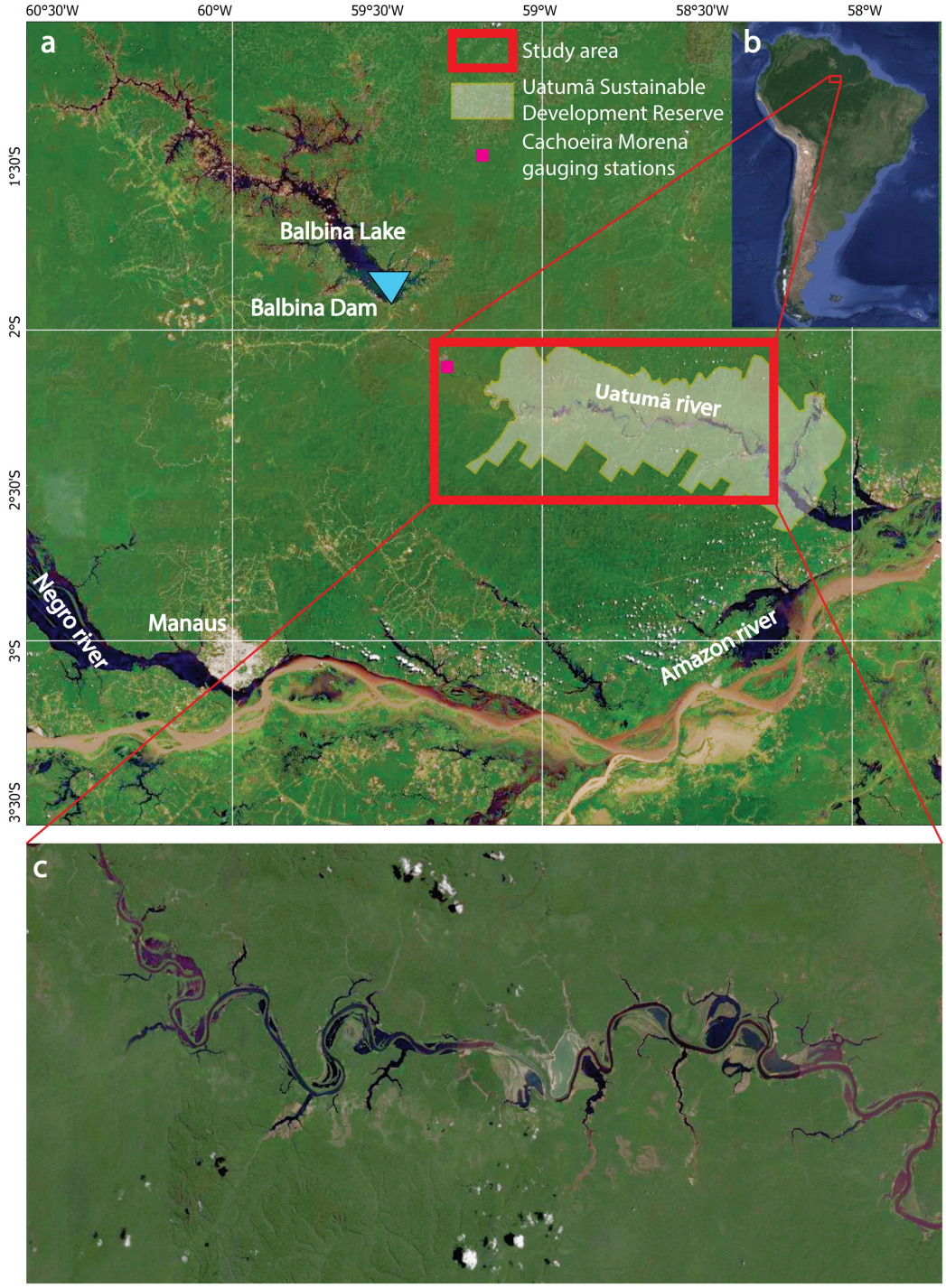

Fig. 7.1 Map of study region. **(a)** Uatumã river from Balbina Lake to confluence with Amazon river. **(b)** South America and study region. **(c)** Study area downstream Balbina dam.

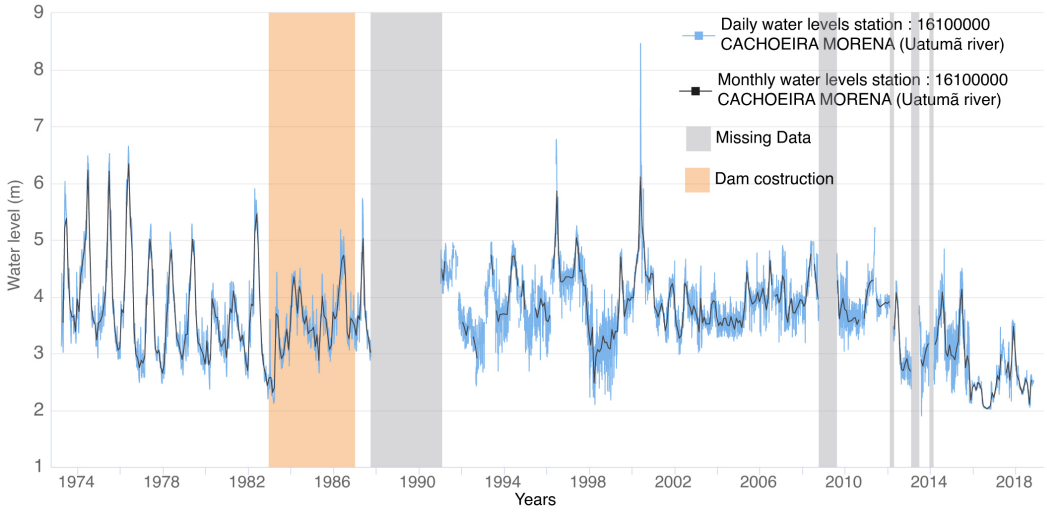

Fig. 7.2 Water levels in gauge station Cachoeira Morena.

7.2 Satellite data

Since the vegetation affected by river dynamics populates a narrow area at the interface between the terrestrial and aquatic system, high spatial resolution data are necessary for mapping and monitoring. Landsat-like optical data at 30 meters spatial resolution are suitable for the detection of specific changes in land cover. Nevertheless, the extreme cloudiness of the Neotropics adversely affects the optical satellite land surface observations.

To obtain gap-filled high spatial resolution reflectance data, Landsat surface reflectance data with a temporal resolution of 16 days and 30 meter spatial resolution, and daily MODIS acquisitions at 500 meters were combined by the HISTARFM algorithm. The algorithm was implemented by Moreno-Martínez et al. (2020) on the GEE cloud computing platform. HISTARFM filters out random noise and reduces the bias of Landsat spectral reflectances based on Bayesian estimations and Kalman filter. The former estimates the Landsat reflectance values for a given time by combining historical Landsat time series and MODIS and Landsat fused values. The latter corrects the bias of the reflectance product by the previous estimation (for further information, see Moreno-Martínez et al. (2020)).

In this way, gap-filled reflectance data (GFHR) at 30 meters spatial resolution was generated from 2001 to 2019 over the whole study area. Then, the high–resolution

products of the normalized difference vegetation index (NDVI), its nonlinear version (kNDVI), and the enhanced vegetation index (EVI), were derived from the GFHR data. The indices NDVI and EVI have been widely and commonly adopted in satellite-based vegetation monitoring. In particular, NDVI has been considered an indicator of photosynthetic activity (Weier and Herring, 2000) whereas the EVI is optimized for high biomass regions and mainly focuses on the canopy structure and is less sensitive to atmospheric alterations (Huete et al., 2002). The kNDVI has been recently proposed as a novel alternative to NDVI that improves the performance with respect to saturation, bias, and complex phenological cycles (Camps-Valls et al., 2021). Formal spectral definitions of the vegetation indices are reported in the next section.

7.3 Water and vegetation indexes

The Normalized Difference Vegetation Index (NDVI) is calculated as the normalized ratio between red (ρ_{red}) and near-infrared (ρ_{NIR}) bands,

$$\text{NDVI} = \frac{\rho_{NIR} - \rho_{red}}{\rho_{NIR} + \rho_{red}}. \tag{7.1}$$

By construction, NDVI varies from -1 to +1. Areas of barren rock, sand, or snow usually show very low NDVI values (for example, 0.1 or less). Shrubs and grasslands crops may result in moderate NDVI values (approximately 0.2 to 0.5). Tropical or temperate forests or in general dense vegetation are characterized High NDVI values (approximately 0.6 to 0.9).

The enhanced vegetation index (EVI) was designed to optimize the vegetation signal with improved sensitivity in high-biomass regions (Huete et al., 2002) and with correction of background soil signals and reduction of atmospheric effects by using blue reflection region:

$$\text{EVI} = G\frac{\rho_{NIR} - \rho_{red}}{L + \rho_{NIR} + C_1\rho_{red} - C_2\rho_{blue}}, \tag{7.2}$$

where ρ_{blue} is the blue band, C1 and C2 are the coefficients of the aerosol resistance term, L is the canopy background adjustment factor and G is the gain factor. Accordingly to the MODIS-EVI algorithm the coefficients can be assumed as: L = 1, C_1 =

6, C_2 = 7.5, and G = 2.5. The range of values for EVI is -1 to 1, with negative value referring to water and cloud and vegetation generally between 0.20 to 0.80.

The kernel NDVI is a non linear generalization of NDVI and reads:

$$\text{kNDVI} = \tanh\left(\frac{\rho_{NIR} - \rho_{red}}{2\sigma}\right)^2, \tag{7.3}$$

where σ is a length-scale parameter, and can be reasonably chosen equal to the average value σ=0.5(NIR + red). This choice leads to a simplified operational index version expressed as kNDVI=tanh (NDVI^2) (Camps-Valls et al., 2021). This index is more resistant to saturation problems than the NDVI and represent a good GPP proxy (Camps-Valls et al., 2021). The kNDVI ranges between 0 and tanh(1)~ 0.76.

The Land Surface Water Index (LSWI) uses the shortwave infrared ρ_{SWIR} and the ρ_{NIR} bands of the electromagnetic spectrum:

$$\text{LSWI} = \frac{\rho_{NIR} - \rho_{SWIR}}{\rho_{NIR} + \rho_{SWIR}}. \tag{7.4}$$

Recent works in evergreen needleleaf forests have shown that LSWI is sensitive to changes in leaf water content over time (Xiao et al., 2004b) and was used in the VPM method by Xiao et al. as a first order approximation to assess the effect of water on plant photosynthesis.

The Modified Normalized Difference Water Index is another water-index and was developed by Han-Qiu, by combining green and SWIR bands:

$$\text{MNDWI} = \frac{\rho_{green-\rho_{SWIR}}}{\rho_{green+\rho_{SWIR}}} \tag{7.5}$$

This index seems to produce an improved performace for detection of water features, because of the high sensitivity due to the use of a shortwave infrared band instead of the near-infrared one in NDWI (Donchyts et al., 2016).

7.4 Vegetation analysis

7.4.1 Data masking

A mask for the water bodies was generated to exclude from the analysis the areas perennially flooded and to avoid misclassification in vegetation changes. The Modified Normalized Difference Water Index (MNDWI) calculated from the GFHR temporal series was used in an unsupervised classification approach, consisting of the Canny edge filter and the Otsu thresholding (Donchyts et al., 2016) in order to obtain the optimum threshold.

Monthly water surface maps between 2001 and 2019 were obtained through the classification of GFHR data. The pixel probability of water presence was obtained for all the pixels of GFHR temporal series. The probability was calculated by dividing the number of water occurrences in the temporal series by the total number of years. Pixels with a water probability value higher than 0.8 (i.e. 80%) were excluded from the vegetation change detection.

7.4.2 Vegetation change detection

The time series of each index was analyzed separately, through a set of segmentation algorithms (LandTrendR, see Kennedy et al. (2018)). The algorithms aim to identify breakpoints in the time series separating periods of durable changes or stability in temporal evolution of the vegetation index. The results of segmentation provide a simplified representation of index history of a pixel as segment lines whose verteces are the breakpoints, identified by year and spectral index value (details are reported in Kennedy et al. (2018) and are recalled in Fig.7.3). Since the algorithms require that the input collection must include only one observation per year, monthly GFHR-based vegetation maps were used to derive the time series of the median annual vegetation index for each pixel. The segmentation process was set up to exclude vegetation changes with a recovery time of one year, which are not consistent with vegetation dynamics and are likely due to noise. Moreover, a maximum number of six segments was imposed to avoid excessive fragmentation of the time series. The possible identified variations were either a loss or a gain of vegetation. These variations were further filtered so that when more than one change of the same type

(loss/gain) was detected in the same pixel only the greatest was reported, indicating the year that changes occurred and its magnitude.

7.4.3 Identification of the regions of interest

Because of the continuous shifts in dry/wet conditions, the correct mapping of vegetation changes can be challenging in some areas. Flush or ephemeral floods induce a decrease in the vegetation index (since reflectance is disturbed by water occurrence), a condition that might be misclassified as a fictitious vegetation loss in the segmentation algorithm. In order to select only changes consistent with actual modifications of vegetation status, and to avoid misclassification due to remaining signal noise, the detected changes in vegetation indices were post-processed. For this purpose only pixels whose change spectral magnitude (e.g.the index difference immediately before and immediately after the change) was greater than 15% of the index range were considered. This threshold was defined after iterative visual inspection and comparison between the map of changes and high-resoluted GEE images. In this way, false-positive detections (low-magnitude disturbances caused by the signal noise) have balanced false-negative detections (missed changes). That allowed the analysis of a wide range of change severity. To this aim, we assumed that the vegetation loss/gain was defined as a reduction/increment of vegetation index exceeding the 15% of the threshold defined above. The vegetation loss/gain considered, comprises plenty of phenomena. In fact, the causes of a vegetation loss can range from temporary deterioration of plants as a result of a very intense and prolonged stress, to the death of the plant itself. Instead, a vegetation gain can be associated with either the germination and growth of a new plant in previously bare soil, the greening of existing plants after the end of stressful conditions, or the invasion of more photosynthetically active plants. One map for each type of change and for each index was produced (in total 6 maps) reporting in each pixel the year y_C in which the change occurred.

These maps were then post-processed through mathematical morphology operations in order to fill the gaps (see *Morphological operation for map refining*). Furthermore, random noise was removed by imposing the condition of 8-neighbor connectivity of pixels having the same y_C. All the clusters whose size was less than 9 pixels were considered noise and discarded from the analysis. Finally, the regions of interest (ROIs) were identified through an image segmentation of each change

map based on y_C. In this way, a ROI has been defined as a group of adjacent pixels with the same y_C. It is noteworthy to point out that not only sudden changes in the indices time series, but also gradual variations, were considered as a change in the vegetation. For the ROIs where a monotonic increase or decrease of vegetation index was detected as a change, the year of the change was conventionally defined as the first year of analysis (2001). The type of vegetation change (loss or gain), and the vegetation index (EVI, NDVI, or kNDVI) adopted to detect that change, was assigned to each ROI.

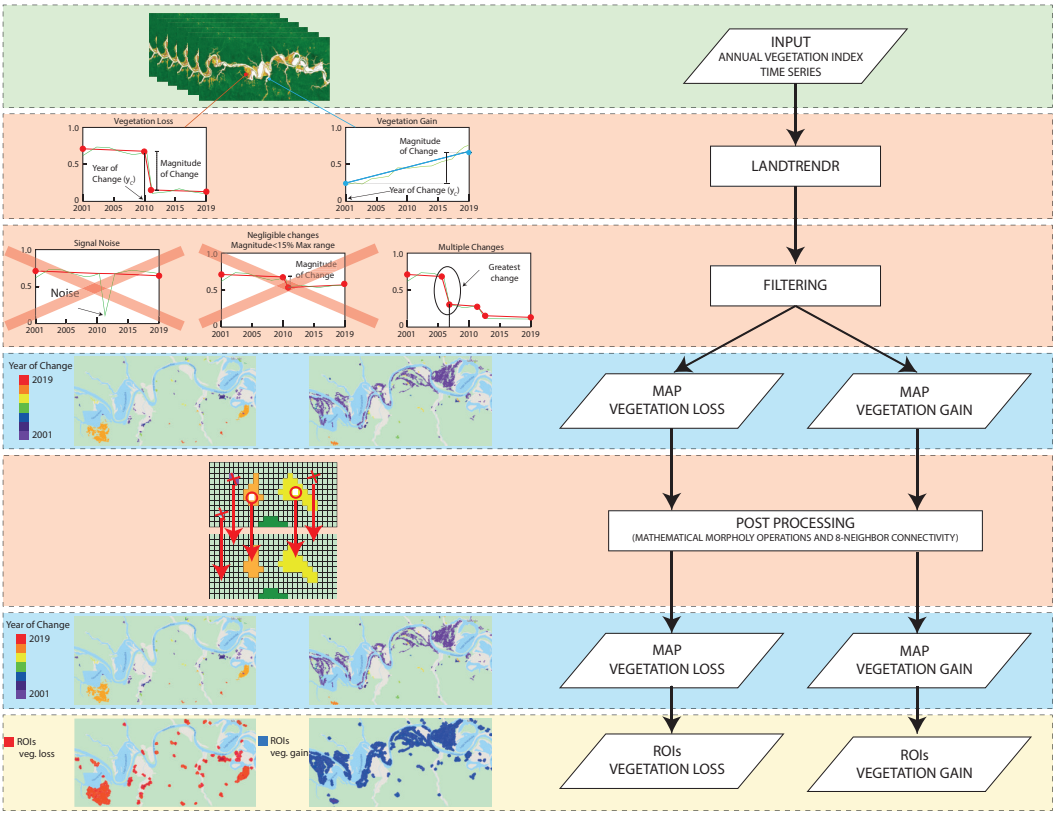

Fig. 7.3 Flow chart of algorithm used to detect vegetation changes and to identify ROIs from annual vegetation index time series. This algorithm was applied to kNDVI, NDVI and EVI

7.4.4 Morphological operation for map refining

Morphological operations are generally composed of dilation and erosion operations applied on binary images (raster cells). In the vegetation changes maps, small holes (up to two-pixel radius) in compact groups of pixel with homogenous y_C could be

due to due to failure in the detection process. In order to fill these failures and to obtain compact areas with the same y_C, the mathematical morphology closure operation (Serra, 1982) was performed on maps. Morphological closing is defined by dilation (A $\oplus$ B) followed by erosion (A $\ominus$ B), where A is the integer-values image of y_C and B is the structuring element (circle kernel with 3 pixels diameter).

7.5 GPP analysis

7.5.1 Assessment of the gross primary production (GPP)

To assess the impact of vegetation alteration on the carbon storage of the fluvial corridor, the inter-annual variability of gross primary production (GPP) was analyzed. The annual GPP was assessed through a Vegetation Photosynthesis Model (VPM) optimized for broad-leaf seasonally moist tropical evergreen forest, proposed by Xiao et al. (2005). The model divides forest canopy into photosynthetically active vegetation and non-photosynthetically active vegetation. GPP is expressed as

$$\mathrm{GPP} = \mathrm{PAR} \times \mathrm{FAPAR} \times \varepsilon_0 \times W_f \times T_f \times P_f, \tag{7.6}$$

where *PAR* is the photosynthetically active radiation [MJ/m^2], FAPAR is the fraction of radiation absorbed by chloroplasts (photosynthetically active part of vegetation), ε_0 is the maximum light use efficiency [kg C/MJ] and W_f, T_f, P_f are downregulating stress factors of water, temperature and phenology for light use efficiency, respectively. Following Xiao et al. (2005) the FAPAR is approximated as

$$\mathrm{FAPAR} = \mathrm{EVI}, \tag{7.7}$$

and the effect of air temperature on the optical energy utilization is

$$T_f = \frac{(T - T_{min})(T - T_{max})}{[(T - T_{min})(T - T_{max})] - (T - T_{opt})^2}, \tag{7.8}$$

where T_{min}, T_{min}, T_{opt} are the minimum, maximum and optimal temperature for photosynthesis, respectively. For tropical conditions they are assumed to be equal to 2°C, 48°C and 28°C (Xiao et al., 2005).

The water stress factor W_f depends on soil moisture and/or vapor pressure deficit, and has been derived through a simple approach using the Land Surface Water Index (LSWI, see Section 7.3 and Xiao et al. (2004a,b, 2005))

$$W_f = \frac{1 + \text{LSWI}}{1 + \text{LSWI}_{max}}, \tag{7.9}$$

with LSWI_{max} being the maximum LSWI during the growing season for each pixel.

The role of phenological stress factor, accounting for the influence of leaf age on photosynthesis at canopy level, can be neglected as a first approximation (i.e., P_f=1), since the canopy of evergreen broadleaf tropical forest is composed of green leaves at various ages (Xiao et al., 2005). GPP was assessed at hourly time step and then cumulated in order to obtain annual values.

7.5.2 Parameter estimation of the VPM model

GPP was assessed at hourly time step and then cumulated in order to obtain annual values. The PAR coefficient was assessed from hourly solar short wave incoming radiation data (Sabater, 2019), assuming that 46% of short wave radiation is available for phothosyntesis (Howell et al., 1983; Papaioannou et al., 1993). Although the GPP was calculated with an hourly frequency, it is reasonable to assume a variation of the FAPAR (EVI) on a monthly scale, as this depends on slow variables such as the structure of the canopy and the optical properties of the plant elements. The coefficient FAPAR was assessed at monthly time step from the EVI time series, according to eq.(2). The EVI index was derived from monthly GFHR data. Considering that the extreme cloudiness and the wet/dry alternation contaminate the reflectance, HISTARFM is able to remove most of the contamination due to clouds and cloud shadows, but it is not able to correct the effect of the water. In order to remove noise in the EVI signal which is unrelated with vegetation temporal evolution such as water contamination, a smoothing procedure (Robinson et al., 2017) was applied. The temperature correction factor was calculated through eq.(3) by using the hourly temperature time series by Sabater (2019). The LSWI product, needed to the assessment of the water restriction factor (eq.(4)), were calculated by using GFHR data.

The maximum light use efficiency ε_0 is a key parameter for the estimation of GPP and it is strongly correlated with the vegetation species. Values of ε_0 was obtained from the the analysis of the net ecosystem exchange (NEE) of CO_2 and the incident PAR measured in a CO_2 eddy-covariance flux tower site, as carried out by Xiao et al. (2005) . Due to the strong correlation with the vegetation species, a land cover classification was performed in order to associate the most suitable value of ε_0 to the different forest types within the study area. Despite the high biodiversity of the Uatumã-Trombetas moist forests ecoregion (Olson et al., 2001), three macro type of vegetation can be identified: i) Land forest having vegetation that is not affected (or only partially affected) by river dynamics (*terra firma*); ii) Flooded forest of igapó type, characterized by vegetation species highly adapted to live under seasonally flooded conditions; iii) Bare soil or herbaceous vegetation.

A random forest was used to classify the land cover based on the aforementioned vegetation macro-types for each year between 2001 and 2019. A set of multi-temporal metrics was used as input for annual land cover mapping. More specifically, the 10-th, 50-th , 90-th percentile and the variance of the vegetation indices NDVI, EVI, kNDVI, the water index LSWI and the Landsat bands B3, B4, B5 and B7 were used. Using high-resolution maps (Google Earth satellite imagery), the carbon density map in 2000 developed by Zarin et al. (2016) and the visible bands of GFHR data in 2000, twenty-two polygons representing homogeneous regions (overall area of 56.5 km^2) were identified and subsequently a sample of 1500 pixels for training and 500 pixels for the validation were randomly extracted. The annual maps of land cover allow one to associate to each pixel an appropriate value of ε_0 according to the type of vegetation. More specifically, for the land forest it was assumed a value of 2.57 gC/MJ, as made by Xiao et al. (2005) for tropical evergreen forests from the time-series data of NEE and incident PAR at the CO2 flux tower sites (Goulden et al., 2004; Malhi et al., 1998). For herbaceous species it was assumed equal to 48% of the one of land forest (i.e., 1.23 gC/MJ), accordingly to Running et al. (2000).

Concerning flooded regions, a proper value of ε_0 is very challenging to obtain, because of the paucity of data for tropical wetland region. Although, some studies estimated the GPP and the correlated parameters in tropical wetlands (Fonseca et al., 2019), they referred to different ecosystems and their results cannot be used for the Uatama igapó. Therefore we assumed the same value of ε_0 adopted for land forest, but corrected in order to account flood effects. It should be remarked that the water restriction factor mentioned above considers just the water deficiency as a limiting

factor, while the negative effects of floods are not taken into account. Although the different species of the igapó forest react in different ways to overcome long flooding periods, because of soil anoxia during flooding, it is a common plant strategy to reduce or completely halt the photosynthetic activity (Schöngart et al., 2002, 2005). For this reason, a dichotomic approach was adopted for the flooded forest: ε_0=0 during flooding, and ε_0 equal to the one of land forest during dry periods. The floods were detected through the monthly water surface maps (see Section 7.4.1).

7.5.3 Algorithm for GPP analysis

The annual time series of GPP_m and GPP_σ in the i-th ROI were divided into a sequence of discrete segments. The segmentation algorithm is based on LANDTRENDR algorithm and allowed the identification of breakpoints separating periods of durable change or stability in time series. To obtain a simplified representation of the time series GPP_m and GPP_σ, the segmentation process was set to identify up to 3 significant segments (4 breakpoints). Hereinafter, we refer to the first and last breakpoints of the simplified series as v_i and v_f, respectively, while the central points as v_{c1} and v_{c2}. A classification algorithm was used to classify the behavior of the simplified time series. The algorithm allowed us to distinguish eight different classes: monotonically increasing (MI) or decreasing (MD), non monotonically increasing or decreasing with a relevant positive or negative spike (nMIS+, nMDS+, nMIS- and nMDS- respectively), and non monotonically increasing (nMI) or decreasing (nMD) without a relevant spikes

Firstly, the algorithm separates monotonic (increasing or decreasing) from non-monotonic time series. To this aim, they were considered as monotonically increasing/decreasing if the breakpoints of time series were sorted in ascending/descending direction, respectively (condition i). If condition i) is false the series was considered non-monotonic and the trend and possible spikes were analysed. It was considered a spike if $v_{c,i} < \min[v_i, v_f]$ or $v_{c,i} > \max[v_i, v_f]$ (condition ii). When a spike was detected and $v_i < v_f$ ($v_i > v_f$) the series was classified as nMIS (nMDS). On the contrary if no spikes was identified but $v_i < v_f$ ($v_i > v_f$) the series was classified as nMI (nMD).

7.6 Region of Interest Analysis

The fundamental unit of this analysis was the Region of Interest (ROI). Every ROI was analyzed in order to investigate the nature of vegetation change, the impact on GPP, and any alterations of the hydrological status. To describe the evolution of a vegetation index within a ROI over the whole considered time period, a series of monthly representative values of the vegetation index was assessed by spatially aggregating the GFHR-based map within the ROI's domain. Two sub-series were divided – from 2001 to the y_C (i.e., the year in which the change occurred) and from y_C to 2019 – in order to analyze the response of the vegetation to the change itself. To detect a trend in the sub-series, a linear regression analysis of the smoothed data (with a 6-months centered moving average) was performed. The average amplitude of oscillations of both sub-series was defined as the mean of the absolute difference between the original signal and its moving average.

Due to the paucity of hydrologic data to perform a statistically robust analysis of the impacts of the dam on the floodplain, we adopted a remote sensing approach. The hydrological alterations that occurred in Uatumã floodplain during the last three decades were assessed through the analysis of the *Global Water Surface* dataset (Pekel et al., 2016). This dataset maps the location and the temporal distribution of surface water from 1984 to 2020, thus allowing to follow water surface behavior from just before the end of the dam construction to the present day. More specifically, each ROI was characterized through the information on *change in seasonality* (i.e. change in intra-annual behavior of water surfaces) between the 1984 and 2020, as provided by the dataset. The dataset, in fact, reports changes between the three classes of not-water, seasonal water, and permanent water and it therefore allows for the identification of a hydrology-induced shift in the flooding regime that occurred in the ROI.

The effects of the vegetation changes on the carbon cycle were evaluated through the analysis of the annual spatial distribution of GPP. In each ROI, the annual time series of the spatial median ($GPP_m(t)$) and the variance ($GPP_\sigma(t)$) was calculated and analyzed (see Section 7.5.3) in order to detect trends in both parameters.

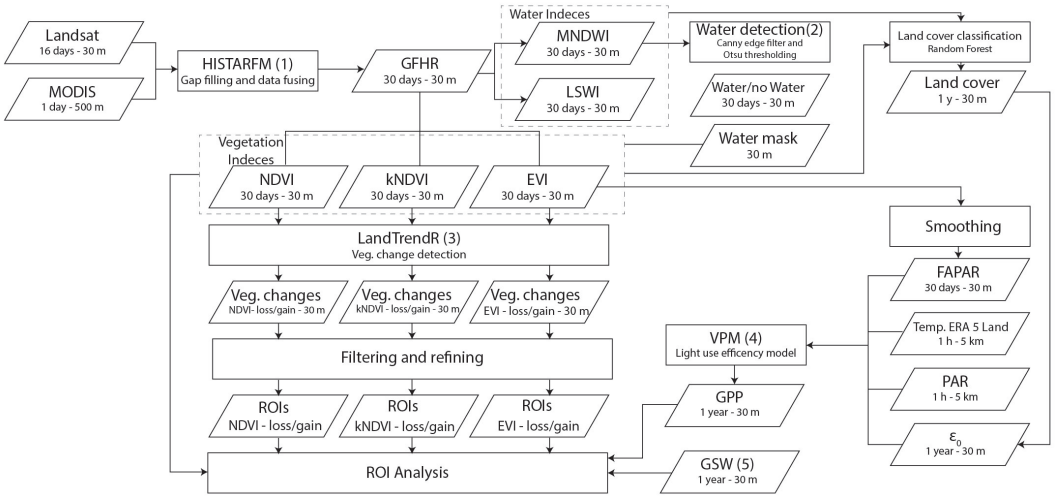

Fig. 7.4 Flowchart of the framework used for the vegetation analysis. (1) Moreno-Martínez et al. (2020), (2) Donchyts et al. (2016) (3) Robinson et al. (2017), (4) Xiao et al. (2005), (5) Pekel et al. (2016)

Chapter 8

Results

In this section the results obtained with each of the three vegetation indices are presented: kNDVI, NDVI and EVI. The results will be shown separately, and hereinafter, they will be reported with a triplet of values, using the same order.

The total area of detected vegetation loss was 53.70 km^2, 27.60 km^2 and 13.23 km^2 (Table 8.1). The kNDVI was the most sensitive index in vegetation loss detection with area and number of ROIs nearly double and quadruple the ones identified by NDVI and EVI (Tab.8.1). The area of vegetation loss common to all the three indices was 11.36 km^2 and represents the 86% of EVI-based detected forest loss.

Table 8.1 Spatial extension of loss and gain with the three indices. The asterisk refers to the percentage of ROIs' total area with a hydrologic change

Vegetation Change type	Vegetation Index	Total Area [km^2]	n ROIs	Mean ROI Area [km^2]	ROIs' total area with an hydrologic change [km^2]
Loss	kNDVI	53.70	696	0.077 ± 0.1423	32.27 (60%*)
Loss	NDVI	27.60	341	0.081 ± 0.1455	17.57 (64%*)
Loss	EVI	13.23	163	0.081 ± 0.1060	6.36 (48%*)
Gain	kNDVI	109.63	715	0.1533 ± 0.4033	88.88 (80%*)
Gain	NDVI	63.72	391	0.1629 ± 0.3633	57.05 (89%*)
Gain	EVI	62.71	442	0.1418 ± 0.3180	52.95 (84%*)

8.1 Vegetation changes

Vegetation loss that occurred during the first decade of the analysis period (2001-2010) accounts for 61%, 69%, and 69% of the totality, with most of this due to a gradual decreasing of the vegetation index (see Fig. 8.1). During the second decade (2011-2019) the loss was concentrated in the year 2015 (Fig. 8.1). This peak coincides with the occurrence of a severe drought induced by ENSO oscillations (2015-2016) that affected especially the higher elevations of the region. Furthermore, the highest lands are rich in the sandy fraction (Schöngart et al., 2021), implying less water retention. The disappearance of the flooding in those zones, a lowering in the rainfall and in water table increase the severity of drought periods (Parolin and Wittmann, 2010). The distribution of (normalized) change in the vegetation index for the ROIs with a loss is bell-shaped, with the mean, median, and mode values very close to each other (see Fig.8.2).

Concerning the ROIs in the floodplain performing a vegetation gain, they involve a surface much larger than the ROIs with a loss. The affected area of vegetation gain amounts to 109.63 km^2, 63.72 km^2, 62.71 km^2, as detected by kNDVI, NDVI or EVI, respectively (Table 8.1). The overall area for vegetation gain commonly detected by all the indices is 41.16 km^2 (amounting to 65% of the area detected by EVI). The vegetation gain is mainly comprised by gradual monotonous increase in the index (72%, 82% and 82% of the overall gain, see Fig.8.1), and this was due to natural tree growth. It was conventionally assumed that all monotonic increases or decreases in the vegetation index occurred in the first year of analysis (y_C = 2001, see Fig.8.1).

The reduction in the oscillation amplitude occurred after the year of change y_C for the majority of the ROIs having a vegetation gain (specifically, 71%, 84%, 91%, see Fig. 8.3d-f). This suggests a change in the phenology and/or a change in species populating the floodplain in favor of a terrestrialization of the forest community. In contrast, loss of vegetation is markedly associated to an increase in the oscillation amplitude (65%, 67%, 77 %, see Fig.8.3a-c).

The linear regression of the vegetation index time series shows a positive trend, after the change, for more than 95 % of ROI with a gain (Fig. 8.4d-f). This indicates that the increase in the index did not stop after the year of the change but is still in progress. On the other hand, for nearly 60 % of areas with a vegetation loss, a

slight recovery followed after the change (Fig. 8.4a-c). Such trends, along with the increase in the oscillation amplitude are probably due to the growth of grassy-like species. Furthermore, for 40% of ROIs with a vegetation loss the index continued to decline after the year of change, thus suggesting a decay towards an unvegetated condition (Fig. 8.4a-c).

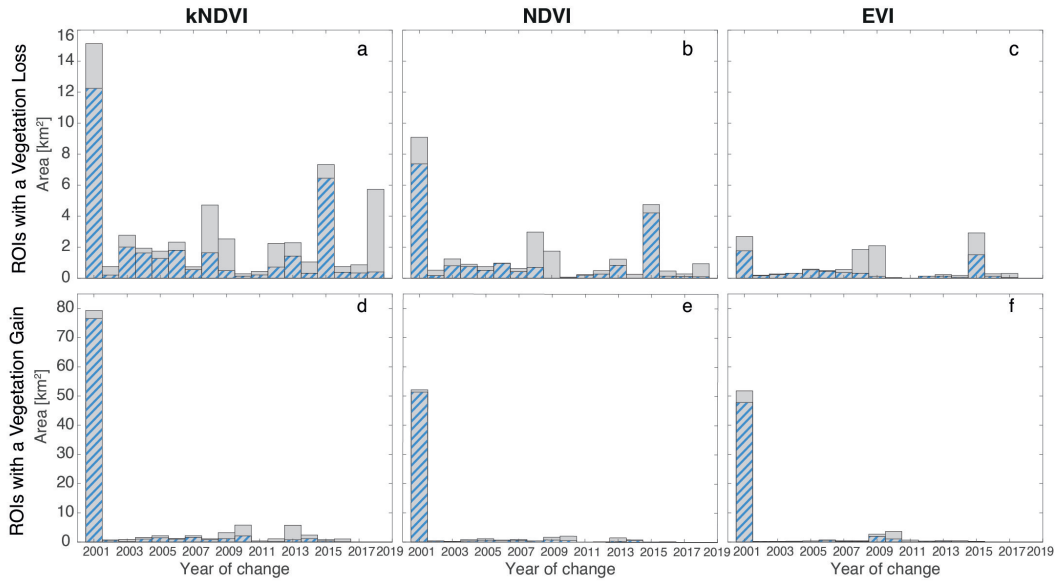

Fig. 8.1 Distribution of the year of change. The blue-dashed portion of the distributions refers to the subset of ROIs wherein an hydrological alteration also occurred. **(a)–(c)** distributions of the year of change for the ROIs with a vegetation loss detected through kNDVI, NDVI and EVI, respectively. **(d)–(f)** distributions of the year change for the ROIs with a vegetation gain detected through kNDVI, NDVI and EVI respectively. It is conventionally assumed that all changes caused by a monotonous increase or decrease in the vegetation index occurred in the first year of the analysis (y_C=2001).

8.2 Hydrological changes

The global map of the water surface developed by Pekel et al. (2016) provides precious information about the spatio-temporal distribution of water surface of the last three decades, with related statistics. Furthermore, Pekel et al. (2016) developed a map capturing the transitions in the hydrological behavior. More specifically, Pekel et al. (2016) identified 8 transition classes of change in seasonality (see definition in the caption of Fig.A.1) between the three classes of not water, seasonal water,

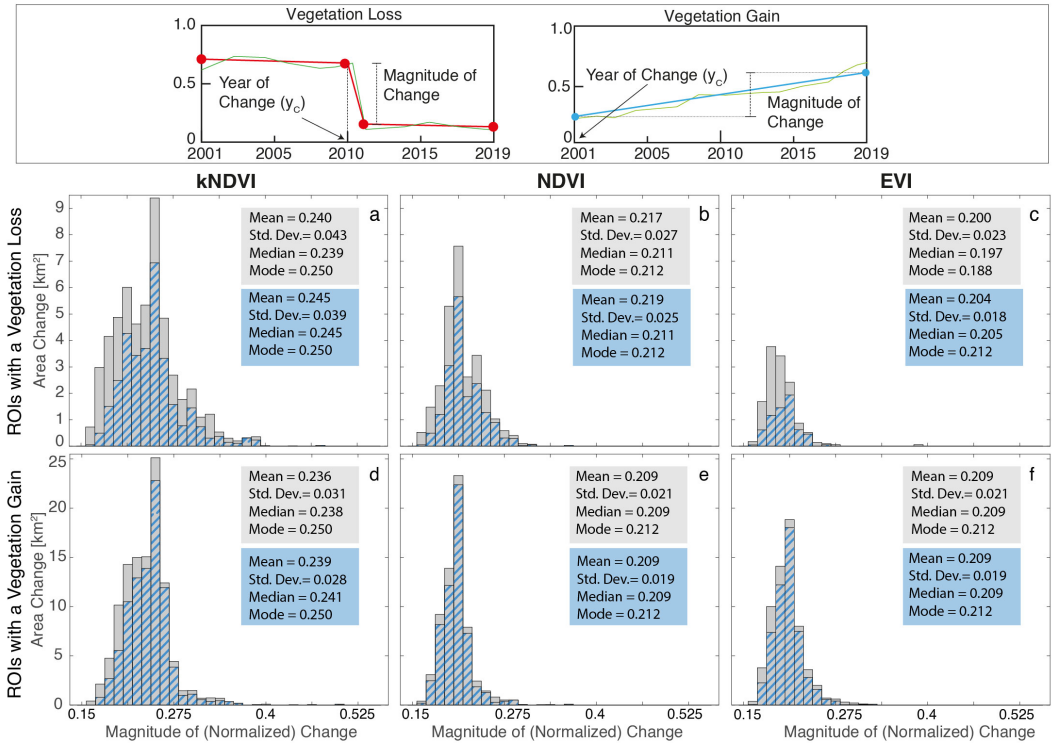

Fig. 8.2 Distribution of the (ROI-averaged) magnitude of (normalized) change. The top panel explains how this quantity has been evaluated for a single pixel. Distributions in **(a)–(f)** refer to spatial mean values of the magnitude within each ROI. The blue-dashed portion of the distributions refers to the subset of ROIs wherein an hydrological alteration also occurred. **(a)–(c)** refer to the ROIs with a loss whereas **(d)–(f)** refer to ROIs with a gain. Features of the distributions are reported in the boxes.

and permanent water (see the original paper for further details about the transition classes). The datasets are annually updated, and the current version (v.1.3) analyzes the global water surface from 1984 to 2020. In the study area of the Uatumã river, about 164 km^2 of permanent water and about 23 km^2 of seasonal water remained so after the dam construction. On the contrary about 29 km^2 of land spots and 5.9 km^2 of permanent water shifted to seasonal waters after the discharge regulation operated by the dam. Finally, a wide area of floodplain was no longer affected by seasonal floods: about 5.4 km^2 shifted to totally terrestrial behaviour, while 33.5 km^2 experienced only a period of seasonal flooding after dam construction and subsequently came back to terrestrial lands.

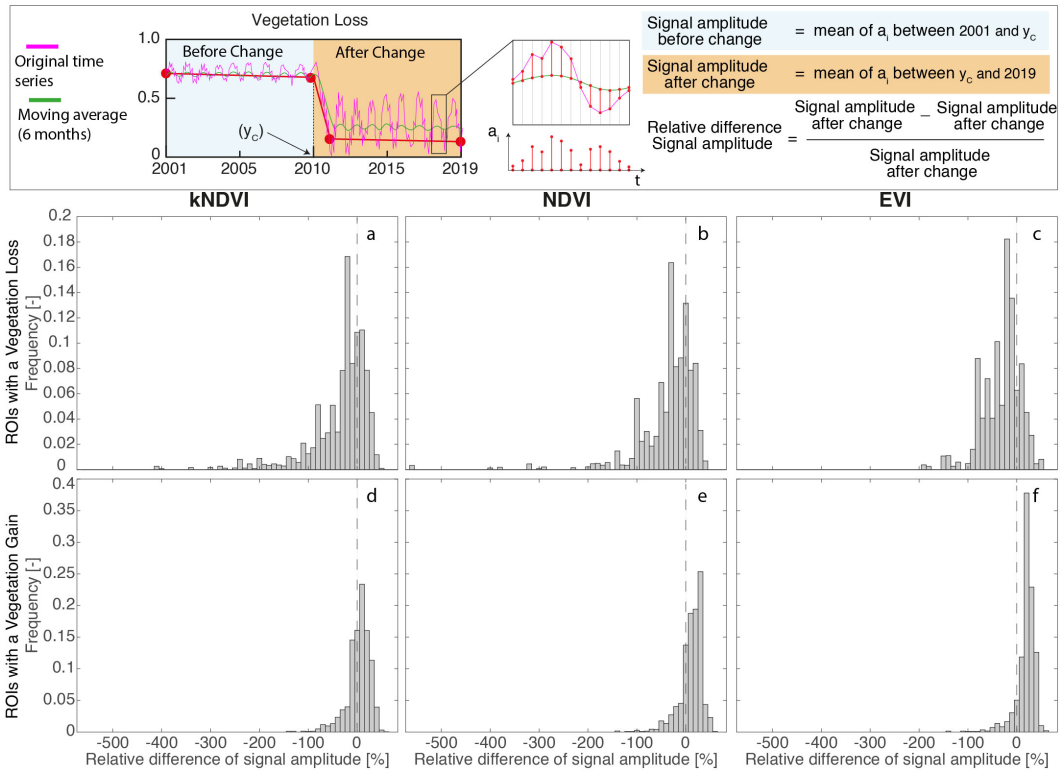

Fig. 8.3 Distribution of the (ROI-averaged) relative difference in the amplitude of intra-annual oscillation of the vegetation index, before and after the change within ROIs. The top panel explains how this quantity has been evaluated for a single pixel. **(a)–(c)** Forest loss **(d)–(f)** Forest gain.

8.3 Hydrological impact on vegetation

By comparison of water transition maps with the above results, we were able to identify the hydrological transitions that occurred within the ROIs after dam construction. The results show that vegetation loss or gain are affected by different kinds of hydrological alterations (see Fig A.8). The 60%, 64%, 48% of loss (Fig.8.2 and Tab.8.1) occurred in areas affected by river dynamics, namely areas flooded quite regularly. More than half of these areas (53.8%, 55.8%, 61.5%) consist of land areas in which a seasonal flooding regime has been established after dam construction (Fig.fig:HydroMap a-c, transition class E). Nearly one-fifth (specifically, 19.8%, 14.5%, 22.9%) of such a *hydrologically-induced vegetation loss* occurred in areas where an ephemeral seasonal regime was established and subsequently disappeared (Fig. A.1 a-c, transition class J). The remaining vegetation loss occurred in areas that

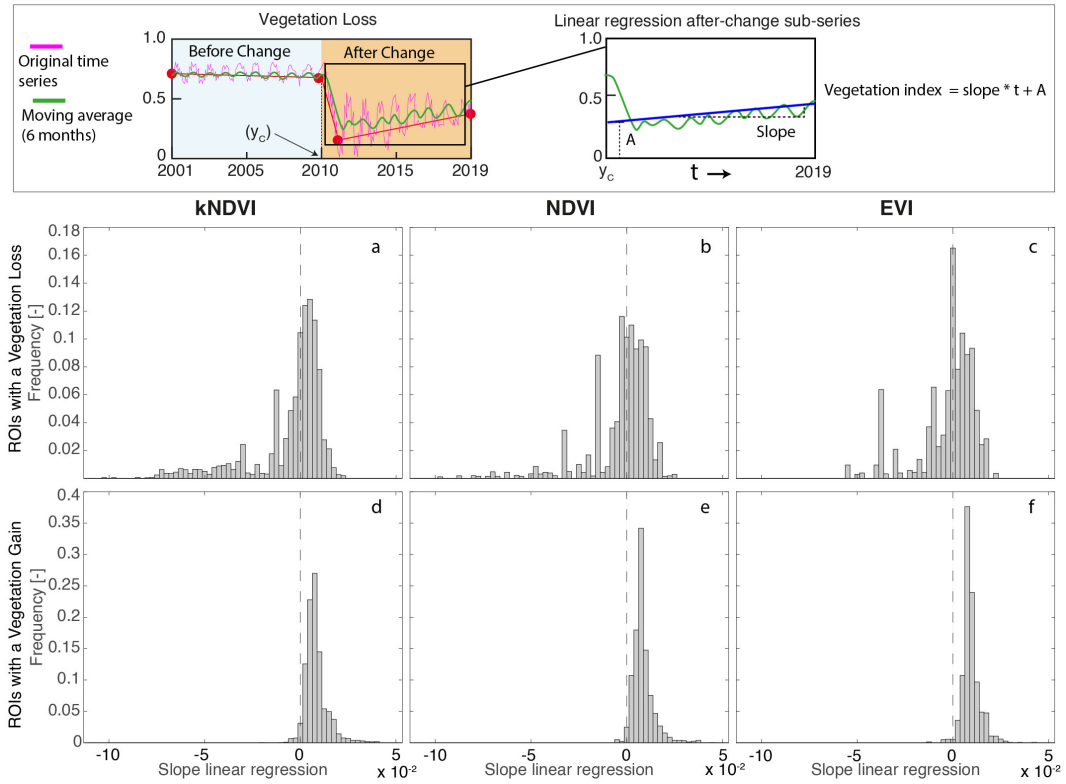

Fig. 8.4 Distribution of the (ROI-averaged) slope of the linear regression of the index time series within ROIs after year of change. The top panel explains how this quantity has been evaluated for a single pixel. **(a)–(c)** Forest loss **(d)–(f)** Forest gain. The vegetation changes are detected through kNDVI ((**a**),(**d**)), NDVI ((**b**),(**e**)) and EVI((**c**),(**f**)).

remained permanently or seasonally inundated despite of dam regulation (Fig. A.1 a-c, transition classes A and D).

As shown in Fig.8.2a-b, the vegetation loss that occurred in areas affected by river dynamics (see blue-dashed bars) represents almost 70% of high-magnitude vegetation changes (i.e., magnitude values higher than the mode). The remaining 30% can be partly due to anthropic use (forest logging, agriculture use, etc.) of the floodplain permitted in the Uatumã Sustainable Development Reserve by the Brazilian authority (Schöngart et al., 2021). On the contrary, the area of forest loss characterized by low-magnitude changes (smaller than the mode) but unrelated to the hydrological regime is respectively 45%, 40% and 67% (Fig.8.2a-b). Since, in this latter case, the ROIs are far from the active channel (see Fig.A.1), and given the low magnitude of the changes, that vegetation alteration may be caused by temporary

vegetation stress not directly related with dam regulation. After comparing the distributions of the magnitude of vegetation gain of all ROIs with the ones affected by river dynamics (Fig. 8.2d-f), it is markedly evident that the forest gain is localized in areas that have undergone an hydrological alteration (regardless of the magnitude of the changes and the index adopted). About 80%, 89% and 84% of the total vegetation gain occurred in fluvially-affected areas (see Table 8.1 and Fig.8.2a-b). In particular, most of them occurred in land spots shifted to seasonal waters after the dam construction and that subsequently came back to terrestrial lands (Fig. A.8 d-f class J).

8.4 Changes in the Gross Primary Production

The forest changes induced by the Balbina dam construction have generated a complex vegetation redistribution of the Uatumã floodplain. Some areas shifted to unvegetated conditions while others underwent a modification in the structure of the plant community. Such a redistribution may alter the capability of the floodplain forest to store carbon, thus affecting the river carbon cycle. For this purpose, high-resolution (30 m-pixel) annual GPP maps were developed through the VPM model (Xiao et al., 2005) (Fig.8.5). In the present study, the impact of river regulation on the forest carbon cycle was assessed through the analysis of the GPP trajectories within each ROI. The annual spatial variance of GPP was used as a proxy of land cover heterogeneity while the temporal changes in the GPP were assessed by monitoring the spatial median of the annual values. Four combinations of changes are therefore possible for both the vegetation loss and gain conditions, depending on the increase/decrease of the spatial variance/median of GPP annual values, respectively (see Fig. 8.6). For example, in 52.7% of ROIs detected by the kNDVI (see Fig. 8.6 a) a vegetation loss is characterized by a decrease in the mean GPP and an increase in the variance. This means that those ROIs, after the change, underwent an increase in the cover heterogeneity (e.g., with a patchy pattern) but a reduced overall gross primary production.

More generally, the results reported in Fig. 8.6 show how the ROIs characterized by a vegetation loss were largely associated to a reduction of GPP in the period 2001-2019 (see Fig.8.6a-c). About a third of these cases are associated with a decrease in the heterogeneity of the land cover within the ROI, which could indicate bare soil

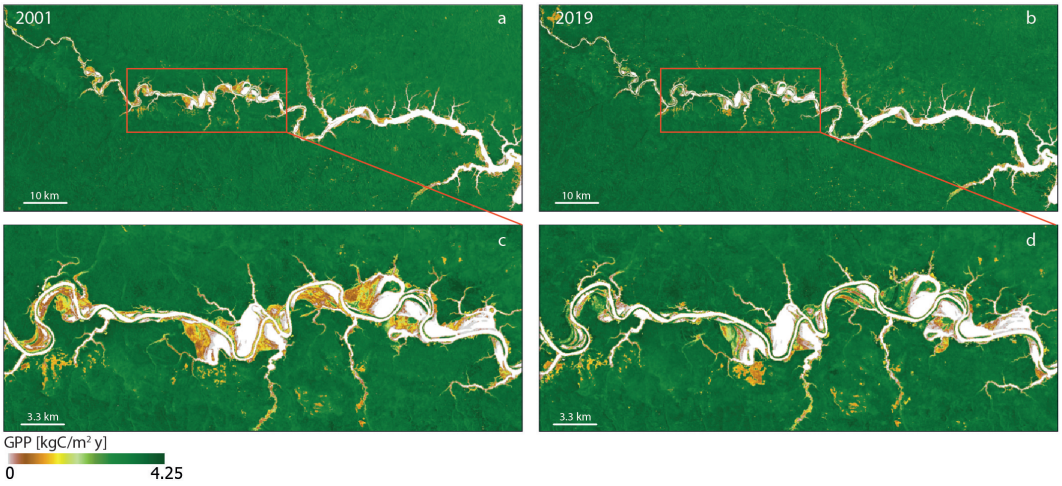

Fig. 8.5 Comparison between annual gross primary production maps (30 m resolution) of Uatumã floodplain forest in 2001 **(a)** and 2019 **(b)**. **(c)** and **(d)** detail of river stretch (red box) affected by greatest changes in GPP in 2001 and 2019 respectively.

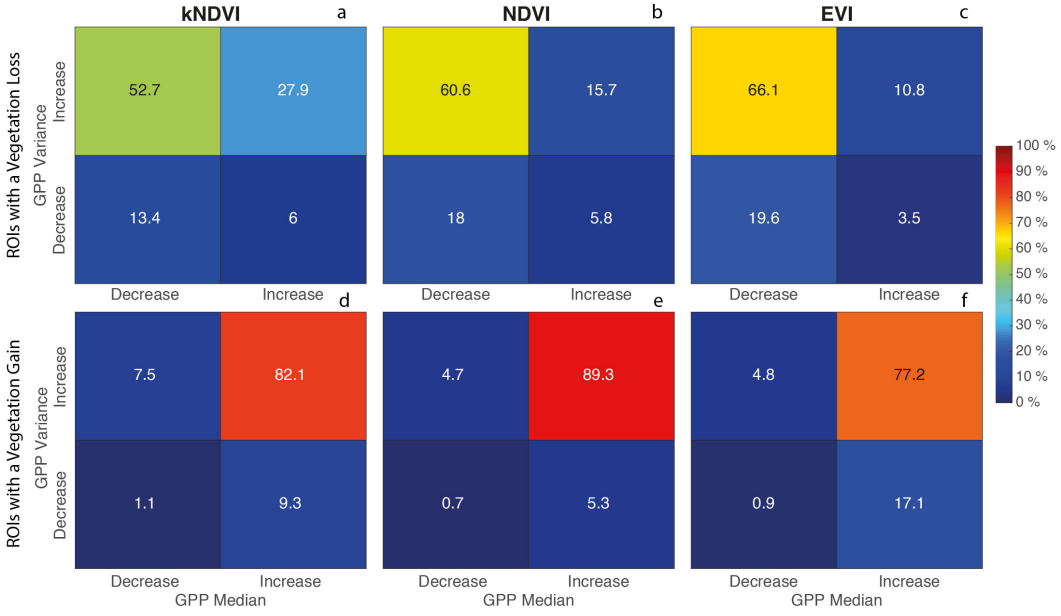

Fig. 8.6 Percentage distribution of combinations of increase/decrease in the GPP spatial median/variance within the ROIs. **(a)**–**(c)** Rois with vegetation loss. **(d)**–**(f)** Rois with vegetation gain.

formation or uniformly distributed vegetated areas with low GPP (e.g. grassland). The remaining two-thirds experienced an increase in land heterogeneity, suggesting a vegetation loss with a leopard-spot pattern. A considerable amount of forest gain

(82%, 89% and 77%) was associated to an increase in both the median value of GPP and land cover heterogeneity (Fig.8.6d-f). According to the field survey made by da Rocha et al. (2019), it is reasonable to suppose that this is due to the encroachment of land forest species in the floodplain forest.

The increase in the heterogeneity suggests a shifting condition, with a patchy distribution, that is far from a stable mature forest. Nevertheless, in at least 17%, 25% and 28% of cases, a first increase followed by a decrease in the variance may suggest that the change is in an advanced state, because a first reorganization of the community structure (increase in heterogeneity) was followed by a homogenization of the patch (Fig.7.3). Although the behavior of GPP spatially-average values within the entire river corridor is similar to that of the adjacent forest, the analysis of the ROIs shows a different story. Some large areas are overcoming an increase in GPP, while others a decrease in primary production. More specifically, the greatest changes are concentrated in a stretch of floodplain about 45 km long, that is 50 km from the dam (see red box Fig.8.5), where the presence of ROIs and hydrological alterations are concentrated.

Chapter 9

Discussion

9.1 The framework

The framework proposed in this study aims to assess the alterations in a tropical floodplain forest induced by river regulation due to damming. The main outcomes of the present approach are the: i) detection and characterization, through a high-resolution analysis, of vegetation changes, in terms of phenology, trajectory of the change, and GPP estimation and the ii) identification of the relation of the changes detected with the local alteration in the hydrologic regime.

The vegetation analysis is based on four pivotal aspects: a) The analysis of the floodplains with a resolution consistent with the scales of the process; b) The adoption of different vegetation indices in order to capture the wider range of vegetation alteration states in a robust way; c) The development of monthly gap-free land observations along the whole study period that allows obtaining information about the vegetation phenology; d) Identification of the sites where vegetation change occurs and their analysis at the site-scale in contrast to floodplain-averaged lumped analysis, as previously made in the literature. The high resolution of reflectance dataset has a crucial role in detecting the changes that affected the narrow aquatic-terrestrial transitional zone. In the considered case, our estimates from the comparison between the maximum extension of flooding and the median width of the river active channel in the last three decades (through *global water surface* dataset) show that river dynamics involve about 600 m of the floodplain width. The effects of dam regulation on vegetation are mostly concentrated in this riparian belt, therefore it deserves to

be scrutinized with adequate resolution. Although monitoring approaches based on moderate spatial resolution data (e.g. MODIS (Zhang et al., 2003)) can compensate the issue of cloud-induced gaps with a high temporal resolution, they provide a too low spatial resolution in the riparian area (1 or 2 pixels per active riparian width). The GFHR data, used herein, instead provides a much higher resolution (about 20 pixels per width of the riparian belt) allowing for precise identification of the areas affected by vegetation changes (see Fig.A.1).

de Resende et al. (2019) developed a high–resolution mapping of dead trees in the Uatumã floodplain through segmentation and a supervised random forest classification of radar data. The use of vegetation indices in our approach provides an additional assessment of forest degradation by analyzing a wider range of states of vegetation stress and progressive deterioration (reduction of photosynthetic activity, decrease of forest greenness, etc.). Moreover, GFHR data allows us to analyze a longer period of time than data from radar missions. In addition, the present framework also identifies vegetation gain. In the present case, this allowed us to quantify the invasion of upland forest vegetation throughout the floodplain, which was indeed observed through field measurements in some plots (da Rocha et al., 2019; de Sousa Lobo et al., 2019).

Many of the current vegetation indices based on high-resolution monitoring systems of Amazonian forest (e.g. PRODES-INPE) are constrained to the availability of reflectance data during the annual free-cloud period (July to September) (Shimabukuro and Ponzoni, 2018). Since the data always refer to the same season of the year (only three or four months of dry period), it is not possible to evaluate changes in intra-annual behavior and therefore in the phenology of forest species. These approaches aimed to detect deforestation (clearings accumulated up to the previous year) focusing on changes between forest and non-forest status, i.e. vegetation that is not characterized by a forest structure (Shimabukuro and Ponzoni, 2018). Therefore they are poorly suited to monitoring changes in plant species or identifying stress conditions in the vegetation.

In our study, the use of HISTARFM fusing algorithm allows the availability of year-round gap-free data and furthermore to analyze vegetation phenology changes. This is very important in interpreting the type of vegetation change that has occurred. Figure 8.3 shows that vegetation loss and gain are widely associated with phenology. In the case of a vegetation loss, an increase in the amplitude of oscillation associated

with a sharp decrease in the average value suggests that, after the change, grassy or shrub species have settled in the ROI. On the other hand, in the case of vegetation gain, a phenology behavior similar to that of the nearby land forest was often found, suggesting an invasion of this type of vegetation in the floodplain area.

The ROI-scale analysis clearly identifies the location where severe forest reshuffling occurred. On the contrary, a spatially averaged lumped analysis along the whole floodplain may not completely identify the actual modification of the forest, since vegetation losses and gains might compensate each other. Although there are many studies concerning the impact of damming that are based on an average-scale analysis of the entire floodplain, those studies usually aim to evaluate the morphological alterations (Nallaperuma and Asaeda, 2020), and cannot assess whether a reorganization of the plant community is taking place in the floodplain. Therefore, those approaches risk underestimating the environmental impact in the area. It is possible to see this effect also by observing what we obtained from the analysis of the GPP trajectories. Although the averaged analysis over the whole floodplain does not show significant GPP changes compared to what has been observed in the nearby forest, a detailed analysis of the individual ROI shows that profound changes are occurring within the floodplains (see Fig.8.5 and Fig. 8.6).

The assessment of the hydrological alterations, based on the Global Water Surface dataset from 1984 to 2020 enabled us to perform a large-scale analysis of the floodplain. The 37 years of data made it possible to go back to pre-dam conditions, and thus investigate the consequences of the dam-induced changes in the hydrologic regime on the evolution of the vegetation during the last 20 years. Since the dataset provides data at a global scale, the analysis of hydrological alteration can also be performed upon others non-instrumented watercourses for which insufficient flow data is available. More specifically, the analysis is well suited to detect the wide variations of the flooded area caused by the alterations of natural flood pulse in the unconfined fluvial systems of the Amazon basin.

9.2 Strength and weaknesses of the procedure

The proposed framework is exportable to other different locations. It is based on the processing of satellite products freely available on GEE (Landsat, MODIS, ERA5-Land, Global water Surface) and does not require special calibration. Moreover, it

is completely implemented on GEE, thus significantly reducing computational cost and storage space.

Although the HISTARFM algorithm showed remarkable efficiency in removing gaps and noise from the signal, the extreme cloud contamination of the Amazonian area cause the presence of residual artifacts. This is due to a non-perfect identification of clouds and their shadows, the paucity of uncontaminated data, and the presence of noise–induced by water (Moreno-Martínez et al., 2020). To reduce the impact of such artifacts on the floodplain analysis, a post-processing filtering operation on vegetation index time series was performed, and all the unrealistic oscillations were removed.

The threshold used for the definition of vegetation loss/gain is the result of an iterative visual inspection and comparison between the map of changes and high-resolution GEE images. Nevertheless, this choice can be further refined through future field validations. The results of the vegetation change detection show differences, depending on the index adopted. The use of three different indices has the purpose of capturing the widest possible range of alterations in the vegetation (photosynthetic activity, structure of the canopy vegetation density of which the indices are proxies). Although, 70% of the areas of change detected with the EVI were also detected by the other two indices, the kNDVI identifies wider additional areas. Further analysis and comparison with field data are needed to define whether this discrepancy is due to the non–linearity of the index (see Section 7.3) and the definition of the threshold value for change detection or its sensitivity to particular types of alterations not found with EVI and NDVI.

Since the framework is fundamentally based on the reflectance data of the HISTARFM algorithm, the time interval analysis is linked to the availability of MODIS data, namely after 2000.

The annual high–resolution GPP maps were developed through a VPM model (Xiao et al., 2005). Although the model was designed for broad-leaf seasonally moist tropical evergreen forest, it was used to assess the GPP also in flooded spots wherein vegetation is subjected to complex interactions with river dynamics. The sedimentary processes involved and the hydrologic regime induce different responses for different species, thus giving rise to an extremely complex scenario. During the dry period, some species of floodplain forest experience an increase in the rate of CO_2 assimilation due to new flushed leaves (more photosynthetically efficient)

and soil aeration (Fonseca et al., 2019; Green et al., 2020; Schöngart et al., 2002). Instead, during long floods, the metabolic activities are reduced to a minimum up to a dormancy status as a survival strategy (Fonseca et al., 2019). However, several studies show that other species (Schöngart et al., 2002) (e.g., evergreen trees in igapó forest) does not completely arrest physiological processes during flooding but they either remain photosynthetically active or flush new leaves and produce flowers and fruits taking energy from carbohydrate reserves through anaerobic metabolism (Schöngart et al., 2002, 2005). Generally speaking, even though different species act in a different way to survive a long period of flood due to the reduction of oxygen in the soil, they reduce or completely stop the GPP. This justifies the choice, as a first approximation, to consider null the GPP in the flooded spots for flood events longer than a month. Nevertheless, the maximum light use efficiency of the flooded forest during the dry period was assumed equal to the one of the land forest. This choice is justified because, the purpose of the work is not to calculate the precise amount of the GPP in each point, but to evaluate its trajectory over time in order to detect the changes. Nevertheless, a future calibration of the model with field data might enhance the GPP accuracy.

9.3 Floodplain alteration

We used Uatumã river as a case study of an altered basin. The construction of the Balbina dam caused a dramatic change in the river hydrological regime. As shown in Fig.7.4, in the period before the discharge regulation (before 1984) the river was characterized by monomodal flood pulse typical of Amazonian basins (Assahira et al., 2017; Junk et al., 1989, 2011). Our results show that the dam has induced perturbation in the seasonal flooding regime with consequences along the whole floodplain. About 33.5 km^2 experienced a seasonal regime only for limited periods and subsequently returned to a terrestrial behavior, 5.4 km^2 of seasonal flooded area was no longer affected by river dynamics, while 5.9 km^2 of permanent water has became seasonal. According to Assahira et al. (2017), the decrease in the maximum water levels (~ 95 cm, according to the hydrometric station of Cachoeira da Morena) and the increase in the minimum water levels (~ 104 cm) caused a massive reduction of area potentially suitable for the growth and survival of typical floodplain forest species. The results show that about 150 km^2 of the floodplain

forest downstream of the dam has undergone vegetation modification over the past two decades. By analyzing changes in vegetation between 2001 and 2019 and also quantifying different forms of vegetation degradation, we found a larger vegetation loss than that one reported by de Resende et al. (2019) for the period 2006-2011. A wide area of highly-degraded vegetation was detected (about 32 km^2, with kNDVI), whose 60% shows evidence of vegetation that is stressed or was partially replaced by grassy species, while about 40% shifted toward unvegetated conditions (Fig.8.4). These changes mainly affected the areas with an alteration of magnitude or flooding frequency.

Despite the high tolerance to flooding, igapó forest species are very sensitive to alterations in the flood pulse. The Balbina dam has modified the monomodal alternation of wet/dry periods which characterized the pre-dam natural conditions, thus inducing an increase in low-water regimes and a reduction in high-water flows (Assahira et al., 2017). The extremely long flooding period and the loss in the terrestrial period that characterized some areas of the lower lands (up to 300 days per year of wet conditions) have induced a selection of a limited number of species able to adapt to this regime (de Resende et al., 2019; Schöngart et al., 2021). Some areas experienced a new flooding condition from 2000 without interruption for more than 8 years, inducing massive mortality of *M. acaciifolium*, one of the most common species in igapó (Assahira et al., 2017; Schöngart et al., 2021). In addition, the peak of forest loss observed in 2005 (Fig 8.1), coincident with a severe drought following a Niño event, highlights how the dam amplifies the effects of natural disturbances.

The consequences of the hydrological changes are not limited to tree mortality induced by the anoxic conditions of long flooded areas (de Resende et al., 2019), but also include the redistribution of plant species (da Rocha et al., 2019). The suppression of high flow conditions reduces the amplitude of oscillation of the water stage, preventing the floods from reaching the highest elevations of the floodplain (Assahira et al., 2017). The lack of a seasonal inundation at the highest elevations prevents the selection of flood-adapted species and allows for the colonization of invasive species from land forests, and therefore the disappearance of the igapó community (Assahira et al., 2017; da Rocha et al., 2019; de Sousa Lobo et al., 2019). Our analysis of vegetation changes and phonological modifications shows that almost 77 km^2 of the floodplain (Fig.8.3d and Table 8.1) have undergone a vegetation gain that can be partly associated to a progressive transition from igapó to upland or secondary forest. Although this ecological transition is accompanied by

an increase in GPP (Fig.8.6), it causes a reduction in biodiversity and a modification in ecosystem functioning (da Rocha et al., 2019; de Sousa Lobo et al., 2019), which is a threat to several environmental services (de Sousa Lobo et al., 2019).

In addition, the disappearance of flooding from the upper floodplain partially or completely inhibits the exchange of organic matter and nutrients between the river and the land and worsens the effect of drought events, making the area vulnerable to wildfire (de Resende et al., 2019).

9.4 Multi-decadal effects of the dam on the forest: a system still far from ecological equilibrium

The Igapó floodplain forest is particularly sensitive to both natural and human-induced changes in hydrology (de Resende et al., 2020). Nevertheless, recent studies using modern radiocarbon techniques have observed that the mortality of some igapó vegetation species in the case of Uatumã mainly occurred after the construction of the dam, while in undisturbed environments it occurred at various times, often associated with La Niña years (de Resende et al., 2019). Our results show that such a vegetation loss downstream of the Balbina dam is still ongoing after 30 years after the construction and does not seem to show a reversal of the trend. Moreover, the floodplain forest is also threatened by species invasion from the land forest.

Damming caused a complex entanglement of terrestrial phase suppression in the lower floodplain region, increasing the alternation between water deficit and anoxic conditions, and the suppression of the aquatic phase in the upper floodplain region. The effects of these disturbances are manifold and still not fully understood. According to Schöngart et al. (2021) the consequences range from the reduction of biodiversity with a loss of ecosystem services, to the increase of greenhouses gasses. Since the high-flow conditions are inhibited, the dead trees remain in the lower part of the floodplain and are exposed to decomposition. The estimates provided by de Resende et al. (2019) predicted that 354 GgC could be potentially emitted from the degradation of dead vegetation downstream of the dam. In addition, a lack of carbon sequestration by vegetation in the remaining unvegetated or highly degraded areas should be considered. Our results show that about 47 km^2 of floodplain experienced a decrease in GPP in the last two decades. Finally, in the upper regions of the

floodplain, emissions from the degradation of root mats and litter, no longer recruited by flooding and levee erosion, and emissions from wildfires represent other sources of greenhouse gases caused by the dam. All these additional emissions worsen the still very high levels of emissions attributed to the dam. The total amount of CH_4 and CO_2 released from the decomposition of vegetation in the upstream reservoirs, from turbines, and from diffuse sources in the water immediately downstream of the dams, is 2.9 MgC-eq per MWh of energy generated, almost ten times that of the coal-fired thermal power plant (Kemenes et al., 2011).

The Uatumã floodplain forest is also threatened by progressive land forest encroachment. Our study shows that an area of approximately 77 km^2 has experienced a progressive increase in the land forest encroachment over the past two decades (Table 8.1 and Fig. 8.1). However, it is unclear whether the hydrological conditions imposed by the dam will lead to a new equilibrium in which the igapó forest will be confined to the boundaries imposed by the dam itself, or whether this ecosystem is doomed to degradation with catastrophic and irreversible shifts of the ecosystem (Bertagni et al., 2018; Tockner et al., 2010). Our analysis of the GPP trajectory shows a widely diffuse increase in land-cover heterogeneity (Fig. 8.6), suggesting that a deep reorganization of the floodplain is in progress. The evidence of ongoing vegetation decline (Table 8.1) seems to indicate that unless some actions are taken to mitigate the dam impact, the ecosystem shift will be unavoidable. The monitoring of the consequences of the dam on vegetation could guide the management policy of the hydropower plant addressing the recovery of this ecosystem, which is populated by a huge variety of vegetation species that reach more than 500 years of life (de Resende et al., 2020; Schöngart et al., 2005).

Our approach is based on the identification and analysis of regions where vegetation changes are concentrated rather than a study of the average behavior of the entire floodplain, allowing very accurate identification of the most degraded or threatened area. The extreme heterogeneity of the forest ecosystems populating the tropical floodplain makes it difficult to generalize what is the response of these ecosystems to alterations in the hydrological regime. At the same time, the increasing number of dams under construction in the Neotropics makes urgent the availability of more accurate procedures for monitoring impacts. Our framework is a practical tool that could be potentially applied to map and monitor floodplain forests, guiding the assessment of the vegetation status and the identification of threatened areas.

Part IV

Chapter 10

General conclusions

This chapter aims to provide a general discussion of results obtained in the Parts II and III, recommendations and final conclusions.

The analysis here presented concerns the interactions between rivers and riparian vegetation and showed the importance of river eco-morphodynamic in the global carbon cycle. Although the role of freshwater in the carbon cycle has been revised in the last decades with increasingly accurate estimates of carbon fluxes, still many mechanisms remain poorly understood or unstudied. As suggested by Hoffmann et al. (2013), floodplains have the potential to be important carbon store at Holocene time scale. Nevertheless, due to the interaction among their compartments, integrated approaches involving ecological, geomorphological and hydraulic knowledge needs to better understand floodplain role in global carbon cycle. Here we presented a process still unexplored, driven by fluvial dynamics that we defined as eco-morphodynamic carbon pumping (eCP): rivers export carbon through the recruitment of riparian forests and promote CO_2 fixation by highly productive new vegetation that repopulates bare bars. The eCP is a complex process result of mutual interactions among water, sediments supply and riparian vegetation that involves fast (vegetation photosynthesis) and slow (carbon stored in woody sediment buried in sedimentary compartments) carbon cycle.

We investigated this mechanism in large natural rivers of the Tropics. Although these account for 9% of the total tropical waterways, it was assessed that they export as many as 12 million tons of carbon each year through eCE. More specifically, the analysis identified 9 rivers (*Big exporters*) that contribute about half of this

carbon export (see Table 5.2). The final fate of the carbon recruited by rivers is still poorly understood. A fraction of this returns to the atmosphere through decomposition and outgassing, but there is a part that is buried and permanently stocked within river corridors as sedimentary organic carbon, or reaches the coastal zones and deep oceans. However, the amount of carbon contained in coarse wood that reaches the ocean has never been assessed on a global scale. This is because, as Evans (2022) suggests, coarse material is not typically sampled by standard POC collection approaches. Although large wood dynamics have been studied in the last decades (Comiti et al., 2016; Ruiz-Villanueva et al., 2016b), but many aspect remain unexplored and tropical region data are quite limited. We argued that the hypothesis of complete degradation of this coarse material into dissolved fractions during transport in the river compartment is incorrect. The LCW can be preserved from rapid decomposition by persisting buried in the sediment compartment for a long time. Therefore riverine sediment represents a reservoir wherein carbon can be stored for millennia before reaching the ocean compartment. We suggest a revision of the estimates of oceanic carbon export by accounting for also contribution of LCW. Indeed, it is reasonable that a consistent fraction of the 8 TgC/yr of eCE herein assessed for the Amazon basin (or 32 TgC/yr, if downscaling is considered) must be added to the current estimate (31 TgC/yr (Schlünz and Schneider, 2000)) of organic carbon flux from the Amazon River to the ocean.

It was also shown how the carbon export phenomenon acts in tandem with an enhanced ability of new vegetation to fix carbon (ENPP). Although ENPP was not directly assessed here for all the rivers analyzed, the carbon export and riparian forest primary production must necessarily equalize when analyzed at sufficiently long time scales. Since it is acknowledged that the total floodplain biomass and forest cover remain roughly constant at the multi-decadal time scale in unaltered or unregulated rivers (Schöngart and Wittmann, 2010), the export of carbon due to river morphodynamic recruitment must be compensated with an NPP of riparian forest dramatically higher than terra-firma mature forest.

In terms of areal efficiency, the eco-morphodynamic Carbon Pump of lowland tropical rivers is a high-performance machine. In the Amazon basin, the carbon exported annually per unit area of river-driven forest loss may be computed as eCE/A_{RDFL}=218-275 MgC/km^2 yr. This value is higher than other widely known fluxes of the carbon cycle, such as POC fluxes from eroded peatlands (< 78 MgC/km^2 yr, (Pawson et al., 2012)), the rate of carbon storage in upland blanket peatland (55

MgC/km^2 yr, (Worrall et al., 2003)) and mass wasting in tropical steep lands (3-39 MgC/km^2 yr, (Ramos Scharrón et al., 2012)). Furthermore, by examining the mineral weathering of silicate soils, we may refer to angiosperm-deciduous systems, which induce an estimated average loss rate of calcium ions of 4 Mg/km^2 yr (Volk, 1989). This corresponds to 2.4 MgC/km^2 yr for the Urey reaction stoichiometry, a value 100 times smaller than the present process. Net oceanic upwelling C-flux per unit area due to thermohaline and Ekman circulations is instead a thousand times smaller (Takahashi, 1989).

In this thesis we present the linkage between eCE and ENPP in a simplified way (see Fig. 3.1). Nevertheless, many other interaction between the two phenomena could exist. The coarse woody material before reach the final destination can be deposited and re-mobilized many times, triggering the formation of "pioneer" vegetated island Gurnell et al. (2005), influencing fluvial morphology (Ruiz-Villanueva et al., 2016b) and biodiveristy of river corridors (Gurnell et al., 2005). This could have effect on the NPP of riparian zone, promoting further carbon fluxes. Further analysis need to define the impact of LCW to enhance NPP.

As mentioned above, the eCP process is deeply related with ecological, morphological and biological dynamics within the floodplain. Although we analyzed the enhanced capability of juvenile riparian vegetation to fix carbon, the influence of river dynamics on the vegetation composition of floodplain forests and related NPP should be deepened. The eCP processes the more carbon the more the river is capable of exporting mature vegetation (high carbon stored but low carbon sequestration capability) and providing new areas that can be colonized by highly productive young vegetation (low carbon stored but high carbon sequestration capability). As described in Section 5.4 for the case of a meandering river, migration rate acts as a filter of riparian communities selecting species that can proliferate within the meandering time scale. Nevertheless, very mobile rivers could perform a rapid rework of floodplain, do not allowing to the elevated region of sediment that has been deposited by the flow to be vegetated. These new areas could remain bare or in poorly vegetated state (with a decrease in eCE and NPP). Similarly to what was observed in Section 5.5 regarding the influence of hydro-periods on carbon signature, extremely dynamic systems could be characterized by lower values of stored carbon. The next steps of our research will include both the adaptation of the methodology developed so far to study eCP in high energy river systems (such as the braided rivers) and the

development of new models capable of coupling river migration with NPP satellite measures of floodplain forests.

Since eCP (eCE+ENPP) is strictly correlated with sediment supply and river migration (see Section 5.3), alterations in lateral erosion, uprooting, and overflow in natural rivers negatively influence this process. Furthermore, increasing development and changes in climate and land use are bringing severe impacts on streams, which are increasingly being regulated thereby altering the natural migration of the river, the flow pattern, and the intermittency of dry and wet periods in floodplains. Since the boom of the damming for hydroelectric production during the last decades (Zarfl et al., 2015), particular attention must be paid to the Amazon basin. This suggests that special policies to preserve the natural regime of *Big Exporters* should be undertaken. The analysis performed on weakly impacted rivers shows that anthropogenic alterations reduce carbon export (eCE_A) by about 40% compared to what is exported by natural rivers. Although further analysis is needed to define how the degree of impact affects eCP, it is justified to assume that in rivers caged between levees and dams the pumping process could be almost negligible. A modern approach to the management of regulated rivers in the Neotropics is crucial to arguing whether hydropower can be still considered a clean source of energy. Present environmental flows (e-flows) assessment in Neotropics requires an upgrade since it is just based on water flow requirements in downstream reaches (Timpe and Kaplan, 2017). Strategic planning urges operational rules able to lessen the overall alteration of hydrological and geomorphological processes, including dynamic flow releases (Niayifar and Perona, 2017), flood pulses, and sediment dynamics when specifying e-flows (Bussettini and Vezza, 2019). Pure hydrology-based methodologies for e-flows assessment (Poff and Zimmerman, 2010) – such as the VMF method (Pastor et al., 2014) – incompletely capture changes in channel morphology, floodplain habitat, and vegetation dynamics due to the sediment-water disequilibrium. The assessment of the river sediment budget can instead tune the flow regime to maintain the desired sediment balance, as well as river structure and functioning. To this aim, it is of paramount importance to implement the recommendations about a combination of water and sediment management (Bussettini and Vezza, 2019; Kondolf et al., 2014; Wohl et al., 2015), integrated with the carbon budgeting at the watersheds scale. Flood releases from dams, as experienced in USA (Jacobson and DL, 2008), India (Thakur et al., 2012) or China (Yang et al., 2010), can be coupled with technical solutions such as bypass off-stream storage, sediment bypass channel or tunnel,

off-channel storage, or sediment sluicing (Lee and Foster, 2013) that can be designed to limit sediment trapping. Moreover, the flood release should mimic the natural flood to preserve the downstream environment.

The carbon density analysis of floodplain forests revealed that the eCP leaves a distinguishable footprint in biomass distributions. Four different signatures due to fluvial bio-morphological activity were identified. A new classification algorithm allowed the analysis of all large tropical rivers and observe that rivers follow a longitudinal signature sequence (NS-MM-PS). Such a sequence corresponds to the stages of the river system from higher land to lower land. These signatures confirm the close link between river morphodynamic processes and vegetation species that distribute themself following specific successional patterns or develop adaptations to survive and proliferate in different environments.

Although these adaptations allow the vegetation species of tropical floodplains to survive intense water stresses, these species are very sensitive to changes in the natural periodicity of the stresses. The presence of ever new hydropower dams has negative effects not only on the carbon pump directly by blocking river dynamics but also indirectly causing the loss of these highly productive floodplain forests unable to tolerate the newly imposed regime of water and sediments. We developed an operative framework based on the assessment of vegetation index changes, hydrological alterations, and the modification of the forest's gross primary production, to assess the wide-ranging impacts and environmental degradation that river regulation has on riparian vegetation. The framework presented in Part III provides a tool that is potentially appliable to map and monitor floodplain forests, helping in the assessment of vegetation status and the identification of threatened areas. The framework was applied to study the influence of the Balbina dam on the Uatamã river, in Brazilian Amazonia. The GFHR data was fundamental to studying the extremely cloudy tropical area of the Amazon basin. The high spatial and temporal resolution analysis of floodplain forest allowed for the detection of modifications of vegetation behavior in terms of both inter- and intra-annual variability, even along the narrow aquatic-terrestrial transitional zone. The analysis of vegetation indices, not only in terms of variation of the annual mean of vegetation index but also about the magnitude of the change and variation in phenology (amplitude of oscillation), guided the detection of vegetation species transitions. Our results suggest a deep reorganization in species populating the floodplain of Uatumã, in favor of a terrestrialization of the forest community. The study of hydrological alterations that affect the region with

vegetation changes disentangled the role of the dam in forest alteration. The forest GPP analysis revealed that vegetation changes along the Uatumã are associated with a dramatic change in the floodplain primary production with possible consequences for the river carbon cycle.

In conclusion, this thesis analyses the effect that a set of specific geomorphic disturbances (ones induced by river dynamics) has on carbon dynamics. This opens the way to extend this concept to other natural processes that cause the remotion of mature vegetation, preserve the carbon contained in that vegetation from rapid re-emission in the atmosphere and force the ecosystem to a juvenile high productive stage. As argued by Swanson et al. (2011), areas where vegetation communities are disturbed frequently by high geomorphic activities, can experience an enhancement of NPP. That is due to the development of early-successional forest ecosystems that populate the area after disturbance and can sequestrate carbon rapidly. In part, this enhancement on NPP can be also due to the time gap between vegetation succession and full recovery of soil microbiological communities, which limits the decomposition of organic matter in the early phase of recovery (Evans, 2022). That phenomena are still poorly understood and further investigations need. Here we highlight that particular attention should be paid also to organic material exported by disturbances. If this organic matter is stored in the sedimentary compartment and cannot return rapidly to the atmosphere can represent a long-term carbon sink. More in general, we suggest that all these natural phenomena of carbon pumping (i.e. coupling of carbon export and storage with enhancement in NPP) should be studied deeply and preserved by anthropical impact. Strategies for the mitigation of climate change effects see as a crucial point the management of anthropical alteration of the global carbon cycle. To reach this goal an accurate compiling of carbon balance and the identification of phenomenon time scale need. The increase in knowledge about processes of natural carbon pumping could provide more effective ways for their preservation. Furthermore, the study of these phenomena could inspire actions that artificially mimic them and help to sequestrate carbon from the atmosphere.

All the analyses developed in this thesis are based on the use of free accessible satellite products and are implemented on GEE to reduce computational time and storage space. This makes the extension of the analysis to other regions or the updating of the data in the coming years easily obtainable.

Appendix A

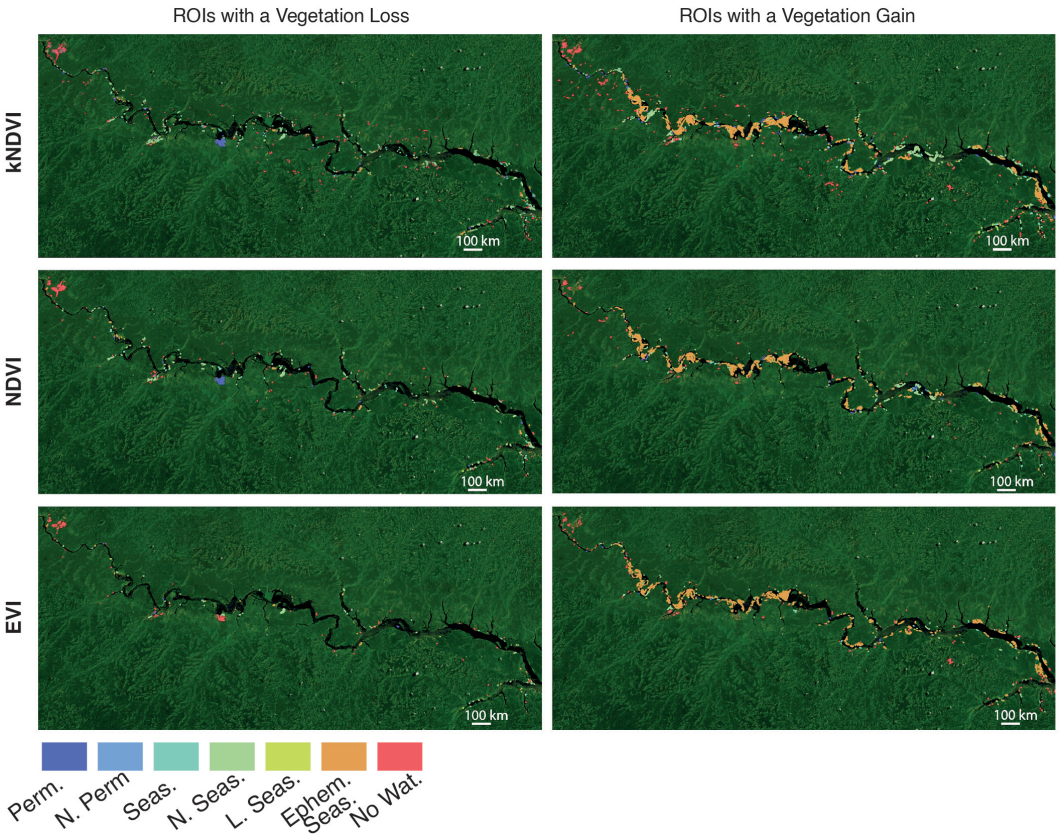

Fig. A.1 Alteration in the hydrological conditions of the ROIs. For graphical reasons only the middle reach of the area of study is reported. The whole region is reported in the Supplementary Material Fig. A.2-A.7

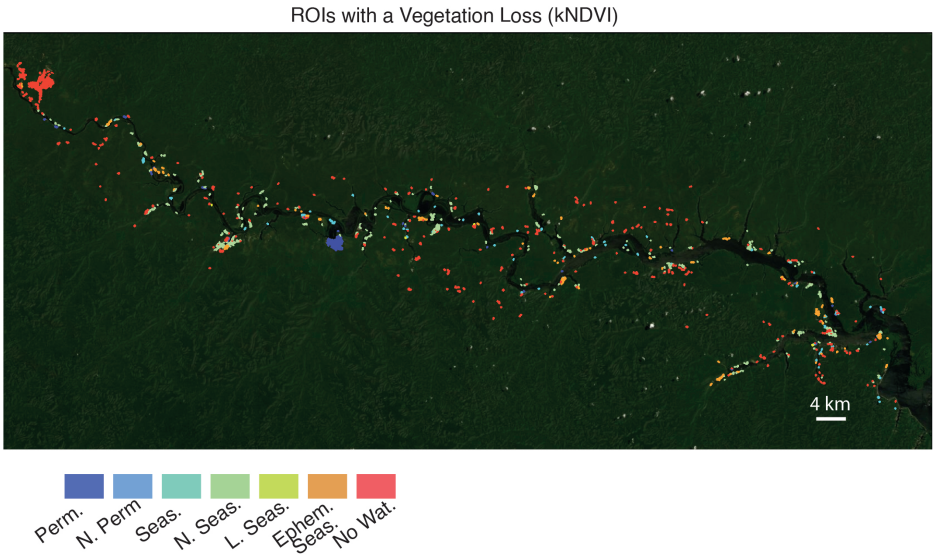

Fig. A.2 Alteration in the hydrological conditions of the ROIs with a vegetation loss (kNDVI).

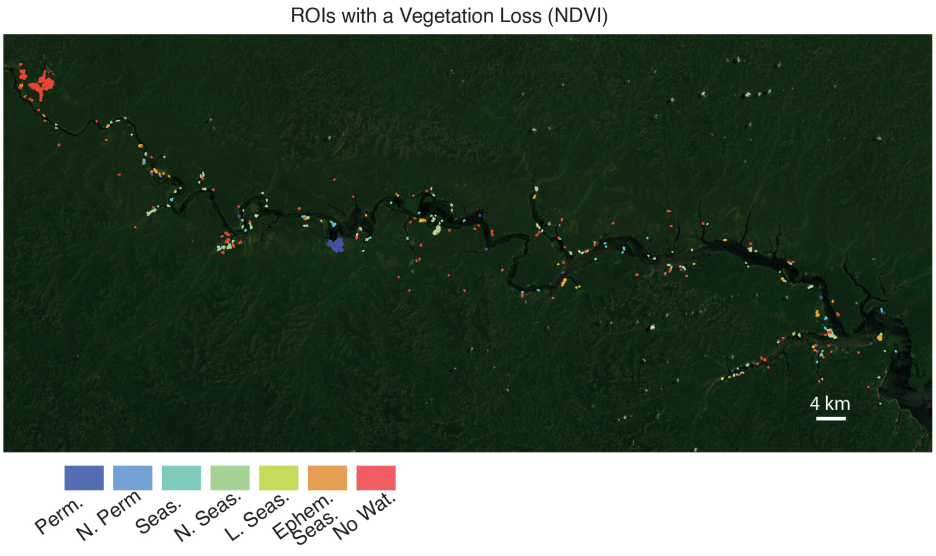

Fig. A.3 Alteration in the hydrological conditions of the ROIs with a vegetation loss (NDVI).

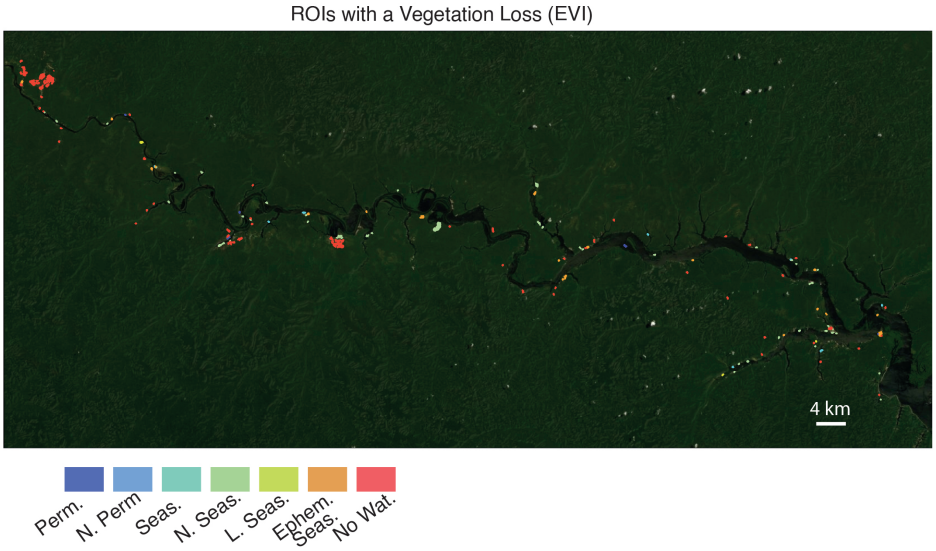

Fig. A.4 Alteration in the hydrological conditions of the ROIs with a vegetation loss (EVI).

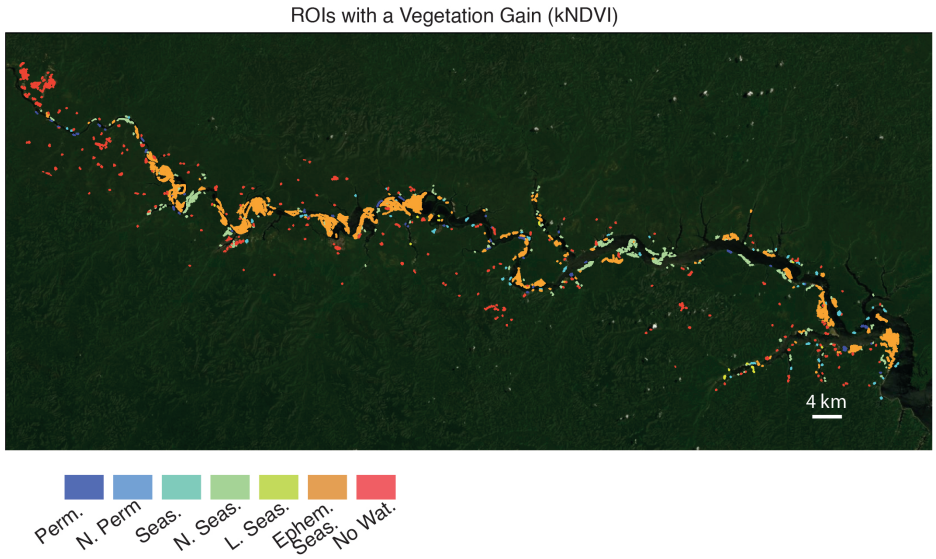

Fig. A.5 Alteration in the hydrological conditions of the ROIs with a vegetation gain (kNDVI).

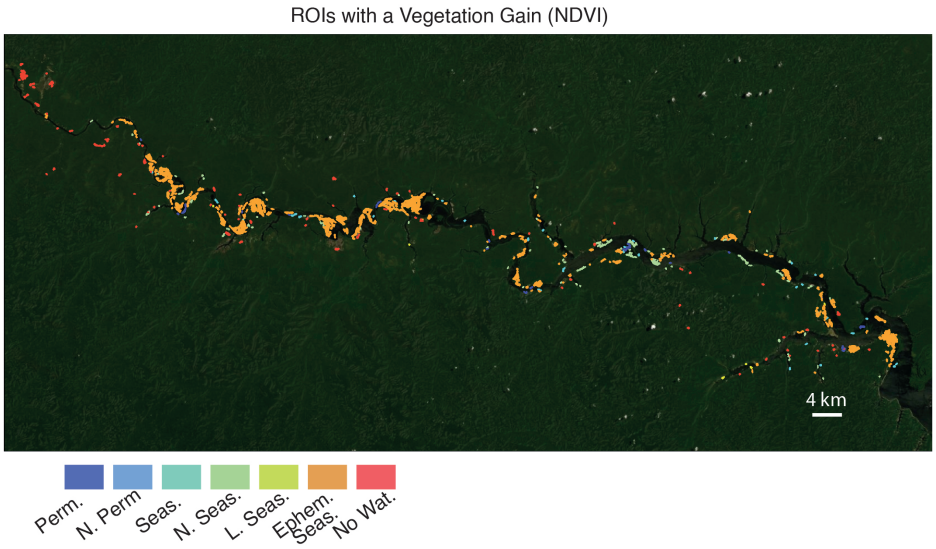

Fig. A.6 Alteration in the hydrological conditions of the ROIs with a vegetation gain (NDVI).

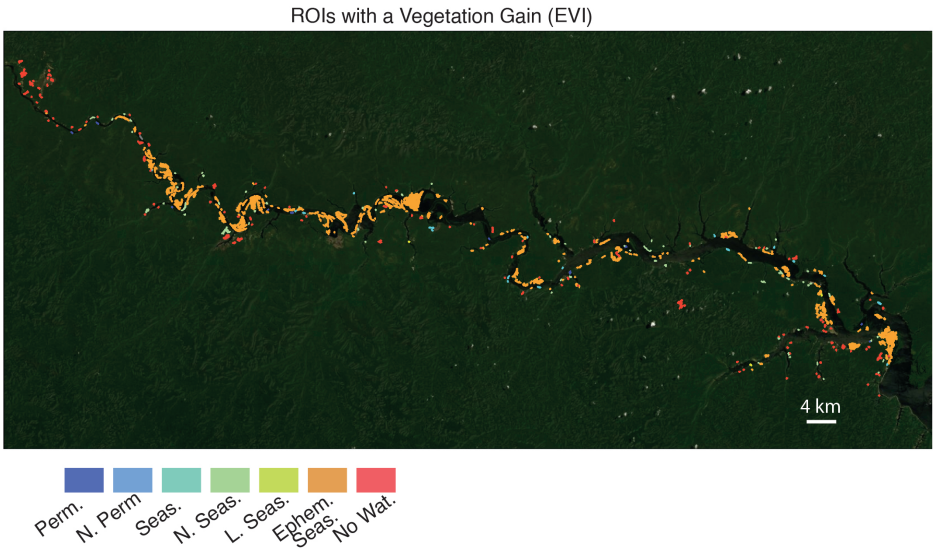

Fig. A.7 Alteration in the hydrological conditions of the ROIs with a vegetation gain (EVI).

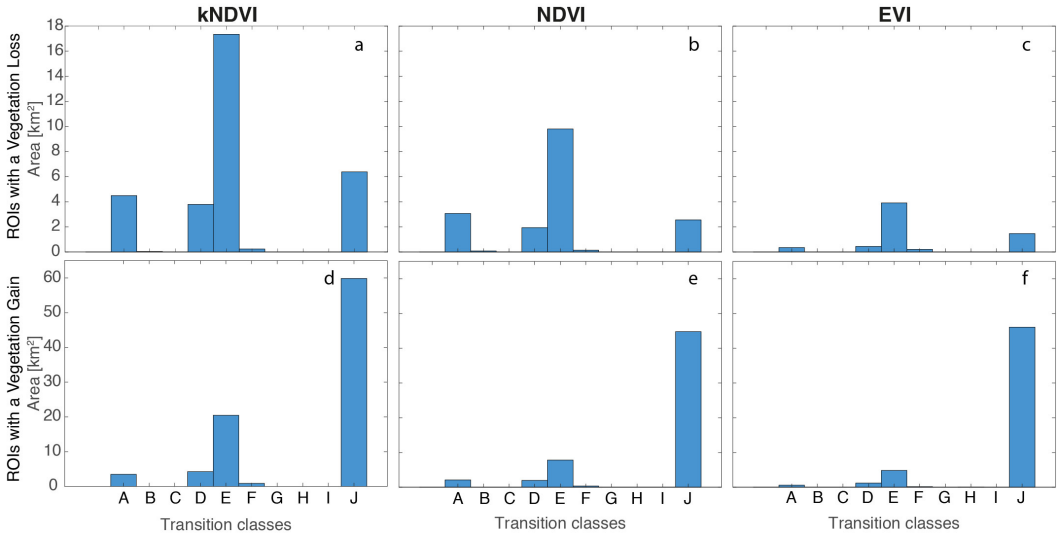

Fig. A.8 Distribution of hydrological transition in ROIs. A: unchanging permanent water surfaces; B: new permanent water surfaces (conversion of land into permanent water); C: lost permanent water surfaces (conversion of permanent water into land); D: unchanging seasonal water surfaces; E: new seasonal water surfaces (conversion of land into seasonal water); F: lost seasonal water surfaces (conversion of a seasonal water into land); G: the conversion of seasonal water into permanent water; H: conversion of permanent water into seasonal water; I: ephemeral permanent water (land replaced by permanent water that subsequently disappears) J: ephemeral seasonal water (land replaced by seasonal water that subsequently disappears). To further details about definition of hydrological transition classes refer to Pekel (2016)

References

Abril, G., Martinez, J.-M., Artigas, L. F., Moreira-Turcq, P., Benedetti, M. F., Vidal, L., Meziane, T., Kim, J.-H., Bernardes, M. C., Savoye, N., et al. (2014). Amazon river carbon dioxide outgassing fuelled by wetlands. *Nature*, 505(7483):395–398.

Agostinho, A. A., Thomaz, S. M., and Gomes, L. C. (2018). Threats for biodiversity in the floodplain of the upper paraná river: effects of hydrological regulation by dams. *Ecohydrol. Hydrobiol.*

Ahmed, J., Constantine, J., and Dunne, T. (2019). The role of sediment supply in the adjustment of channel sinuosity across the Amazon Basin. *Geology*, 47(9):807–810.

Aitkenhead, J. and McDowell, W. H. (2000). Soil c: N ratio as a predictor of annual riverine doc flux at local and global scales. *Global biogeochemical cycles*, 14(1):127–138.

Allen, G. H. and Pavelsky, T. M. (2018). Global extent of rivers and streams. *Science*, 361(6402):585–588.

Almeida, R. M., Shi, Q., Gomes-Selman, J. M., Wu, X., Xue, Y., Angarita, H., Barros, N., Forsberg, B. R., García-Villacorta, R., Hamilton, S. K., et al. (2019). Reducing greenhouse gas emissions of amazon hydropower with strategic dam planning. *Nat. Commun*, 10(1):1–9.

Anderson, L. G. and Amon, R. M. (2015). Dom in the arctic ocean. In *Biogeochemistry of marine dissolved organic matter*, pages 609–633. Elsevier.

Andersson, E., Nilsson, C., and Johansson, M. E. (2000). Effects of river fragmentation on plant dispersal and riparian flora. *Regulated Rivers: Research Management*, 16(1):83–89.

Assahira, C., Piedade, M. T. F., Trumbore, S. E., Wittmann, F., Cintra, B. B. L., Batista, E. S., de Resende, A. F., and Schöngart, J. (2017). Tree mortality of a flood-adapted species in response of hydrographic changes caused by an amazonian river dam. *For. Ecol. Manag.*, 396:113–123.

Aufdenkampe, A. K., Mayorga, E., Raymond, P. A., Melack, J. M., Doney, S. C., Alin, S. R., Aalto, R. E., and Yoo, K. (2011). Riverine coupling of biogeochemical cycles between land, oceans, and atmosphere. *Front. Ecol. Environ.*, 9(1):53–60.

Baccini, A., Goetz, S., Walker, W., Laporte, N., Sun, M., Sulla-Menashe, D., Hackler, J., Beck, P., Dubayah, R., Friedl, M., et al. (2012). Estimated carbon dioxide emissions from tropical deforestation improved by carbon-density maps. *Nat. Clim. Change*, 2(3):182.

Battin, T. J., Kaplan, L. A., Findlay, S., Hopkinson, C. S., Marti, E., Packman, A. I., Newbold, J. D., and Sabater, F. (2008). Biophysical controls on organic carbon fluxes in fluvial networks. *Nat. Geosci.*, 1(2):95–100.

Battin, T. J., Luyssaert, S., Kaplan, L. A., Aufdenkampe, A. K., Richter, A., and Tranvik, L. J. (2009). The boundless carbon cycle. *Nat. Geosci.*, 2(9):598–600.

Beckman, N. and Wohl, E. (2014). Carbon storage in mountainous headwater streams: The role of old-growth forest and logjams. *Water Resour. Res.*, 50.

Benchimol, M. and Peres, C. A. (2015). Edge-mediated compositional and functional decay of tree assemblages in amazonian forest islands after 26 years of isolation. *Journal of Ecology*, 103(2):408–420.

Bertagni, M. B., Perona, P., and Camporeale, C. (2018). Parametric transitions between bare and vegetated states in water-driven patterns. *Proc. Nat. Acad. Sci.*, 115(32):8125–8130.

Bianchi, T. S. (2011). The role of terrestrially derived organic carbon in the coastal ocean: A changing paradigm and the priming effect. *Proceedings of the National Academy of Sciences*, 108(49):19473–19481.

Borges, A. V., Morana, C., Bouillon, S., Servais, P., Descy, J.-P., and Darchambeau, F. (2014). Carbon cycling of lake kivu (east africa): net autotrophy in the epilimnion and emission of co2 to the atmosphere sustained by geogenic inputs. *PloS one*, 9(10):e109500.

Boye, K., Noel, V., Tfaily, M., Bone, S., Williams, K., Bargar, J., and Fendorf, S. (2017). Thermodynamically controlled preservation of organic carbon in floodplains. *Nature Geosci.*, advance online publication.

Bradley, D. N. and Tucker, G. E. (2013). The storage time, age, and erosion hazard of laterally accreted sediment on the floodplain of a simulated meandering river. *J. Geophys. Res. Earth Surf.*, 118(3):1308–1319.

Bussettini, M. and Vezza, P. (2019). Guidance on environmental flows, integrating e-flow science with fluvial geomorphology to maintain ecosystem services. Technical report, World Meteorological Organization – WMO, Commission for Hydrology.

Calamita, E., Siviglia, A., Gettel, G. M., Franca, M. J., Winton, R. S., Teodoru, C. R., Schmid, M., and Wehrli, B. (2021). Unaccounted co2 leaks downstream of a large tropical hydroelectric reservoir. *Proc. Nat. Acad. Sci.*, 118(25).

Camporeale, C., Perona, P., Porporato, A., and Ridolfi, L. (2007). Hierarchy of models for meandering rivers and related morphodynamic processes. *Rev. Geophys.*, 45(RG1001).

Camporeale, C., Perucca, E., Ridolfi, L., and Gurnell, A. (2013). Modeling the interactions between river morphodynamics and riparian vegetation. *Rev. Geophys.*, 51:379–414.

Camporeale, C., Salerno, L., Vezza, P., Perona, P., and Running, S. (2022). *Submitted to Sci. Adv.*

Camps-Valls, G., Campos-Taberner, M., Moreno-Martínez, Á., Walther, S., Duveiller, G., Cescatti, A., Mahecha, M. D., Muñoz-Marí, J., García-Haro, F. J., Guanter, L., et al. (2021). A unified vegetation index for quantifying the terrestrial biosphere. *Science Advances*, 7(9):eabc7447.

Cannell, M. (1984). Woody biomass of forest stands. *Forest Ecol. Manag.*, 8(3-4):299–312.

Castello, L. and Macedo, M. N. (2016). Large-scale degradation of amazonian freshwater ecosystems. *Global change biology*, 22(3):990–1007.

Chambers, J. Q., dos Santos, J., Ribeiro, R. J., and Higuchi, N. (2001). Tree damage, allometric relationships, and above-ground net primary production in central amazon forest. *Forest Ecol. Manag.*, 152(1-3):73–84.

Chave, J., Andalo, C., Brown, S., Cairns, M. A., Chambers, J. Q., Eamus, D., Fölster, H., Fromard, F., Higuchi, N., Kira, T., et al. (2005). Tree allometry and improved estimation of carbon stocks and balance in tropical forests. *Oecologia*, 145(1):87–99.

Ciais, P., Sabine, C., Bala, G., Bopp, L., Brovkin, V., Canadell, J., Chhabra, A., DeFries, R., Galloway, J., Heimann, M., Jones, C., Le Quéré, C., Myneni, R., S., P., and P., T. (2013). Carbon and other biogeochemical cycles. In Stocker, T., Qin, D., Plattner, G.-K., Tignor, M., Allen, S., Boschung, J., Nauels, A., Xia, Y., V., B., and Midgley, P., editors, *Climate Change 2013: The Physical Science Basis. Contribution of Working Group I to the Fifth Assessment Rep. of IPCC*, chapter 6, pages 465–570. CUP, UK and New York, NY, USA.

Cochrane, S. M., Matricardi, E. A., Numata, I., and Lefebvre, P. A. (2017). Landsat-based analysis of mega dam flooding impacts in the amazon compared to associated environmental impact assessments: Upper madeira river example 2006–2015. *Remote Sens. Appl. Soc. Environ.*, 7:1–8.

Cole, J. J., Prairie, Y. T., Caraco, N. F., McDowell, W. H., Tranvik, L. J., Striegl, R. G., Duarte, C. M., Kortelainen, P., Downing, J. A., Middelburg, J. J., and Melack, J. (2007). Plumbing the global carbon cycle: Integrating inland waters into the terrestrial carbon budget. *Ecosystems*, 10(1):171–184.

Comiti, F., Lucía, A., and Rickenmann, D. (2016). Large wood recruitment and transport during large floods: a review. *Geomorphology*, 269:23–39.

Constantine, J. A., Dunne, T., Ahmed, J., Legleiter, C., and Lazarus, E. D. (2014). Sediment supply as a driver of river meandering and floodplain evolution in the amazon basin. *Nat. Geosci.*, 7(12):899.

da Rocha, M., de Assis, R. L., Piedade, M. T. F., Feitosa, Y. O., Householder, J. E., Lobo, G. d. S., Demarchi, L. O., Albuquerque, B. W., Quaresma, A. C., Ramos, J. F., et al. (2019). Thirty years after balbina dam: Diversity and floristic composition of the downstream floodplain forest, central amazon, brazil. *Ecohydrology*, 12(8):e2144.

Dai, M., Yin, Z., Meng, F., Liu, Q., and Cai, W.-J. (2012). Spatial distribution of riverine doc inputs to the ocean: an updated global synthesis. *Current Opinion in Environmental Sustainability*, 4(2):170–178.

Dargie, G. C., Lewis, S. L., Lawson, I. T., Mitchard, E. T., Page, S. E., Bocko, Y. E., and Ifo, S. A. (2017). Age, extent and carbon storage of the central congo basin peatland complex. *Nature*, 542(7639):86.

David, A. (2010). *The global carbon cycle*. Princeton University Press.

Davies, N. S. and Gibling, M. R. (2011). Evolution of fixed-channel alluvial plains in response to Carboniferous vegetation. *Nat. Geosci.*, 4(9):629–633.

De Almeida, D. R. A., Nelson, B. W., Schietti, J., Gorgens, E. B., Resende, A. F., Stark, S. C., and Valbuena, R. (2016). Contrasting fire damage and fire susceptibility between seasonally flooded forest and upland forest in the central amazon using portable profiling lidar. *Remote Sens. Environ.*, 184:153–160.

de Resende, A. F., Piedade, M. T., Feitosa, Y. O., Andrade, V. H. F., Trumbore, S. E., Durgante, F. M., Macedo, M. O., and Schöngart, J. (2020). Flood-pulse disturbances as a threat for long-living amazonian trees. *New Phytol.*, 227(6):1790–1803.

de Resende, A. F., Schöngart, J., Streher, A. S., Ferreira-Ferreira, J., Piedade, M. T. F., and Silva, T. S. F. (2019). Massive tree mortality from flood pulse disturbances in amazonian floodplain forests: The collateral effects of hydropower production. *Sci. Total Environ.*, 659:587–598.

de Sousa Lobo, G., Wittmann, F., and Piedade, M. T. F. (2019). Response of blackwater floodplain (igapó) forests to flood pulse regulation in a dammed amazonian river. *For. Ecol. Manag.*, 434:110–118.

Deemer, B. R., Harrison, J. A., Li, S., Beaulieu, J. J., DelSontro, T., Barros, N., Bezerra-Neto, J. F., Powers, S. M., Dos Santos, M. A., and Vonk, J. A. (2016). Greenhouse gas emissions from reservoir water surfaces: a new global synthesis. *BioScience*, 66(11):949–964.

Dietrich, W. E. and Smith, J. D. (1983). Influence of the point bar on flow through curved channels. *Water Resour. Res.*, 19(5):1173–1192.

Donchyts, G., Schellekens, J., Winsemius, H., Eisemann, E., and Van de Giesen, N. (2016). A 30 m resolution surface water mask including estimation of positional and thematic differences using landsat 8, srtm and openstreetmap: a case study in the murray-darling basin, australia. *Remote Sens.*, 8(5):386.

Downing, J. A., Cole, J. J., Duarte, C., Middelburg, J. J., Melack, J. M., Prairie, Y. T., Kortelainen, P., Striegl, R. G., McDowell, W. H., and Tranvik, L. J. (2012). Global abundance and size distribution of streams and rivers. *Inland waters*, 2(4):229–236.

Drake, T. W., Raymond, P. A., and Spencer, R. G. (2018). Terrestrial carbon inputs to inland waters: A current synthesis of estimates and uncertainty. *Limnol. Oceanogr. Lett.*, 3(3):132–142.

Evans, M. (2022). *Geomorphology and the Carbon Cycle*. John Wiley & Sons.

Fearnside, P. M. (1989). Brazil's balbina dam: Environment versus the legacy of the pharaohs in amazonia. *Environmental management*, 13(4):401–423.

Fearnside, P. M. (2002). Greenhouse gas emissions from a hydroelectric reservoir (brazil's tucuruí dam) and the energy policy implications. *Water, Air, and Soil Pollution*, 133(1):69–96.

Fearnside, P. M. (2014). Impacts of brazil's madeira river dams: Unlearned lessons for hydroelectric development in amazonia. *Environmental Science & Policy*, 38:164–172.

Fearnside, P. M. (2016). Tropical dams: To build or not to build? *Science*, 351(6272):456–457.

Fearnside, P. M. and Pueyo, S. (2012). Greenhouse-gas emissions from tropical dams. *Nat. Clim. Change*, 2(6):382–384.

Ferreira, C. S., Piedade, M. T. F., Wittmann, A. d. O., and Franco, A. C. (2010). Plant reproduction in the central amazonian floodplains: challenges and adaptations. *AoB Plants*, 2010.

Finer, M. and Jenkins, C. (2012). Proliferation of hydroelectric dams in the andean amazon and implications for andes-amazon connectivity. *PloS one*, 7:e35126.

Flores, B. M., Holmgren, M., Xu, C., Van Nes, E. H., Jakovac, C. C., Mesquita, R. C., and Scheffer, M. (2017). Floodplains as an achilles' heel of amazonian forest resilience. *Proceedings of the National Academy of Sciences*, 114(17):4442–4446.

Fonseca, L. D., Dalagnol, R., Malhi, Y., Rifai, S. W., Costa, G. B., Silva, T. S., Da Rocha, H. R., Tavares, I. B., and Borma, L. S. (2019). Phenology and seasonal ecosystem productivity in an amazonian floodplain forest. *Remote Sens.*, 11(13):1530.

Friedl, M. and Sulla-Menashe, D. (2015). Mcd12q1 modis/terra+ aqua land cover type yearly l3 global 500m sin grid v006 [data set]. *NASA EOSDIS Land Processes DAAC*, 10.

Gaughan, A. E., Stevens, F. R., Linard, C., Jia, P., and Tatem, A. J. (2013). High resolution population distribution maps for southeast asia in 2010 and 2015. *PloS one*, 8(2).

Gautier, E., Brunstein, D., Vauchel, P., Roulet, M., Fuertes, O., Guyot, J. L., Darozzes, J., and Bourrel, L. (2007). Temporal relations between meander deformation, water discharge and sediment fluxes in the floodplain of the rio beni (bolivian amazonia). *Earth Surf. Proc. Landf.*, 32(2):230–248.

Giglio, L., Justice, C., Boschetti, L., and Roy, D. (2015). Mcd64a1 modis/terra+aqua burned area monthly l3 global 500m sin grid v006 [data set]. *NASA EOSDIS Land Processes DAAC*.

Goodman, L. (1960). On the exact variance of products. *J. Am. Stat. Assoc.*, 55(292):708–713.

Gorelick, N., Hancher, M., Dixon, M., Ilyushchenko, S., Thau, D., and Moore, R. (2017). Google earth engine: Planetary-scale geospatial analysis for everyone. *Remote Sens. Environ.*

Goulden, M. L., Miller, S. D., Da Rocha, H. R., Menton, M. C., de Freitas, H. C., e Silva Figueira, A. M., and de Sousa, C. A. D. (2004). Diel and seasonal patterns of tropical forest co2 exchange. *Ecol. Appl.*, 14(sp4):42–54.

Green, J., Berry, J., Ciais, P., Zhang, Y., and Gentine, P. (2020). Amazon rainforest photosynthesis increases in response to atmospheric dryness. *Science advances*, 6(47):eabb7232.

Grill, G., Lehner, B., Thieme, M., Geenen, B., Tickner, D., Antonelli, F., Babu, S., Borrelli, P., Cheng, L., Crochetiere, H., et al. (2019). Mapping the world's free-flowing rivers. *Nature*, 569(7755):215–221.

Guo, X., Chen, D., and Parker, G. (2019). Flow directionality of pristine meandering rivers is embedded in the skewing of high-amplitude bends and neck cutoffs. *Proceedings of the National Academy of Sciences*, 116(47):23448–23454.

Gurnell, A., Rinaldi, M., Belletti, B., Bizzi, S., Blamauer, B., Braca, G., Buijse, A. D., Bussettini, M., Camenen, B., Comiti, F., Demarchi, L., garcia de jalon, D., González del Tánago, M., Grabowski, R., Gunn, I., Habersack, H., Hendriks, D., Henshaw, A., Klösch, M., and Ziliani, L. (2016). A multi-scale hierarchical framework for developing understanding of river behaviour to support river management. *Aquat. Sci.*, 78:1–16.

Gurnell, A., Tockner, K., Edwards, P., and Petts, G. (2005). Effects of deposited wood on biocomplexity of river corridors. *Frontiers in Ecology and the Environment*, 3(7):377–382.

Han-Qiu, X. (2005). A study on information extraction of water body with the modified normalized difference water index (mndwi). *J. Remote Sens.*, 5:589–595.

Hansen, M. C., Potapov, P. V., Moore, R., Hancher, M., Turubanova, S., Tyukavina, A., Thau, D., Stehman, S., Goetz, S., Loveland, T. R., et al. (2013). High-resolution global maps of 21st-century forest cover change. *Science*, 342(6160):850–853.

Hartmann, J., Moosdorf, N., Dürr, H., Kempe, S., and Köhler, P. (2009). Global co2-consumption by chemical weathering: What is the contribution of highly active weathering regions? *Glob. Planet. Change*, 99:185–194.

Hedges, J. I., Keil, R. G., and Benner, R. (1997). What happens to terrestrial organic matter in the ocean? *Organic geochemistry*, 27(5-6):195–212.

Hess, L. L., Melack, J. M., Novo, E. M., Barbosa, C. C., and Gastil, M. (2003). Dual-season mapping of wetland inundation and vegetation for the central amazon basin. *Remote Sens. Environ.*, 87(4):404–428.

Hoffmann, T., Mudd, S. M., Van Oost, K., Verstraeten, G., Erkens, G., Lang, A., Middelkoop, H., Boyle, J., Kaplan, J. O., Willenbring, J., et al. (2013). Humans and the missing c-sink: erosion and burial of soil carbon through time. *ESurf*, 1(1):45–52.

Holgerson, M. A. and Raymond, P. A. (2016). Large contribution to inland water co2 and ch4 emissions from very small ponds. *Nature Geoscience*, 9(3):222–226.

Holmes, R. M., Coe, M. T., Fiske, G. J., Gurtovaya, T., McClelland, J. W., Shiklomanov, A. I., Spencer, R. G., Tank, S. E., and Zhulidov, A. V. (2013). Climate change impacts on the hydrology and biogeochemistry of arctic rivers. *Climatic change and global warming of inland waters*, pages 1–26.

Holt, D. and Jones, E. (1983). Bacterial degradation of lignified wood cell walls in anaerobic aquatic habitats. *Appl. Environ. Microbiol.*, 46(3):722–727.

Horgby, Å., Segatto, P. L., Bertuzzo, E., Lauerwald, R., Lehner, B., Ulseth, A. J., Vennemann, T. W., and Battin, T. J. (2019). Unexpected large evasion fluxes of carbon dioxide from turbulent streams draining the world's mountains. *Nature communications*, 10(1):1–9.

Howell, T., Meek, D., and Hatfield, J. (1983). Relationship of photosynthetically active radiation to shortwave radiation in the san joaquin valley. *Agricultural Meteorology*, 28(2):157–175.

Huete, A., Didan, K., Miura, T., Rodriguez, E. P., Gao, X., and Ferreira, L. G. (2002). Overview of the radiometric and biophysical performance of the modis vegetation indices. *Remote Sens. Environ.*, 83(1-2):195–213.

Jacobson, R. and DL, G. (2008). Design of a naturalized flow regime on the lower missouri river. *Ecohydrology*, 1:81–104.

Jones, M. W., Coppola, A. I., Santín, C., Dittmar, T., Jaffé, R., Doerr, S. H., and Quine, T. A. (2020). Fires prime terrestrial organic carbon for riverine export to the global oceans. *Nat. Commun.*, 11(1):1–8.

Junk, W. (1997a). *The Central Amazon Floodplain*. Springer.

Junk, W. J. (1997b). General aspects of floodplain ecology with special reference to amazonian floodplains. In *The Central Amazon Floodplain*, pages 3–20. Springer.

Junk, W. J., Bayley, P. B., Sparks, R. E., et al. (1989). The flood pulse concept in river-floodplain systems. *Can. Fish. Aquat. Sci.*, 106(1):110–127.

Junk, W. J., Piedade, M. T. F., Lourival, R., Wittmann, F., Kandus, P., Lacerda, L. D., Bozelli, R. L., Esteves, F. d. A., Nunes da Cunha, C., Maltchik, L., et al. (2014). Brazilian wetlands: their definition, delineation, and classification for research, sustainable management, and protection. *Aquat. Conserv. Mar. Freshwat. Ecosyst.*, 24(1):5–22.

Junk, W. J., Piedade, M. T. F., Schöngart, J., Cohn-Haft, M., Adeney, J. M., and Wittmann, F. (2011). A classification of major naturally-occurring amazonian lowland wetlands. *Wetlands*, 31(4):623–640.

Junk, W. J., Wittmann, F., Schöngart, J., and Piedade, M. T. (2015). A classification of the major habitats of amazonian black-water river floodplains and a comparison with their white-water counterparts. *Wetl. Ecol.*, 23(4):677–693.

Kahn, J. R., Freitas, C. E., and Petrere, M. (2014). False shades of green: the case of brazilian amazonian hydropower. *Energies*, 7(9):6063–6082.

Kemenes, A., Forsberg, B. R., and Melack, J. M. (2011). Co2 emissions from a tropical hydroelectric reservoir (balbina, brazil). *Journal of Geophysical Research: Biogeosciences*, 116(G3).

Kempe, S. (1979). Carbon in the freshwater cycle. *The global carbon cycle*, 13:317–342.

Kennedy, R. E., Yang, Z., Gorelick, N., Braaten, J., Cavalcante, L., Cohen, W. B., and Healey, S. (2018). Implementation of the landtrendr algorithm on google earth engine. *Remote Sens.*, 10(5):691.

Keogh, K., Martinius, A., and Osland, R. (2007). The development of fluvial stochastic modelling in the norwegian oil industry: A historical review, subsurface implementation and future directions. *Sedimentary Geology*, 202:249–268.

Kobayashi, H. and Dye, D. G. (2005). Atmospheric conditions for monitoring the long-term vegetation dynamics in the amazon using normalized difference vegetation index. *Remote Sens. Environ.*, 97(4):519–525.

Kondolf, G. M., Gao, Y., Annandale, G. W., Morris, G. L., Jiang, E., Zhang, J., Cao, Y., Carling, P., Fu, K., Guo, Q., Hotchkiss, R., Peteuil, C., Sumi, T., Wang, H.-W., Wang, Z., Wei, Z., Wu, B., Wu, C., and Yang, C. T. (2014). Sustainable sediment management in reservoirs and regulated rivers: Experiences from five continents. *Earth's Future*, 2(5):256–280.

Kramer, N. and Wohl, E. (2016). Rules of the road: A qualitative and quantitative synthesis of large wood transport through drainage networks. *Geomorphology*, 279.

Kuriqi, A., Pinheiro, A. N., Sordo-Ward, A., Bejarano, M. D., and Garrote, L. (2021). Ecological impacts of run-of-river hydropower plants—current status and future prospects on the brink of energy transition. *Renewable and Sustainable Energy Reviews*, 142:110833.

Lafage, D., Secondi, J., Georges, A., Bouzillé, J.-B., and Pétillon, J. (2014). Satellite-derived vegetation indices as surrogate of species richness and abundance of ground beetles in temperate floodplains. *Insect Conservation and Diversity*, 7(4):327–333.

Lal, R. (2003). Soil erosion and the global carbon budget. *Environment international*, 29(4):437–450.

Latrubesse, E., Arima, E., Dunne, T., Park, E., Baker, V., d'Horta, F. M., Wight, C., Wittmann, F., Zuanon, J., Baker, P., Ribas, C., Norgaard, R., Filizola, N., Ansar, A., Flyvbjerg, B., and Stevaux, J. (1957). Damming the rivers of the amazon basin. *Nature*, 546:363–369.

Le Quéré, C., Andrew, R., Friedlingstein, P., Sitch, S., Hauck, J., Pongratz, J., Pickers, P., Korsbakken, J. I., Peters, G., Canadell, J., Arneth, A., Arora, V., Barbero, L., Bastos, A., Bopp, L., Chevallier, F., Chini, L., Ciais, P., Doney, S., and Zheng, B. (2018). Global carbon budget 2018 [data paper]. *Earth Syst. Sci. Data*, (10):2141–2194.

Lee, C. and Foster, G. (2013). Assessing the potential of reservoir outflow management to reduce sedimentation using continuous turbidity monitoring and reservoir modeling. *Hydrol. Process.*, (27):1426–1439.

Lees, A. C., Peres, C. A., Fearnside, P. M., Schneider, M., and Zuanon, J. A. (2016). Hydropower and the future of amazonian biodiversity. *Biodiversity and conservation*, 25(3):451–466.

Lehner, B. and Grill, G. (2013). Global river hydrography and network routing: baseline data and new approaches to study the world's large river systems. *Hydrological Processes*, 27(15):2171–2186.

Lewis, W. M., Hamilton, S. K., Lasi, M. A., Rodríguez, M., and Saunders, J. F. (2000). Ecological determinism on the orinoco floodplain: A 15-year study of the orinoco floodplain shows that this productive and biotically diverse ecosystem is functionally less complex than it appears. hydrographic and geomorphic controls

induce a high degree of determinism in biogeochemical and biotic processes. *BioScience*, 50(8):681–692.

Li, M., Peng, C., Wang, M., Xue, W., Zhang, K., Wang, K., Shi, G., and Zhu, Q. (2017). The carbon flux of global rivers: a re-evaluation of amount and spatial patterns. *Ecological Indicators*, 80:40–51.

Lima, A. J. N., Suwa, R., de Mello Ribeiro, G. H. P., Kajimoto, T., dos Santos, J., da Silva, R. P., de Souza, C. A. S., de Barros, P. C., Noguchi, H., Ishizuka, M., et al. (2012). Allometric models for estimating above-and below-ground biomass in amazonian forests at são gabriel da cachoeira in the upper rio negro, brazil. *For. Ecol. Manag.*, 277:163–172.

Linard, C., Gilbert, M., Snow, R. W., Noor, A. M., and Tatem, A. J. (2012). Population distribution, settlement patterns and accessibility across africa in 2010. *PloS one*, 7(2).

Linke, S., Lehner, B., Dallaire, C. O., Ariwi, J., Grill, G., Anand, M., Beames, P., Burchard-Levine, V., Maxwell, S., Moidu, H., et al. (2019). Global hydro-environmental sub-basin and river reach characteristics at high spatial resolution. *Sci. Data*, 6(1):1–15.

Livingstone, D. A. (1963). *Chemical composition of rivers and lakes*, volume 440. US Government printing office.

Lloyd, C. T., Chamberlain, H., Kerr, D., Yetman, G., Pistolesi, L., Stevens, F. R., Gaughan, A. E., Nieves, J. J., Hornby, G., MacManus, K., et al. (2019). Global spatio-temporally harmonised datasets for producing high-resolution gridded population distribution datasets. *Big earth data*, 3(2):108–139.

Lopes, A., Crema, L. C., Demarchi, L. O., Ferreira, A. B., Santiago, I. N., Ríos-Villamizar, E. A., and Piedade, M. T. F. (2019). Herbáceas aquáticas em igapós de água preta dentro e fora de unidades de conservaçao no estado do amazonas. *Biodiversidade Brasileira*, (2):45–62.

Ludwig, W., Probst, J., and Kempe, S. (1996). Predicting the oceanic input of organic carbon by continental erosion. *GLOBAL Biogeochem. Cycles*, 10(1):23–41.

Mackensen, J., Bauhus, J., and Webber, E. (2003). Decomposition rates of coarse woody debris—a review with particular emphasis on australian tree species. *Aust. J. Bot.*, 51(1):27–37.

Malhi, Y., Nobre, A. D., Grace, J., Kruijt, B., Pereira, M. G., Culf, A., and Scott, S. (1998). Carbon dioxide transfer over a central amazonian rain forest. *J. Geophys. Res. Atm.*, 103(D24):31593–31612.

Margono, B., Potapov, P., Turubanova, S., Stolle, F., and Tang, M. (2014). Primary forest cover loss in indonesia over 2000–2012. *Nat. Clim. Change.*, 4(8):730.

Melack, J. M. and Hess, L. L. (2010). Remote sensing of the distribution and extent of wetlands in the amazon basin. In *Amazonian floodplain forests*, pages 43–59. Springer.

Merritt, D. M. and Wohl, E. E. (2006). Plant dispersal along rivers fragmented by dams. *River Research and Applications*, 22(1):1–26.

Meybeck, M. (1982). Carbon, nitrogen, and phosphorus transport by world rivers. *Am. J. Sci*, 282(4):401–450.

Meybeck, M. (1993). Riverine transport of atmospheric carbon: sources, global typology and budget. *Water, Air, and Soil Pollution*, 70(1):443–463.

Morel, A. C., Saatchi, S. S., Malhi, Y., Berry, N. J., Banin, L., Burslem, D., Nilus, R., and Ong, R. C. (2011). Estimating aboveground biomass in forest and oil palm plantation in sabah, malaysian borneo using alos palsar data. *Forest Ecol. Manag.*, 262(9):1786–1798.

Moreno-Martínez, Á., Izquierdo-Verdiguier, E., Maneta, M. P., Camps-Valls, G., Robinson, N., Muñoz-Marí, J., Sedano, F., Clinton, N., and Running, S. W. (2020). Multispectral high resolution sensor fusion for smoothing and gap-filling in the cloud. *Remote Sens. Environ.*, 247:111901.

Muneepeerakul, R., Rinaldo, A., and Rodriguez-Iturbe, I. (2007). Effects of river flow scaling properties on riparian width and vegetation biomass. *Water Resour. Res.*, 43(12).

Myster, R. W. (2018). *Igapó (Black-water flooded forests) of the Amazon Basin*. Springer.

Nallaperuma, B. and Asaeda, T. (2020). The long-term legacy of riparian vegetation in a hydrogeomorphologically remodelled fluvial setting. *River Res. Appl.*, 36(8):1690–1700.

Nebel, G., Dragsted, J., and Vega, A. S. (2001). Litter fall, biomass and net primary production in flood plain forests in the peruvian amazon. *Forest Ecol. Manag.*, 150(1-2):93–102.

Niayifar, A. and Perona, P. (2017). Dynamic water allocation policies improve the global efficiency of storage systems. *Adv. Water Resour.*, 104.

Nilsson, C. and Berggren, K. (2000). Alteration of riparian ecosystems caused by river regulation. *BioScience*, 50:783–792.

Olson, D. M., Dinerstein, E., Wikramanayake, E. D., Burgess, N. D., Powell, G. V., Underwood, E. C., D'amico, J. A., Itoua, I., Strand, H. E., Morrison, J. C., et al. (2001). Terrestrial ecoregions of the world: A new map of life on eartha new global map of terrestrial ecoregions provides an innovative tool for conserving biodiversity. *BioScience*, 51(11):933–938.

Paine, A. D. (1985). Ergodic reasoning in geomorphology: time for a review of the term? *Prog. Phys. Geogr.*, 9(1):1–15.

Papaioannou, G., Papanikolaou, N., and Retalis, D. (1993). Relationships of photosynthetically active radiation and shortwave irradiance. *Theor. Appl. Climatol.*, 48(1):23–27.

Parolin, P. and Wittmann, F. (2010). Tree phenology in amazonian floodplain forests. In *Amazonian floodplain forests*, pages 105–126. Springer.

Pastor, A., Ludwig, F., Biemans, H., Hoff, H., and Kabat, P. (2014). Accounting for environmental flow requirements in global water assessments. *Hydrol. Earth Syst. Sci.*, 18:5041–5059.

Pawson, R., Evans, M., and Allott, T. (2012). Fluvial carbon flux from headwater peatland streams: significance of particulate carbon flux. *Earth Surface Processes and Landforms*, 37(11):1203–1212.

Pekel, J.-F., Cottam, A., Gorelick, N., and Belward, A. S. (2016). High-resolution mapping of global surface water and its long-term changes. *Nature*, 540(7633):418.

Pfister, R., Schwarz, K. A., Janczyk, M., Dale, R., and Freeman, J. (2013). Good things peak in pairs: a note on the bimodality coefficient. *Front. Psychol.*, 4:700.

Poff, N. and Zimmerman, J. (2010). Ecological responses to altered flow regimes: a literature review to inform the science and management of environmental flows. *Fresh. Bio*, 55(1):194–205.

Poff, N. L. and Hart, D. D. (2002). How dams vary and why it matters for the emerging science of dam removal: an ecological classification of dams is needed to characterize how the tremendous variation in the size, operational mode, age, and number of dams in a river basin influences the potential for restoring regulated rivers via dam removal. *BioScience*, 52(8):659–668.

Prairie, Y. T., Alm, J., Beaulieu, J., Barros, N., Battin, T., Cole, J., Del Giorgio, P., DelSontro, T., Guérin, F., Harby, A., et al. (2018). Greenhouse gas emissions from freshwater reservoirs: what does the atmosphere see? *Ecosystems*, 21(5):1058–1071.

Ramos Scharrón, C. E., Castellanos, E. J., and Restrepo, C. (2012). The transfer of modern organic carbon by landslide activity in tropical montane ecosystems. *J. Geophys. Res.*, 117(G3).

Raymond, P. A., Hartmann, J., Lauerwald, R., Sobek, S., McDonald, C., Hoover, M., Butman, D., Striegl, R., Mayorga, E., Humborg, C., Kortelainen, P., Duerr, H., Meybeck, M., Ciais, P., and Guth, P. (2014). Global carbon dioxide emissions from inland waters. *Nature*, 507(7492).

Regnier, P., Friedlingstein, P., Ciais, P., Mackenzie, F. T., Gruber, N., Janssens, I. A., Laruelle, G. G., Lauerwald, R., Luyssaert, S., Andersson, A. J., et al. (2013). Anthropogenic perturbation of the carbon fluxes from land to ocean. *Nature geoscience*, 6(8):597–607.

Robinson, N. P., Allred, B. W., Jones, M. O., Moreno, A., Kimball, J. S., Naugle, D. E., Erickson, T. A., and Richardson, A. D. (2017). A dynamic landsat derived normalized difference vegetation index (ndvi) product for the conterminous united states. *Remote Sens.*, 9(8):863.

Rodriguez-Iturbe, I. and Rinaldo, A. (2001). *Fractal river basins: chance and self-organization*. Cambridge University Press.

Ross, S. (2009). *Probability and statistics for engineers and scientists*. Elsevier, New Delhi.

Ruiz-Villanueva, V., Piégay, H., Gurnell, A. M., Marston, R. A., and Stoffel, M. (2016a). Recent advances quantifying the large wood dynamics in river basins: New methods and remaining challenges. *Rev. Geophys.*, 54(3):611–652.

Ruiz-Villanueva, V., Piégay, H., Gurnell, A. M., Marston, R. A., and Stoffel, M. (2016b). Recent advances quantifying the large wood dynamics in river basins: New methods and remaining challenges. *Reviews of Geophysics*, 54(3):611–652.

Running, S. W., Thornton, P. E., Nemani, R., and Glassy, J. M. (2000). Global terrestrial gross and net primary productivity from the earth observing system. In *Methods Ecol. Evol.*, pages 44–57. Springer.

Saatchi, S., Harris, N., Brown, S., Lefsky, M., Mitchard, E., Salas, W., Zutta, B., Buermann, W., Lewis, S., and Hagen, S. (2011). Benchmark map of forest carbon stocks in tropical regions across three continents. *Proc. Nat. Acad. Sci.*, 108(24):9899–9904.

Sabater, M. (2019). Era5-land hourly data from 1981 to present.

Salerno, L., Moreno-Martínez, Á., Izquierdo-Verdiguier, E., Clinton, N., Siviglia, A., and Camporeale, C. (2022). Satellite analyses unravel the multi-decadal impact of dam management on tropical floodplain vegetation. front. *Environ. Sci*, 10:871530.

Salo, J., Kalliola, R., Häkkinen, I., Mäkinen, Y., Niemelä, P., Puhakka, M., and Coley, P. D. (1986). River dynamics and the diversity of amazon lowland forest. *Nature*, 322(6076):254.

Sawakuchi, H. O., Neu, V., Ward, N. D., Barros, M. d. L. C., Valerio, A. M., Gagne-Maynard, W., Cunha, A. C., Less, D. F., Diniz, J. E., Brito, D. C., et al. (2017). Carbon dioxide emissions along the lower amazon river. *Frontiers in Marine Science*, 4:76.

Schlesinger, W. H. and Melack, J. M. (1981). Transport of organic carbon in the world's rivers. *Tellus*, 33(2):172–187.

Schlünz, B. and Schneider, R. R. (2000). Transport of terrestrial organic carbon to the oceans by rivers: re-estimating flux-and burial rates. *International Journal of Earth Sciences*, 88(4):599–606.

Schöngart, J., Arieira, J., Fortes, C. F., de Arruda, E. C., Da Cunha, C. N., and Arneth, A. (2011). Age-related and stand-wise estimates of carbon stocks and sequestration in the aboveground coarse wood biomass of wetland forests in the northern pantanal, brazil. *Biogeosciences*, 8(11).

Schöngart, J. and Junk, W. J. (2007). Forecasting the flood-pulse in central amazonia by enso-indices. *J. Hydrol.*, 335(1-2):124–132.

Schöngart, J., Piedade, M. T. F., Ludwigshausen, S., Horna, V., and Worbes, M. (2002). Phenology and stem-growth periodicity of tree species in amazonian floodplain forests. *J. Trop. Ecol.*, 18(4):581–597.

Schöngart, J., Piedade, M. T. F., Wittmann, F., Junk, W. J., and Worbes, M. (2005). Wood growth patterns of macrolobium acaciifolium (benth.) benth.(fabaceae) in amazonian black-water and white-water floodplain forests. *Oecologia*, 145(3):454–461.

Schöngart, J. and Wittmann, F. (2010). Biomass and net primary production of central amazonian floodplain forests. In *Amazonian Floodplain Forests*, pages 347–388. Springer.

Schöngart, J., Wittmann, F., Faria de Resende, A., Assahira, C., de Sousa Lobo, G., Rocha Duarte Neves, J., da Rocha, M., Biem Mori, G., Costa Quaresma, A., Oreste Demarchi, L., et al. (2021). The shadow of the balbina dam: A synthesis of over 35 years of downstream impacts on floodplain forests in central amazonia. *Aquat. Conserv.*, 31(5):1117–1135.

Serra, J. P. (1982). *Image analysis and mathematical morphology*. Academic Press, London ; New York.

Shilpakar, R. L., Thoms, M. C., and Reid, M. A. (2021). The resilience of a floodplain vegetation landscape. *Landsc. Ecol.*, 36(1):139–157.

Shimabukuro, Y. E. and Ponzoni, F. J. (2018). *Spectral Mixture for Remote Sensing: Linear Model and Applications*. Springer.

Sims, N. C. and Colloff, M. J. (2012). Remote sensing of vegetation responses to flooding of a semi-arid floodplain: Implications for monitoring ecological effects of environmental flows. *Ecological Indicators*, 18:387–391.

Sorichetta, A., Hornby, G. M., Stevens, F. R., Gaughan, A. E., Linard, C., and Tatem, A. J. (2015). High-resolution gridded population datasets for latin america and the caribbean in 2010, 2015, and 2020. *Sci. data*, 2(1):1–12.

Strahler, A. N. (1957). Quantitative analysis of watershed geomorphology. *Eos, Trans. Am. Geophys. Union*, 38(6):913–920.

Sutfin, N. A., Wohl, E. E., and Dwire, K. A. (2016). Banking carbon: a review of organic carbon storage and physical factors influencing retention in floodplains and riparian ecosystems. *Earth Surf. Proc. Landf.*, 41(1):38–60.

Swanson, M. E., Franklin, J. F., Beschta, R. L., Crisafulli, C. M., DellaSala, D. A., Hutto, R. L., Lindenmayer, D. B., and Swanson, F. J. (2011). The forgotten stage of forest succession: early-successional ecosystems on forest sites. *Frontiers in Ecology and the Environment*, 9(2):117–125.

Syvitski, J. P. M., Vorosmarty, C. J., Kettner, A. J., and P., G. (2005). Impact of humans on the flux of terrestrial sediment to the global coastal ocean. *Science*, 308:376–380.

Takahashi, T. (1989). THE CARBON-DIOXIDE PUZZLE. *Oceanus*, 32(2):22–29.

Targhetta, N., Kesselmeier, J., and Wittmann, F. (2015). Effects of the hydroedaphic gradient on tree species composition and aboveground wood biomass of oligotrophic forest ecosystems in the central amazon basin. *Folia Geobotanica*, 50(3):185–205.

Tealdi, S., Camporeale, C., and Ridolfi, L. (2011). Modeling the impact of river damming on riparian vegetation. *J. Hydrol.*, 396(3):302–312.

Thakur, P., Chalantika, L., and Shiv, P. (2012). River bank erosion hazard study of river ganga, upstream of farakka barrage using remote sensing and gis. *Natural Hazards*, 61:967–987.

Timpe, K. and Kaplan, D. (2017). The changing hydrology of a dammed amazon. *Sci. Adv.*, 3(11):e1700611.

Tockner, K., Pusch, M., Borchardt, D., and Lorang, M. S. (2010). Multiple stressors in coupled river–floodplain ecosystems. *Freshw. Biol.*, 55:135–151.

Torres, J. A. (1994). Wood decomposition of cyrilla racemiflora in a tropical montane forest. *Biotropica*, pages 124–140.

Torres, M., Limaye, A., Ganti, V., Lamb, M., West, A. J., and Fischer, W. (2017). Model predictions of long-lived storage of organic carbon in river deposits. *Earth Surf. Dyn.*, 5:1–40.

Tranvik, L. J., Downing, J. A., Cotner, J. B., Loiselle, S. A., Striegl, R. G., Ballatore, T. J., Dillon, P., Finlay, K., Fortino, K., Knoll, L. B., et al. (2009). Lakes and reservoirs as regulators of carbon cycling and climate. *Limnol. and Oceanogr.*, 54(6part2):2298–2314.

Van Oost, K., Verstraeten, G., Doetterl, S., Notebaert, B., Wiaux, F., Broothaerts, N., and Six, J. (2012). Legacy of human-induced c erosion and burial on soil–atmosphere c exchange. *Proc. Natl. Acad. Sci. USA*, 109(47):19492–19497.

Vannote, R. L., Minshall, G. W., Cummins, K. W., Sedell, J. R., and Cushing, C. E. (1980). The river continuum concept. *Canadian Journal of Fisheries and Aquatic Sciences*, 37(1):130–137.

Venter, O., Sanderson, E. W., Magrach, A., Allan, J. R., Beher, J., Jones, K. R., Possingham, H. P., Laurance, W. F., Wood, P., Fekete, B. M., et al. (2016). Sixteen years of change in the global terrestrial human footprint and implications for biodiversity conservation. *Nat. Commun.*, 7(1):1–11.

Vesipa, R., Camporeale, C., and Ridolfi, L. (2017). Effect of river flow fluctuations on riparian vegetation dynamics: Processes and models. *Adv. Water Resour.*, 110:29–50.

Volk, T. (1989). RISE OF ANGIOSPERMS AS A FACTOR IN LONG-TERM CLIMATIC COOLING. *Geology*, 17(2):107–110.

Ward, J. and Stanford, J. (1995). Ecological connectivity in alluvial river ecosystem and its disruption by flow regulation. *Regul. Riv.-Res. Manag.*, 11(1):105–119.

Weier, J. and Herring, D. (2000). Measuring vegetation (ndvi & evi). *NASA Earth Observatory*, 20.

Wittmann, F., Junk, W. J., and Piedade, M. T. (2004). The várzea forests in amazonia: flooding and the highly dynamic geomorphology interact with natural forest succession. *Forest ecology and Management*, 196(2-3):199–212.

Wittmann, F., Schöngart, J., and Junk, W. J. (2010). Phytogeography, species diversity, community structure and dynamics of central amazonian floodplain forests. In *Amazonian floodplain forests*, pages 61–102. Springer.

Wohl, E. (2016). Bridging the gaps: An overview of wood across time and space in diverse rivers. *Geomorphology*, 279.

Wohl, E., Hall, Jr., R. O., Lininger, K. B., Sutfin, N. A., and Walters, D. M. (2017). Carbon dynamics of river corridors and the effects of human alterations. *Ecol. Mono.*, 87(3):379–409.

Wohl, E., Kramer, N., Ruiz-Villanueva, V., Scott, D., Comiti, F., Gurnell, A., Piégay, H., Lininger, K., Jaeger, K., Walters, D., and Fausch, K. (2019). The natural wood regime in rivers. *BioScience*, 69.

Wohl, E. and Ogden, F. L. (2013). Organic carbon export in the form of wood during an extreme tropical storm, Upper Rio Chagres, Panama. *Earth Surf. Proc. Land.*, 38(12):1407–1416.

Wohl, E., P., B., Jacobson, R., Poff, N., Rathburn, S., Walters, D., and Wilcox, A. (2015). The Natural Sediment Regime in Rivers: Broadening the Foundation for Ecosystem Management. *BioScience*, 65(4):358–371.

Worbes, M. (1997). The forest ecosystem of the floodplains. In *The central Amazon floodplain*, pages 223–265. Springer.

Worrall, F., Reed, M., Warburton, J., and Burt, T. (2003). Carbon budget for a british upland peat catchment. *Sci. of the Total Environ.*, 312(1-3):133–146.

Xiao, X., Hollinger, D., Aber, J., Goltz, M., Davidson, E. A., Zhang, Q., and Moore III, B. (2004a). Satellite-based modeling of gross primary production in an evergreen needleleaf forest. *Remote Sens. Environ.*, 89(4):519–534.

Xiao, X., Zhang, Q., Braswell, B., Urbanski, S., Boles, S., Wofsy, S., Moore III, B., and Ojima, D. (2004b). Modeling gross primary production of temperate deciduous broadleaf forest using satellite images and climate data. *Remote Sens. Environ.*, 91(2):256–270.

Xiao, X., Zhang, Q., Saleska, S., Hutyra, L., De Camargo, P., Wofsy, S., Frolking, S., Boles, S., Keller, M., and Moore III, B. (2005). Satellite-based modeling of gross primary production in a seasonally moist tropical evergreen forest. *Remote Sens. Environ.*, 94(1):105–122.

Yang, S., Milliman, J., Li, P., and Xu, K. (2010). 50,000 dams later: Erosion of the yangtze river and its delta. *Glob. Planet. Change*, 75.

Zarfl, C., Lumsdon, A., Berlekamp, J., Tydecks, L., and Tockner, C. (2015). A global boom in hydropower dam construction. *Aquat. Sci.*, 77:161–170.

Zarin, D. J., Harris, N. L., Baccini, A., Aksenov, D., Hansen, M. C., Azevedo-Ramos, C., Azevedo, T., Margono, B. A., Alencar, A. C., Gabris, C., et al. (2016). Can carbon emissions from tropical deforestation drop by 50% in 5 years? *Glob. Change Biol.*, 22(4):1336–1347.

Zhang, X., Friedl, M. A., Schaaf, C. B., Strahler, A. H., Hodges, J. C., Gao, F., Reed, B. C., and Huete, A. (2003). Monitoring vegetation phenology using modis. *Remote Sens. Environ.*, 84(3):471–475.